

2011

Development of Imaging Paradigms for Drug Distribution and Fate in the Eye

Corey Albert Smith

Follow this and additional works at: <https://ir.lib.uwo.ca/digitizedtheses>

Recommended Citation

Smith, Corey Albert, "Development of Imaging Paradigms for Drug Distribution and Fate in the Eye" (2011). *Digitized Theses*. 3342.
<https://ir.lib.uwo.ca/digitizedtheses/3342>

This Thesis is brought to you for free and open access by the Digitized Special Collections at Scholarship@Western. It has been accepted for inclusion in Digitized Theses by an authorized administrator of Scholarship@Western. For more information, please contact wlsadmin@uwo.ca.

Development of Imaging Paradigms for Drug Distribution and Fate in the Eye

(Spine title: Imaging Paradigms for Drug Distribution and Fate in the Eye)

(Thesis format: Integrated Article)

by

Corey A. Smith

Graduate Program in Biomedical Engineering

2

A thesis submitted in partial fulfillment
of the requirements for the degree of
Master of Engineering Science

The School of Graduate and Postdoctoral Studies
The University of Western Ontario
London, Ontario, Canada

© Corey A. Smith 2011

THE UNIVERSITY OF WESTERN ONTARIO
School of Graduate and Postdoctoral Studies

CERTIFICATE OF EXAMINATION

Supervisor

Examiners

Dr. Timothy A. Newson

Dr. Jim Johnson

Co-Supervisor

Dr. Grace Parraga

Dr. Kathleen A. Hill

Dr. William Hodge

Supervisory Committee

Dr. Cindy M. L. Hutnik

The thesis by

Corey Albert Smith

entitled:

**Development of Imaging Paradigms for
Drug Distribution and Fate in the Eye**

is accepted in partial fulfillment of the
requirements for the degree of
Master of Engineering Science

Date

Chair of the Thesis Examination Board

Co-Author Abstract

Aging-associated vision loss is increasingly prevalent in our population and intravitreal injections are commonly used to administer ocular drugs to the posterior segment of the eye. This work aims to visualize and predict the delivery of ocular drugs by combining micro-computed tomography (micro-CT) imaging and computational fluid dynamics (CFD) modeling. Intravitreal injections were administered into *ex vivo* porcine eyes and imaged for an extended period of time to track the progression of the injected drug mimic. Non-invasive imaging allowed for precise determination of contrast agent concentration, flow patterns and fate. A computational model was developed that provided quantitative agreement with the concentration values found in the experimental study and allowed for easy manipulation of parameters. The ability to accurately model drug transport following an intravitreal injection provides vital information to better understand the specific concentration and time frame for the drug to reach the target site.

Keywords: intravitreal injection, drug delivery, vitreous, diffusion, micro-computed tomography, computational fluid dynamics

Co-Authorship Statement

The work in Chapter 1 **CA Smith** is the sole author.

The work in Chapter 2 **CA Smith** is the sole author and completed all experimental work presented. TA Newson and KA Hill provided financial support and supervision.

The work in Chapter 3 is adapted from **Smith CA**, Newson TA, Leonard KC, Barfett J, Holdsworth DW, Hutnik CML and Hill KA. A novel framework for modeling ocular drug transport and flow through the eye using micro-CT. Submitted: April 2011. CA Smith performed the literature review, data acquisition, data analysis/ interpretation and preparation of the manuscript. KC Leonard and J Barfett completed the initial experimental design and pilot study. DW Holdsworth provided support for data acquisition and analysis. TA Newson, CML Hutnik and KA Hill provided assistance in experimental design/conception, obtaining funding and supervision. All authors contributed to editing and approval of the final manuscript.

The work in Chapter 4 is adapted from **Smith CA**, Newson TA, Hutnik CML and Hill KA. Micro-computed tomography imaging identifies anomalous features of intravitreal injections that impact drug delivery. Submitted: June 2011. CA Smith performed the literature review, data acquisition, data analysis/interpretation and preparation of the manuscript. TA Newson, CML Hutnik and KA Hill provided assistance in data interpretation, obtaining funding and supervision. All authors contributed to editing and approval of the final manuscript.

The work in Chapters 5 and 6 **CA Smith** is the sole author and completed all experimental work presented. TA Newson and KA Hill provided financial support and supervision.

Acknowledgments

This journey would not have been possible without the guidance and support from my supervisor Dr. Tim Newson. His ability to help make sense of the what appeared to be great challenges is an attribute I hope to have picked up. I appreciated the humour when I experienced frustrations and the continuing push for basic science interests. My co-supervisor, Dr. Kathleen Hill I owe a great deal of thanks to for her unwavering presence when I had questions and ability to deal with formalities of the academic world.

I owe special thanks to my advisor Dr. Cindy Hutnik who connected me with the Experimental Eye Research group in the beginning. Her enthusiasm and support is unprecedented and the constant encouragement and advice is inspirational. Her belief in me has inspired me to continue my studies.

I would like to thank the Biomedical Engineering Graduate Program for the support and environment that fosters scientific thinking and collaboration. Specifically, thanks to Diana Timmermans for always having an answer or solution to any administrative questions and a door always open. With her help, she has made my time in the program much smoother and more supportive. In addition, the financial support of The University of Western Ontario and CNIB Barbara Tuck MacPhee Research Award is gratefully acknowledged.

Thanks to my family for their love and pride as I continue my educational journey and for always supporting the decisions I make. To my fiancée, Katie: Much of the time over the past two years we were not in the same city, but I always had your unconditional love and support as I completed this work. I look forward to our future together and there is great comfort in knowing you appreciate science as much as I do.

Table of Contents

CERTIFICATE OF EXAMINATION	ii
Abstract.....	iii
Co-Authorship Statement.....	iv
Acknowledgments.....	v
Table of Contents	vi
List of Tables	x
List of Figures	xi
Abbreviations and Nomenclature	xiii
Chapter 1	1
1 Introduction.....	1
1.1 Background and Motivation	1
1.1.1 Eye Anatomy	2
1.2 Ocular Drug Delivery	4
1.2.1 Intravitreal Injections	5
1.2.2 Drugs Administered by Intravitreal Injection	5
1.3 Imaging	6
1.3.1 Micro-Computed Tomography	7
1.4 Computational Fluid Dynamics	8
1.5 Objectives	8
1.6 Hypotheses	9
1.7 Experimental Design.....	9
1.8 References.....	12
Chapter 2.....	16
2 Comparison of radiographic contrast agent drug mimics in the vitreous	16

2.1	Introduction.....	16
2.2	Materials and Methods.....	18
2.2.1	Micro-Computed Tomography	18
2.2.2	Contrast Agents.....	18
2.2.3	Intravitreal Injections	19
2.2.4	Imaging	20
2.2.5	Image Analysis.....	20
2.2.6	Estimation of Diffusion Coefficients	20
2.3	Results.....	21
2.3.1	Calibration.....	21
2.3.2	Contrast Dilution.....	24
2.3.3	Molecular Weight	26
2.4	Discussion	28
2.5	Conclusions.....	30
2.6	References.....	31
Chapter 3	33
3	A framework for modeling ocular drug transport and flow through the eye using micro-CT	33
3.1	Introduction.....	33
3.2	Materials and Methods.....	35
3.2.1	Micro-CT system	35
3.2.2	Injections and Scanning	36
3.2.3	Image Analysis.....	38
3.2.4	Calculation of Diffusion Coefficients.....	38
3.2.5	Reflective and Absorptive Boundaries	39
3.3	Results.....	40

3.4 Discussion.....	47
3.4.1 Capabilities of Micro-CT in Ocular Drug Transport Study.....	47
3.4.2 Modeling Ocular Drug Transport Using Experimental Data.....	48
3.4.3 Limitations	49
3.5 Conclusions.....	49
3.6 References.....	51
Chapter 4.....	54
4 Identification of anomalous features of intravitreal injections using micro-computed tomography	54
4.1 Introduction.....	54
4.2 Methods.....	55
4.2.1 Micro-Computed Tomography	55
4.2.2 Intravitreal Injections	56
4.2.3 Imaging	56
4.2.4 Image Analysis.....	57
4.3 Results.....	58
4.3.1 Air Bubbles	58
4.3.2 Bolus Shape	60
4.3.3 Injection Flow Rate.....	61
4.4 Discussion.....	63
4.5 Conclusions.....	66
4.6 References.....	67
Chapter 5.....	70
5 Modeling drug transport in the vitreous using computational fluid dynamics	70
5.1 Introduction.....	70
5.2 Methods.....	72

5.2.1	Initial Conditions	72
5.2.2	Governing Equations	72
5.2.3	Model Geometry	73
5.2.4	Boundary Conditions and Material Properties.....	74
5.2.5	Solution Method.....	75
5.3	Results.....	76
5.3.1	Validation of Model with Experimental Results	76
5.3.2	Effect of Diffusion Coefficients.....	77
5.3.3	Air Bubbles and Bolus Shape	80
5.3.4	Convection	81
5.4	Discussion	82
5.4.1	Translation to Human Model	84
5.5	Conclusions.....	84
5.6	References.....	85
Chapter 6	87
6	General Discussion and Conclusions	87
6.1	Summary	87
6.2	Limitations	89
6.3	Future Work	90
6.4	Significance.....	91
6.5	References.....	92
Appendix A	– Eye Planes/Orientation	93
Appendix B	– Contrast Agent ROIs	94
Appendix C	– Contrast Agent Bolus Signal Profiles.....	95
Appendix D	– MATLAB Implementation Code	96
Curriculum Vitae	99

List of Tables

Table 1.1 Age-related macular degeneration drugs	6
Table 2.1 Comparison of CT numbers for air and water	24
Table 2.2 Comparison of molecular weight and diffusion coefficient values	27
Table 4.1 Air bubble changes over time in the vitreous	59
Table 4.2 Injected bolus dimensions.....	61
Table 5.1 Dimension for model eye.....	73
Table 5.2 Model parameters for CFD model	75

List of Figures

Figure 1.1 Anatomy of a normal human eye.	2
Figure 1.2 Experimental design flow chart.....	11
Figure 2.1 Vials of contrast agents containing varying concentrations	22
Figure 2.2 CT number and concentration calibration plot.....	23
Figure 2.3 CT scan slices showing contrast agent in vitreous at time steps	25
Figure 2.4 Contrast agent dilution from the vitreous graphed over time.....	26
Figure 2.5 Diffusion coefficient and molecular weight linear regression	27
Figure 3.1 Enclosed container for <i>ex vivo</i> eyes in micro-CT scanner	37
Figure 3.2 Micro-CT image of <i>ex vivo</i> porcine eye	40
Figure 3.3 Isoshells representing concentrations in sagittal slice of micro-CT scan.....	41
Figure 3.4 Observed and predicted signal profile through bolus.....	42
Figure 3.5 Iodine solution diffusion coefficients.....	43
Figure 3.6 Gold nanoparticle diffusion coefficients	44
Figure 3.7 Reflective and absorbing diffusion.....	46
Figure 4.1 Air bubbles seen in micro-CT scan	58
Figure 4.2 Influence of time on air bubble volume	60
Figure 4.3 Bolus shapes shown in micro-CT images	61
Figure 4.4 Micro-CT images with needle in place during injection	62
Figure 4.5 Surface area of bolus compared with injection duration	63

Figure 5.1 Domain of vitreous transport model.....	74
Figure 5.2 Concentration at the center of the injected bolus	76
Figure 5.3 Concentration profiles from CFD model.....	78
Figure 5.4 Concentration gradient at boundary points for contrast agents	79
Figure 5.5 Concentration gradient at the macula for anomalous features	80
Figure 5.6 Convective flux and velocity fields in CFD model	81
Figure A.1 Planes used for orientation of the eye in analysis of micro-CT images.	93
Figure B.1 Isosurfaces representing the diffusing bolus over time.	94
Figure C.1 Line signal profiles through the bolus.	95

Abbreviations and Nomenclature

2D	Two-dimensional
3D	Three-dimensional
a	Initial radius
AMD	Age-related macular degeneration
C	Concentration
CFD	Computation fluid dynamics
CT	Computed tomography
D	Diffusion coefficient
EDTA	Ethylenediaminetetraacetic acid
Gd-EDTA	Gadolinium-diethylenetriaminopentaacetic acid
k	Decay constant
Mn ²⁺	Manganese ion
MRI	Magnetic resonance imaging
MW	Molecular weight
OCT	Optical coherence tomography
PBS	Phosphate buffered saline
r	Radius
S	Surface area
SD	Standard deviation
t	Time
U	Velocity vector
V	Volume
VEGF	Vascular endothelial growth factor

Chapter 1

1 Introduction

Developing greater insight and understanding into the processes involved in ocular drug delivery, particularly in the posterior segment of the eye, is vital information when developing drugs and drug delivery systems. This chapter provides the motivation of the work to be presented and background of eye anatomy, ocular drug delivery, imaging modalities and computational fluid dynamics. An outline of the hypothesis, objectives and experimental design provide the rationale of what will be presented in the following chapters.

1.1 Background and Motivation

Every 12 minutes someone in Canada develops significant vision loss. Vision loss accounts for the highest health care costs compared to any other disease in Canada, including diabetes, cardiovascular disease and cancer.¹ The leading cause of vision loss and legal blindness in people over the age of 50 in the developed world is age-related macular degeneration (AMD).^{2,3} AMD is a chronic degenerative disease that affects a small area at the back of the eye called the macula and it is this region of the eye that is responsible for central vision. Advanced stages of AMD cause complete loss of central vision, while some peripheral vision is maintained. A person's quality of life is significantly reduced when affected by vision loss, such as AMD.⁴⁻⁶ AMD and other ocular diseases associated with the posterior segment of the eye, such as diabetic retinopathy, macular edema and retinal vein occlusion, are commonly treated by administering injected drugs directly into the eye.

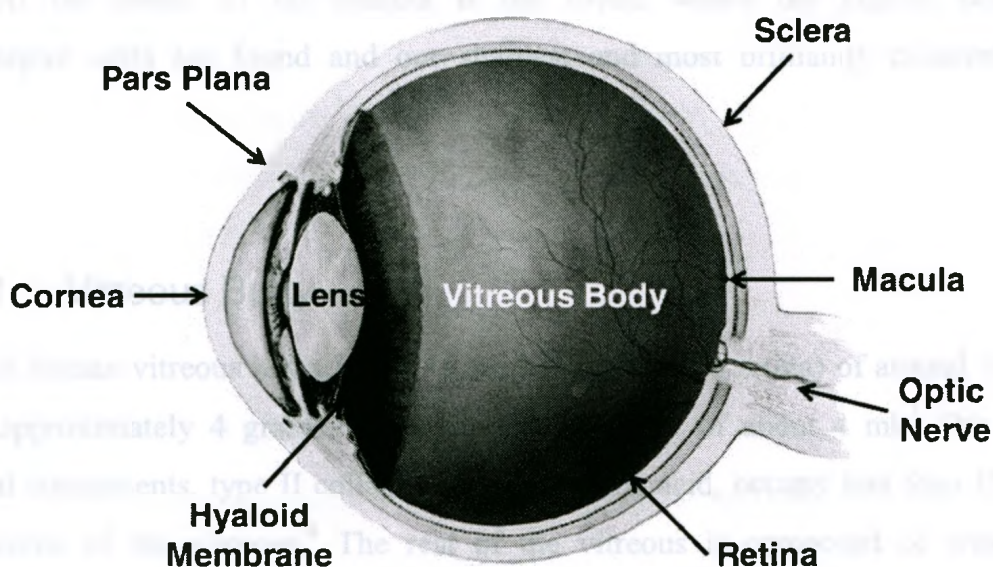


Figure 1.1 Anatomy of a normal human eye.

Adapted from: National Eye Institute, National Institutes of Health.

1.1.1 Eye Anatomy

Important anatomical features of the human eye for the purpose of this work are shown in Figure 1.1. Ocular anatomy is typically divided into two groups: anterior and posterior. The anterior region encompasses the region between the cornea and the lens. The cornea is the outermost layer of the anterior segment of the eye and is most useful in orienting the front of the eye. Light first passes through the cornea and then the lens, which focuses the light onto the back of the eye, specifically the retina. The posterior region includes the sclera, vitreous and retina. The sclera is the white covering of the eye that acts as a protective layer and helps maintain the shape. Within the eye is the vitreous cavity which contains the vitreous body (or humor), a jelly-like substance. The vitreous is enclosed by a membrane called the hyaloid membrane. The anterior hyaloid membrane separates the vitreous from the anterior chamber and the lens. An important function of the vitreous body is to hold the retina against the back of the eye. The retina is a very thin multi-layer of cells at the back of the eye that is responsible for detecting the light and transmitting the image to the brain via the optic nerve. The small specialized region of the retina

responsible for detailed central vision, called the macula, is located near the center of the retina. At the center of the macula is the fovea, where the highest density of photoreceptor cells are found and our sharpest and most brilliantly coloured vision occurs.

1.1.1.1 Vitreous Body

The adult human vitreous has a length (from back of lens to retina) of around 16.5 mm, weighs approximately 4 grams, and occupies a volume of about 4 ml.⁷ The primary structural components, type II collagen and hyaluronic acid, occupy less than 1% of the total volume of the vitreous.⁸ The rest of the vitreous is composed of water.⁹ The chemical composition of a typical human vitreous and the distribution of these components are not homogenous.¹⁰ The mature vitreous is a transparent gel with viscoelastic rheological properties. Rheological values for human vitreous have been shown to be a function of region.⁷ The normal human vitreous has a density close to that of water (1 g/ml) and a kinematic viscosity of approximately $1.4 \times 10^{-4} \text{ m}^2/\text{s}$. The normal postnatal vitreous is a homogenous gel and the fundamental aging process consists of a progressive disintegration of the gel structure, particularly at the center of the vitreous.¹¹ This process is termed vitreous liquefaction and starts early in life. Liquefied vitreous has a viscosity closer to $10^{-6} \text{ m}^2/\text{s}$.¹¹ The large volume and gel structure of the vitreous, consisting of several large molecular weight polymeric elements, suggests that its function is to provide a system that absorbs mechanical stress and protects the surrounding tissues during eye movement and physical activity. The vitreous accomplishes its mechanical function by securing the retina's adherence to the outer layers and filling up the vitreous chamber, and acting as a barrier between the anterior and posterior segments of the eye for heat and drug transport.⁷

There are several vitreous factors that affect the success or failure of drug delivery in the eye. The vitreous body is relatively inert connective tissue and is quite porous and thus transmits the pressure from the anterior chamber throughout the interior of the eye.¹² It has been observed that a needle hole in the sclera can affect transport between the

aqueous and vitreous bodies.¹³ Many existing works consider diffusion to be the greatest contributing factor to drug flow in the vitreous,^{14,15} over other transport mechanisms such as convection. The degree to which convection is responsible has been shown to vary with drug size and eye species.^{8,16} An important factor to consider when dealing with elderly patients is that their vitreous will be liquefied to some extent and may be less efficient as a transport barrier.¹¹

1.2 Ocular Drug Delivery

Drugs can be introduced into the eye by a variety of routes. The regions to which delivery of the drug is targeted and in which it is administered are divided in the same way as the eye is anatomically, into anterior and posterior. Drug delivery to the anterior region is typically administered by topical eye drops or subconjunctival injection and used to treat diseases such as glaucoma, infection and inflammation. Administration of drugs to the posterior region is accomplished using systemic administration, topical delivery and direct injection. Diseases that require administration of drugs to the posterior segment include AMD, diabetic retinopathy and uveitis.

Drug delivery in the eye poses a number of challenges including, but not limited to, corneal barrier,¹⁷ high aqueous humor turnover,¹⁸ blood-aqueous barrier and blood-retina barrier.¹⁹ Significant work has been devoted to developing and improving drug delivery systems for the eye. Methods that have been developed recently, but not yet common in clinical practice, include intraocular implants,²⁰ sustained release biodegradable implants,²¹ micro- and nanoparticle extended-release drugs²²⁻²⁴ and implantable intraocular pumps.²⁵ These remain as potential options in future clinical use, but all rely on the transport properties of drug flow in the vitreous. Combined with this reason and that intravitreal injections are currently very common in the clinic, intravitreal injections will be the route of choice in this study's experimentation.

1.2.1 Intravitreal Injections

The first choice for administering drugs to the posterior segment of the eye is via intravitreal injections.²⁶ Intravitreal injections are a direct needle injection into the eye through the region called the pars plana, where the cornea meets the sclera. The drug is administered into the human vitreous in volumes of 30-100 μ l. This volume of drug is expected to reach the target site, commonly the retina, by means of diffusion and convection. It has been estimated that intravitreal drug transport in humans is composed of 30% convective flow and the remainder diffusive flow.¹⁶ The challenge of intravitreal injections is due to the large diffusion distance in which the drug must travel. When administering a small volume of drug in a relatively large region, the challenge becomes the delivery of sufficient drug concentration to the correct region. The desirable fate of the drug is to be present at the target site, specifically the macula in treatment of AMD, at a therapeutic level of concentration for a sufficient time period without reaching levels of toxicity.^{27,28}

Intravitreal injections remain the most commonly used method of administering drugs to the posterior segment of the eye. Despite the invasive nature of the injections there is a low rate of complications, such as inflammation, cataract and retinal detachment, that result.^{29,30} The number of intravitreal injections being completed in Canada has increased dramatically since 2003. In Ontario between 2005 and 2007, the rate of intravitreal injections grew 8-fold from 3.5 to 25.9 injections per 100 000 patients per month.³¹ This has been attributed to the increased development of intraocular drugs, specifically those for the treatment of AMD.

1.2.2 Drugs Administered by Intravitreal Injection

Recent development of drugs for intravitreal injection have provided a variety of treatment options for diseases such as AMD. Each drug has unique properties, such as molecular weight, that may affect its transport properties in the vitreous. Table 1.1 lists the drugs used in the treatment of AMD via intravitreal injection and characteristics found in the prescribing information sheets.

Intravitreal injection volumes and doses administered in humans for the treatment of AMD range considerably between drugs. Taking into account the typical volume of vitreous in humans, this translates into a large difference in the concentration, from 3.47 to 25 mg/ml, in which the drugs listed in Table 1.1 are administered. The ability to optimize this concentration is vitally important in order to be effective in treating the disease while not reaching levels of toxicity.

Table 1.1 Age-related macular degeneration drugs

Characteristics of drugs used in treatment of age-related macular degeneration administered via intravitreal injection

Drug	Molecular Weight (kDa)	Volume (ul)	Concentration (mg/ml)	Dose (mg)
Pegaptanib (Macugen®) ³²	50	90	3.47	0.3
Bevacizumab (Avastin®) ³³	149	50	25	1.25
Ranibizumab (Lucentis®) ³⁴	48	50	10	0.5
Aflibercept (VEGF Trap-Eye)*	110	-	-	0.5 - 2

**Aflibercept (VEGF Trap-Eye, Regeneron Pharmaceuticals Inc) is currently in clinical trials for the treatment of AMD, diabetic macular edema and central retinal vein occlusion and specific prescribing information is not yet available*

1.3 Imaging

With the development of specialized imaging modalities such as molecular imaging, optical coherence tomography, positron emission tomography, magnetic resonance imaging (MRI) and micro-computed tomography (micro-CT), we are now able to non-invasively gain detailed information from biological systems. All modalities are useful tools in retrieving data on drug delivery, distribution and elimination. MRI is particularly useful for soft tissue imaging, but has limitations of low spatial resolution and long scan times,^{35,36} which are both very important components when studying ocular drug

delivery. In this study, micro-CT was chosen as the non-invasive imaging modality for tracking drug delivery in the eye for its high spatial resolution and fast scan time.

1.3.1 Micro-Computed Tomography

Micro-CT is an x-ray based imaging system that combines x-ray transmission with computed tomographical reconstruction to provide three-dimensional (3D) image volumes. An x-ray source transmits a beam of photons through the specimen and generates a set of 2D radiographs. These 2D radiographs are reconstructed into grey-scale images that are based on the tissue electron densities and level of photon absorption.³⁷ The set of 2D images are further reconstructed into a 3D volume for further analysis. CT contrast is achieved through the difference of the x-ray photon attenuation between materials. Attenuation is the decrease in the number of photons as the x-ray beam passes through material as a result of scattering or absorption. Heavy elements have a high attenuation primarily due to the absorption of the x-ray photons while soft tissue has a low attenuation due to the transmission of x-ray photons through the material. Attenuation therefore leads to image contrast in CT imaging.

For the purpose of this study, the delineation of anatomical features is not as important as visualizing the injected drug mimic. Major anatomical features such as the cornea, lens and sclera were all visible in the reconstructed CT images and provided useful landmark information. Radiopaque contrast agents with high atomic number and density, characteristics of high attenuation, were chosen to be used as drug mimics for clear differentiation from surrounding tissue and background. Specific concentrations can be measured by taking advantage of the linear relationship between attenuation and contrast agent concentration in x-ray imaging and is the basis of this study.^{38,39} Micro-CT has been shown to have the capabilities in providing advanced analytical techniques and detailed internal quantitative information to investigate drug delivery.⁴⁰

1.4 Computational Fluid Dynamics

Computational fluid dynamics (CFD) is a method of modeling fluid transport using numerical analysis. CFD is made up of three different disciplines: engineering (fluid dynamics), mathematics and computer science.⁴¹ Fluid dynamics encompasses the study of fluids either in motion or at rest and how they interact with other processes such as heat transfer and chemical reactions. Transport properties (i.e. diffusion coefficient, density, viscosity) are used to describe the fluid under study within the simulations in the mathematical equations. The mathematical equations are used to describe the fluid's characteristics, such as concentration and flux, based on the transport properties input into the equations. It is the computational aspect that combines it all together into an efficient software package.

The use of CFD for modeling ocular drug flow provides the capability to manipulate a variety of transport properties and investigate the extent to which they are important in the mechanisms of drug delivery. All of this can be completed without the use of animals or humans and allows for a cost-effective method of studying ocular drug flow. However, it is important to develop a CFD model that is based on experimental evidence and can be validated. With a physiologically relevant model, realistic predictions can be made by running a simulation and provide insight into ocular fluid dynamics that may not be realized in any other way.¹⁵

1.5 Objectives

The global objective of this work is to gain a better understanding, through the integration of imaging and modeling, of drug distribution and fate in the eye when administered to the posterior segment

The specific objectives are:

- To compare the x-ray compatibility and transport properties of contrast agents, acting as drug mimics, in the vitreous body of the eye.

- To characterize and understand the transport properties of a drug mimic in the vitreous body using micro-computed tomography imaging.
- To examine any unexpected characteristics arising from intravitreal injections that could impact ocular drug delivery.
- To develop a computational fluid dynamics model based on data from micro-computed tomography images.

1.6 Hypotheses

Transport properties will vary between contrast agents due to differences in molecular weight and will be able to be visualized and calculated using image analysis of micro-CT images. Imaging of the eyes before, after, and in some cases during injection, will allow for full assessment of the injection outcomes and reveal details of any potential complications. Computational fluid dynamics will provide a time dependent model of drug flow in the vitreous with concentration profiles that reflect those of the *ex vivo* imaging results.

1.7 Experimental Design

X-ray compatibility and transport properties will be assessed using micro-CT imaging. Measures of signal intensity, clearing time and diffusion coefficients will be analyzed and compared between differing contrast agents and concentrations. The iodinated contrast agent will be studied as a possible drug mimic and the gold nanoparticles will be studied as a drug mimic and as a drug tag. It is expected both contrast agents will provide visualization within the vitreous, but the transport properties, such as the diffusion coefficient, are expected to differ due to the material properties, such as the large difference in molecular weight between the two agents.

Micro-CT will allow for non-invasive analysis of an injected bolus of the drug mimic over an extended period of time. Each eye will be monitored for the full duration of the

scanning, providing a complete temporal data set per eye. Calculation and analysis of the diffusion coefficient will be completed and will be instrumental in understanding the mechanisms of diffusion in intravitreal drug transport.

Anomalous features have the potential to impact ocular drug delivery. Some characteristics not expected to be seen following an intravitreal injection are identified and analyzed. Air bubbles and their fate within the vitreous, needle tip movement during the injection resulting in an altered bolus shape and jetting from the tip of the needle, can all impact the transport of drugs in the vitreous. A better understanding of how they may influence drug flow and possible ways to eliminate them will be identified in an effort to optimize intravitreal injection techniques.

Utilizing the data acquired from non-invasive imaging, a computational fluid dynamics model is developed based on experimental results. Using the knowledge from the micro-CT experiments with that of the literature, a model of drug flow in the vitreous can be used to complete theoretical studies using different drug properties and eye parameters. It is expected the computational fluid dynamics model will provide strong correlation to the experimental results and allow for validation of the model. The combination of non-invasive imaging and computational fluid dynamics provides a unique combination of resources to study drug distribution and fate in the eye. Combining these methods with what is currently known of intravitreal injections and associated drugs, new methods and tools can be developed for studying intravitreal drug delivery.

1.8 References

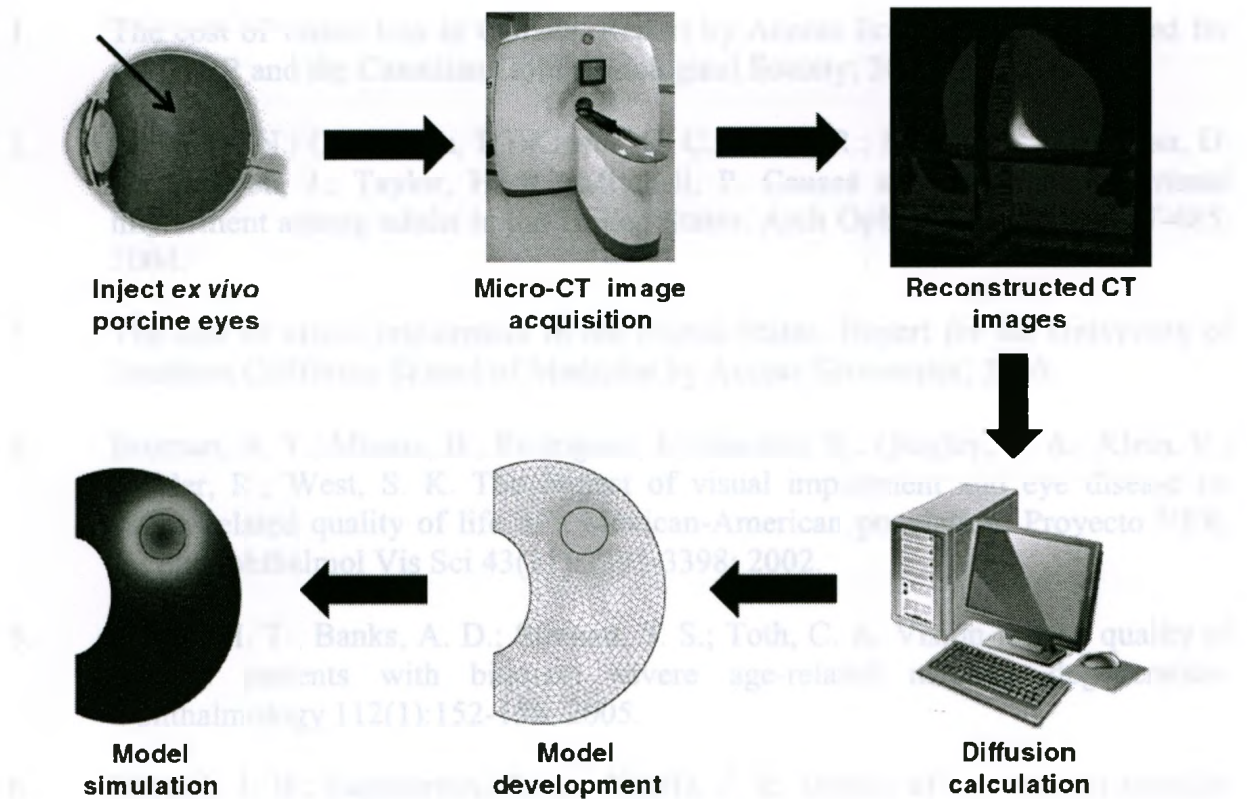


Figure 1.2 Experimental design flow chart

The general study design to address the objectives presented and create a link between non-invasive micro-CT imaging data and computational fluid dynamics modeling is shown in this flow chart.

1.8 References

1. The cost of vision loss in Canada. Report by Access Economics Pty Limited for the CNIB and the Canadian Ophthalmological Society; 2009.
2. Congdon, N.; O'Colmain, B.; Klaver, C. C.; Klein, R.; Munoz, B.; Friedman, D. S.; Kempen, J.; Taylor, H. R.; Mitchell, P. Causes and prevalence of visual impairment among adults in the United States. *Arch Ophthalmol* 122(4):477-485; 2004.
3. The cost of visual impairment in the United States. Report for the University of Southern California School of Medicine by Access Economics; 2006.
4. Broman, A. T.; Munoz, B.; Rodriguez, J.; Sanchez, R.; Quigley, H. A.; Klein, R.; Snyder, R.; West, S. K. The impact of visual impairment and eye disease on vision-related quality of life in a Mexican-American population: Proyecto VER. *Invest Ophthalmol Vis Sci* 43(11):3393-3398; 2002.
5. Cahill, M. T.; Banks, A. D.; Stinnett, S. S.; Toth, C. A. Vision-related quality of life in patients with bilateral severe age-related macular degeneration. *Ophthalmology* 112(1):152-158; 2005.
6. Hassell, J. B.; Lamoureux, E. L.; Keeffe, J. E. Impact of age related macular degeneration on quality of life. *Br J Ophthalmol* 90(5):593-596; 2006.
7. Lee, B.; Litt, M.; Buchsbaum, G. Rheology of the vitreous body. Part I: Viscoelasticity of human vitreous. *Biorheology* 29(5-6):521-533; 1992.
8. Stay, M. S.; Xu, J.; Randolph, T. W.; Barocas, V. H. Computer simulation of convective and diffusive transport of controlled-release drugs in the vitreous humor. *Pharm Res* 20(1):96-102; 2003.
9. Kaufman, P. L.; Alm, A.; Adler, F. H. Adler's physiology of the eye : clinical application. St. Louis: Mosby; 2003.
10. Theocharis, Achilleas D.; Papageorgakopoulou, N.; Feretis, E.; Theocharis, Dimitrios A. Occurrence and structural characterization of versican-like proteoglycan in human vitreous. *Biochimie* 84(12):1235-1241; 2002.
11. Stocchino, A.; Repetto, R.; Cafferata, C. Eye rotation induced dynamics of a Newtonian fluid within the vitreous cavity: the effect of the chamber shape. *Phys Med Biol* 52(7):2021-2034; 2007.
12. Ethier, C. R.; Johnson, M.; Ruberti, J. Ocular biomechanics and biotransport. *Annu Rev Biomed Eng* 6:249-273; 2004.
13. Maurice, D. M. Flow of water between aqueous and vitreous compartments in the rabbit eye. *Am J Physiol* 252(1 Pt 2):F104-108; 1987.

14. Tojo, K.; Isowaki, A. Pharmacokinetic model for in vivo/in vitro correlation of intravitreal drug delivery. *Adv Drug Deliv Rev* 52(1):17-24; 2001.
15. Kathawate, J.; Acharya, S. Computational modeling of intravitreal drug delivery in the vitreous chamber with different vitreous substitutes. *Int J Heat Mass Tran* 51(23-24):5598-5609; 2008.
16. Xu, J.; Heys, J. J.; Barocas, V. H.; Randolph, T. W. Permeability and diffusion in vitreous humor: implications for drug delivery. *Pharm Res* 17(6):664-669; 2000.
17. Liang, F. Q.; Viola, R. S.; del Cerro, M.; Aquavella, J. V. Noncross-linked collagen discs and cross-linked collagen shields in the delivery of gentamicin to rabbits eyes. *Invest Ophthalmol Vis Sci* 33(7):2194-2198; 1992.
18. Brubaker, R. F. Targeting outflow facility in glaucoma management. *Surv Ophthalmol* 48 Suppl 1:S17-20; 2003.
19. Cunha-Vaz, J.; Maurice, D. Fluorescein dynamics in the eye. *Doc Ophthalmol* 26:61-72; 1969.
20. Molokhia, S. A.; Sant, H.; Simonis, J.; Bishop, C. J.; Burr, R. M.; Gale, B. K.; Ambati, B. K. The capsule drug device: Novel approach for drug delivery to the eye. *Vision Res* 50(7):680-685; 2009.
21. Lee, S. S.; Hughes, P.; Ross, A. D.; Robinson, M. R. Biodegradable Implants for Sustained Drug Release in the Eye. *Pharm Res*:10; 2010.
22. Zhang, G.; Feng, X.; Wabner, K.; Fandrey, C.; Naqwi, A.; Wiedmann, T.; Olsen, T. W. Intraocular nanoparticle drug delivery: a pilot study using an aerosol during pars plana vitrectomy. *Invest Ophthalmol Vis Sci* 48(11):5243-5249; 2007.
23. Conley, S. M.; Naash, M. I. Nanoparticles for retinal gene therapy. *Prog Retin Eye Res* 29(5):376-397; 2010.
24. Rafie, F.; Javadzadeh, Y.; Javadzadeh, A. R.; Ghavidel, L. A.; Jafari, B.; Moogooee, M.; Davaran, S. In vivo evaluation of novel nanoparticles containing dexamethasone for ocular drug delivery on rabbit eye. *Curr Eye Res* 35(12):1081-1089; 2010.
25. Avery, R. L.; Saati, S.; Journey, M.; Caffey, S.; Varma, R.; Tai, Y. C.; Humayun, M. S. A novel implantable, refillable pump for intraocular drug delivery. The Association for Research in Vision and Ophthalmology Annual Meeting. Fort Lauderdale, Florida, USA; 2010.
26. Eljarrat-Binstock, E.; Pe'er, J.; Domb, A. J. New techniques for drug delivery to the posterior eye segment. *Pharm Res* 27(4):530-543; 2010.

27. Kwak, H. W.; D'Amico, D. J. Evaluation of the retinal toxicity and pharmacokinetics of dexamethasone after intravitreal injection. *Arch Ophthalmol* 110(2):259-266; 1992.
28. Rosenfeld, P. J.; Schwartz, S. D.; Blumenkranz, M. S.; Miller, J. W.; Haller, J. A.; Reimann, J. D.; Greene, W. L.; Shams, N. Maximum tolerated dose of a humanized anti-vascular endothelial growth factor antibody fragment for treating neovascular age-related macular degeneration. *Ophthalmology* 112(6):1048-1053; 2005.
29. Jager, R. D.; Aiello, L. P.; Patel, S. C.; Cunningham, E. T. J. Risks of intravitreal injection: a comprehensive review. *Retina* 24(5):676-698; 2004.
30. Jonas, J. B.; Spandau, U. H.; Schlichtenbrede, F. Short-term complications of intravitreal injections of triamcinolone and bevacizumab. *Eye* 22(4):590-591; 2008.
31. Campbell, R. J.; Bronskill, S. E.; Bell, C. M.; Paterson, J. M.; Whitehead, M.; Gill, S. S. Rapid expansion of intravitreal drug injection procedures, 2000 to 2008: a population-based analysis. *Arch Ophthalmol* 128(3):359-362; 2010.
32. Product monograph: Macugen. Pfizer Canada Inc.; 2005.
33. Product monograph: Avastin. Hoffmann-La Roche Ltd; 2005.
34. Prescribing information: Lucentis. Novartis Pharmaceuticals Canada Inc.; 2009.
35. Li, S. K.; Jeong, E. K.; Hastings, M. S. Magnetic resonance imaging study of current and ion delivery into the eye during transscleral and transcorneal iontophoresis. *Invest Ophthalmol Vis Sci* 45(4):1224-1231; 2004.
36. Kim, H.; Robinson, M. R.; Lizak, M. J.; Tansey, G.; Lutz, R. J.; Yuan, P.; Wang, N. S.; Csaky, K. G. Controlled drug release from an ocular implant: an evaluation using dynamic three-dimensional magnetic resonance imaging. *Invest Ophthalmol Vis Sci* 45(8):2722-2731; 2004.
37. Hounsfield, G. N. Computerized transverse axial scanning (tomography): Part 1. Description of system. *Br J Radiol* 46(552):1016-1022; 1973.
38. Kelsey, C. A. *Essentials of radiology physics*. St. Louis, Mo.: W.H. Green; 1985.
39. Novelline, R. A.; Squire, L. F. *Squire's fundamentals of radiology*, 5th ed. Cambridge, Mass.: Harvard University Press; 1997.
40. Wang, Y.; Wertheim, D. F.; Jones, A. S.; Coombes, A. G. A. Micro-CT in drug delivery. *Eur J Pharm Biopharm* 74(1):41-49; 2010.

Chapter 2

2 Comparison of radiographic contrast agent drug mimics in the vitreous

The purpose of the work presented in this chapter is to compare the x-ray compatibility and transport mechanisms of two contrast agents acting as drug mimics. Iodine based (Omnipaque™) and gold nanoparticle (AuroVist™) contrast agents were studied using micro-CT imaging. Comparisons of signal intensity, dilution in the vitreous and molecular weight are made to demonstrate their effectiveness in use as an intravitreal injection drug mimic or agent acting as a tag for a clinical drug.

2.1 Introduction

With an increasing number of intravitreal injections being administered¹ and more drugs being developed for use in the vitreous of the eye, there is a requirement to know the flow and fate patterns of these drugs. In studying ocular drug transport, it is vitally important to maintain the integrity of the eye and not disrupt its normal state. Non-invasive imaging is appropriate since it allows for each specimen to be used for its own control and can be longitudinally monitored.² This has been recently made possible with the development of non-invasive imaging techniques, such as micro-computed tomography (micro-CT). Micro-CT provides high resolution volumetric images, but provides poor soft tissue contrast. This limitation can be overcome using contrast-enhanced imaging to successfully visualize the transport of an injected solution.

An injected contrast agent can be utilized to achieve higher contrast within a CT image. Materials that have a higher atomic number (Z) have a higher contrast in x-ray imaging. Iodine ($Z = 53$) is a commonly used material as a radiographic contrast agent. Iodine's high atomic number means it is a heavy element and therefore has a higher attenuation coefficient. Iodinated solutions are an ideal contrast agent for clinical applications

because they are water soluble making them highly compatible with biological systems. Gold nanoparticles have recently become available as a new x-ray contrast agent. Gold has a higher atomic number (Au 79 vs. I 53) and a higher absorption coefficient (at 100 keV: gold $5.16 \text{ cm}^2/\text{g}$; iodine $1.94 \text{ cm}^2/\text{g}$; soft tissue $0.169 \text{ cm}^2/\text{g}$). This has been shown to account for about 3 times greater contrast per unit of weight of gold than iodine.³

Drug administration via intravitreal injection relies on the assumption that the injected drug will diffuse to the target site within the eye, rather than being injected at the exact site. This is the case since the target site is very delicate retinal tissue and is a very small location (5-6 mm macula diameter in humans). Since the drug must travel through the vitreous to the target site, it is important to be able to visualize the contrast agent post-injection within the eye for several hours. Long scan times require a contrast agent that will persist at a sufficient level of concentration to be imaged for the duration of the entire study. It is also important to keep the intravitreal injection clinically relevant and therefore at a volume that resembles that used clinically, which is approximately 50-100 μl for the human eye.⁴

Previous work has shown magnetic resonance imaging (MRI) can be used to monitor ocular drug delivery using compatible contrast agents.⁵⁻⁷ MRI contrast agents used in previous studies include manganese ion (Mn^{2+}), Mn^{2+} with ethylenediaminetetraacetic acid (EDTA) chelate and gadolinium-diethylenetriaminopentaacetic acid (Gd-DTPA). Mn^{2+} and MnEDTA^{2-} are both small ions that would have very different transport properties than macromolecules. Gd-DTPA is a macromolecule that should more closely represent the flow characteristics of drugs used in intravitreal injections. MRI studies are limited in that the spatial resolution may not be high enough to determine the concentration or small volume of drug surrogates in thin tissues less than 0.3mm.⁸

This study utilizes a non-invasive imaging modality that allows for rapid scan time and high resolution. The purpose of this work is to compare the x-ray compatibility and transport mechanisms of contrast agents acting as drug mimics as they flow through the vitreous body of the eye. This is accomplished by the objectives of this work which are to determine if gold nanoparticles are a useful radiographic contrast agent for visualizing an

injected bolus within an eye over time and to determine the optimal range of concentrations to use for intravitreal injections when studying drug transport and flow in the eye.

2.2 Materials and Methods

2.2.1 Micro-Computed Tomography

Micro-computed tomography (micro-CT) scanning was performed using a pre-clinical system (eXplore Locus Ultra, General Electric Healthcare Bioscience, London, Ontario, Canada). The system provides the fast-scanning speed of a clinical scanner with the high resolution of micro-CT and is designed for small animal experiments. It is this system that will be utilized in future *ex vivo* and *in vivo* experiments looking at drug delivery in the eye. A flat-panel detector mounted on a slip-ring CT gantry was used to acquire 3D volumetric data in 8-16 seconds with an isotropic spatial resolution of 150 μm . The x-ray tube voltage and beam current were kept constant during the experiments at 80 kVp and the 80 mA, respectively.

2.2.2 Contrast Agents

Two commercially available contrast agents were chosen for this study. Iodine based iohexol (Omnipaque™ 300, GE Healthcare, Oakville, Ontario, Canada) was chosen because of its common use as a radiographic contrast agent both clinically and experimentally and is very economical. Omnipaque 300 contains 300 mg of iodine per milliliter and has the molecular weight of 821 g/mol. It has an osmolarity of 465 mOsm/L, absolute viscosity of 6.3 at 37°C and specific gravity of 1.349 at 37°C.

Gold nanoparticles (AuroVist™ 1102, Nanoprobes Inc, Yaphank, New York, USA) were chosen as they have been shown to provide higher contrast at lower concentrations.³ The molecular weight of gold nanoparticles is much higher than iodine (50 kDa vs. 0.82 kDa) and studies have shown this to attribute to a slower clearing time in biological systems.³ This provides for a longer period of contrast detection at a lower initial concentration. In

addition, the 1.9 nm gold nanoparticles have a similar molecular weight as the most common anti-VEGF drugs used to treat AMD.

2.2.2.1 Iodine and Gold Concentration Standards

Concentration standards were made using vials of varying iodine concentrations. Solutions were prepared in the following concentrations: 300, 150, 75, 37.5, 18.75 and 9.375 mg/ml. The 300 mg/ml sample was full strength Omnipaque 300. The 150 mg/ml solution was prepared by diluting 100 μ l of full strength Omnipaque 300 with 100 μ l of Phosphate Buffered Saline (PBS) 1x concentration. To prepare the 75 mg/ml solution 25 μ l of Omnipaque 300 was diluted with 75 μ l of PBS, the 37.5 mg/ml solution was 12.5 μ l Omnipaque to 87.5 μ l PBS, the 18.75 mg/ml solution was 6 μ l Omnipaque to 94 μ l PBS and the 9.375 mg/ml solution was 3 μ l Omnipaque to 97 μ l PBS. Two additional vials of deionized water and air were included to assist with signal intensity calibration.

For concentration standards of gold nanoparticle solutions were prepared in the following concentrations: 200, 134, 67, 33.5, 16.75 and 8.375 mg/ml. The 200 mg/ml solution was prepared by diluting the 40 mg vial of gold nanoparticle powder with 200 μ l of PBS. The 134 mg/ml solution was prepared by taking 100 μ l of the 200 mg/ml solution and diluting it with 50 μ l of PBS. This 1:1 dilution process was repeated to make the remaining concentration solutions. Two additional vials of deionized water and air were included to assist with signal intensity calibration.

2.2.3 Intravitreal Injections

Freshly harvested enucleated porcine eyes were obtained from a local abattoir and used within 10 hours postmortem. During scanning and for the remainder of the study, they were maintained at 24°C (+/- 2°C). Pre-injection scans confirmed no abnormalities in any eyes. Iodinated and gold nanoparticle contrast agents were used as drug mimics at varying concentrations. Clinically relevant intravitreal injections of a 30 μ l volume of contrast agent were administered into 24 enucleated eyes. The injection volume of 30 μ l was calculated based on the smaller vitreous volume of the pig eye compared to that of the human. Injections were performed 2-3 mm posterior to the superotemporal limbus at

a depth of 1 cm using 29-gauge needles (SS05M2913, Terumo Medical Corporation, Somerset, NJ, USA).

2.2.4 Imaging

Scans were acquired up to 230 minutes (the anticipated time for the contrast agent to remain at sufficient concentration and/or reach the retina) following the injection to allow for visualization of the contrast agent's progression through the vitreous. Concentration standards were included in the scans for calibration purposes.

2.2.5 Image Analysis

3D computed tomography visualization and analysis software (MicroView 2.1.2, GE Healthcare, London, Ontario, Canada) was used to analyze the reconstructed CT images. The CT number and standard deviation for each concentration sample in the concentration standards were recorded. Measurements were taken from the center of each vial in a $2 \times 2 \times 2 \text{ mm}^3$ region of interest and recorded in Hounsfield units (HU). Linear regression analysis was used to determine the relationship between signal intensity and contrast agent concentration. This was completed for both iodine and gold nanoparticle samples.

2.2.6 Estimation of Diffusion Coefficients

The diffusion coefficient of OmnipaqueTM in the vitreous was estimated using the Wilke-Chang correlation,⁹ since that value was not available from published literature. An estimate was made based on Gd-DTPA, which has a similar molecular weight (936.0 g/mol vs. 821.1 g/mol). The diffusivity of Gd-DTPA in water is known to be $2.6 \times 10^{-10} \text{ m}^2/\text{s}$.¹⁰ The following correlation equation can be derived if it is assumed that the molar volume of each species at its normal boiling point is proportional to its molecular weight,¹¹

$$\frac{D_{\text{Omnipaque}}}{D_{\text{Gd-DTPA}}} = \left(\frac{MW_{\text{Gd-DTPA}}}{MW_{\text{Omnipaque}}} \right)^{0.6} \quad (2.1)$$

which yields $2.8 \times 10^{-10} \text{ m}^2/\text{s}$ for Omnipaque in water. Since the vitreous is composed of more than 99% water,¹² this assumption was thought to be reasonable.

There is no empirical data to date for the diffusion coefficient of gold nanoparticles (AuroVist™ 1.9 nm). Since the particles are close to spherical and are much larger than the water molecules around them, the diffusion coefficient in water can be modeled using the Stokes-Einstein equation,¹³

$$D = \frac{RT}{6\pi\eta rN} \quad (2.2)$$

where R is the gas constant (8.3145 J/mol K), T is the absolute temperature (room temperature = 295 K), η is the viscosity of the diffusing medium (0.001002 kg/m s), r is the radius of the diffusing particle (1.5 nm) and N is Avogadro's number (6.0221×10^{23} per mole). The calculated value for 1.9 nm gold nanoparticles in water is $1.44 \times 10^{-10} \text{ m}^2/\text{s}$ with the assumption no aggregation occurs. This will be used as a comparison value to those calculated for gold nanoparticles in the vitreous.

2.3 Results

2.3.1 Calibration

Calibration of the signal intensity with contrast agent concentration was determined using the standards of various concentrations. The concentrations of both iodine (Omnipaque™) and gold nanoparticles (AuroVist™) along with air and deionized water are shown in Figure 2.1.

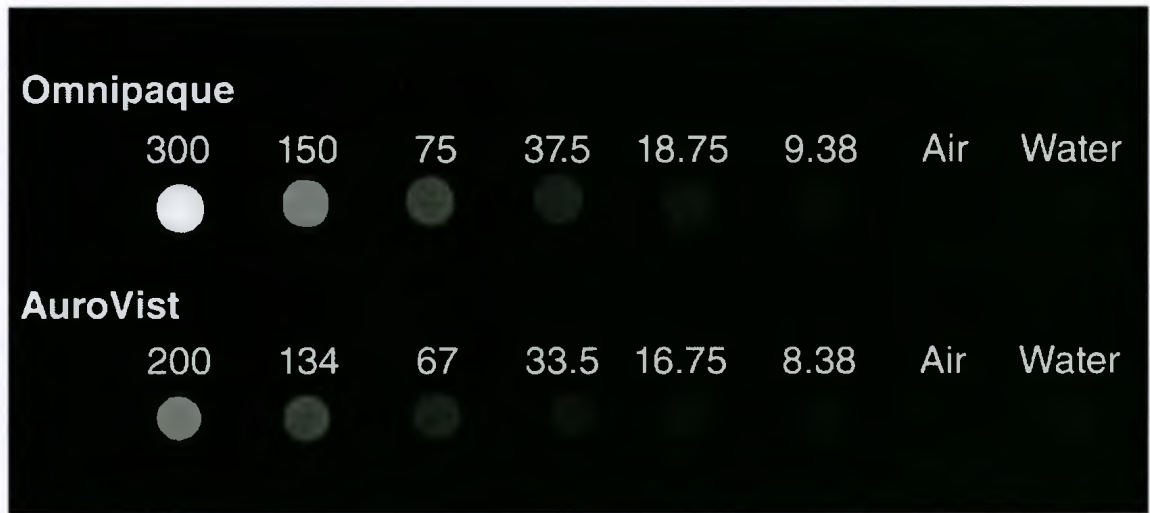


Figure 2.1 Vials of contrast agents containing varying concentrations

Reconstructed CT image of the calibration standards with vials of iodine (Omnipaque) in the following concentrations 300, 150, 75, 37.5, 18.75, 9.38 mg/ml and gold nanoparticles in the following concentrations 200, 134, 67, 33.5, 16.75, 8.38 mg/ml. Vials of air and deionized water were also included with each sample for CT number (HU) calibration.

The signal intensity, CT number (HU), is shown as a function of contrast agent concentration (mg/ml) in Figure 2.2 for both iodine and gold nanoparticles. Linear regression results for iodine can be expressed as an equation $S = 31.9 \text{ ml/mg} \times C_i + 956.0 \text{ HU}$, where S is the signal intensity and C_i is the iodine concentration in mg/ml ($r^2 = 0.9892$). For gold nanoparticles the result of linear regression is $S = 31.0 \text{ ml/mg} \times C_g + 61.1 \text{ HU}$ ($r^2 = 0.9993$), where C_g is the gold nanoparticle concentration. These results are indicative of a highly linear system ($p < 0.01$ and $p < 0.0001$, respectively). The y-intercept is expected to be zero and for both contrast agents it was significantly different. This was also reported by Du *et al.* that indicated the micro-CT scanner calibration may need to be adjusted,¹⁴ but does not impact the results presented herein as our custom concentration standards were used for calibration of the CT number with contrast agent concentration.

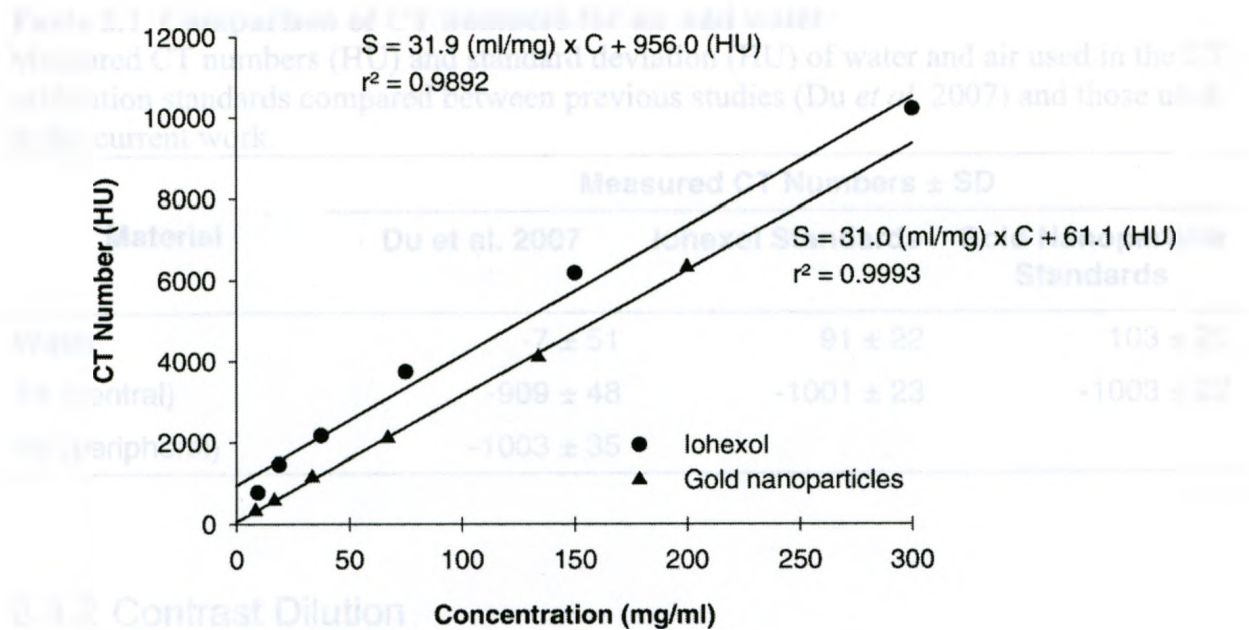


Figure 2.2 CT number and concentration calibration plot

Plot of measured CT number (signal intensity) versus known contrast agent concentrations (circles, iodinated Omnipaque™; triangles, gold nanoparticle AuroVist™). Linear regression results indicate a significant correlation is seen between signal intensity and concentration for both contrast agents.

Calibration findings were compared to that of a study performed using the same micro-CT scanner and a custom made multiple parameter quality assurance phantom.¹⁴ The linearity of the system was comparable between the two studies as all cases of concentration standards exhibited strong linear regression. Measurements of signal intensity in the water and air samples provided values shown in Table 2.1.

Table 2.1 Comparison of CT numbers for air and water

Measured CT numbers (HU) and standard deviation (HU) of water and air used in the CT calibration standards compared between previous studies (Du *et al.* 2007) and those used in the current work.

Material	Measured CT Numbers \pm SD		
	Du et al. 2007	Iohexol Standards	Gold Nanoparticle Standards
Water	-7 ± 51	91 ± 22	103 ± 23
Air (central)	-909 ± 48	-1001 ± 23	-1003 ± 22
Air (peripheral)	-1003 ± 35		

2.3.2 Contrast Dilution

The contrast agent in the eye was evaluated to determine if it was present at a sufficient concentration to be detected for an extended period of time. Iodine solutions and gold nanoparticles were monitored for up to 230 minutes at varying concentrations. The same sagittal plane images of two specimens, one with an injection of iodine solution and one with an injection of gold nanoparticles, were compared at the time points 8, 35, 195 minutes (Figure 2.3). Despite a small difference in initial concentration (37 mg/ml vs. 25 mg/ml) both specimens exhibited similar visualization of concentration at the respective time points.

Quantitative analysis was completed using measured signal intensity values taken from scans at each time point. The results are shown in Figure 2.4 with the maximum detectable signal, representing the concentration within the scan, plotted against time. Various concentrations were plotted to determine how the clearing profiles differed between concentrations. The background signal in the image from vitreous had a mean of 210 ± 65 HU and was included in the graph. The iodine and gold nanoparticle solutions were easily detectable at a signal intensity of greater than 500 HU.

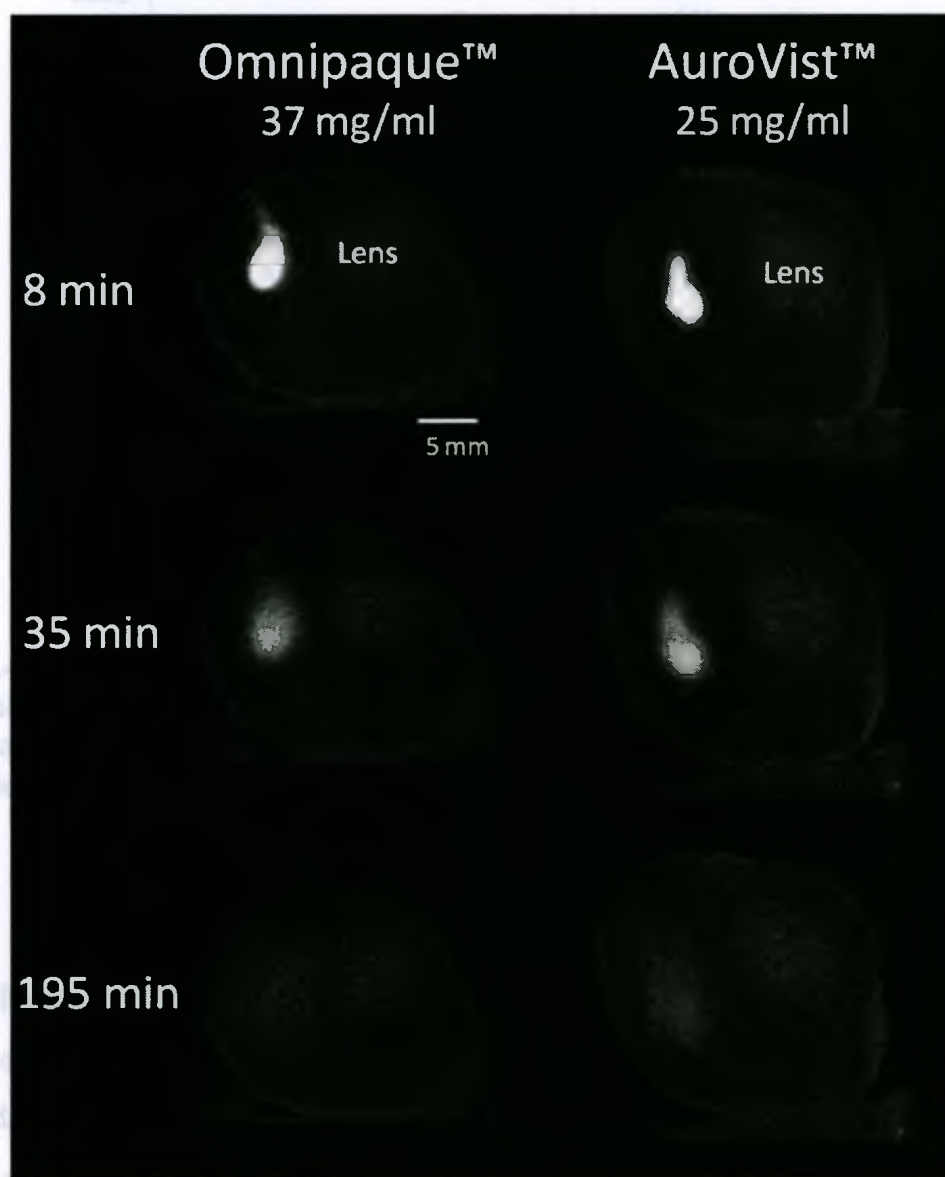


Figure 2.3 CT scan slices showing contrast agent in vitreous at time steps

Comparison of reconstructed micro-CT images taken in the same plane (sagittal) and location at time points 8, 25 and 195 minutes between iodine based Omnipaque™ (37 mg/ml) and gold nanoparticle based AuroVist™ (25 mg/ml) indicates there is very little difference in visualization of contrast between the two.

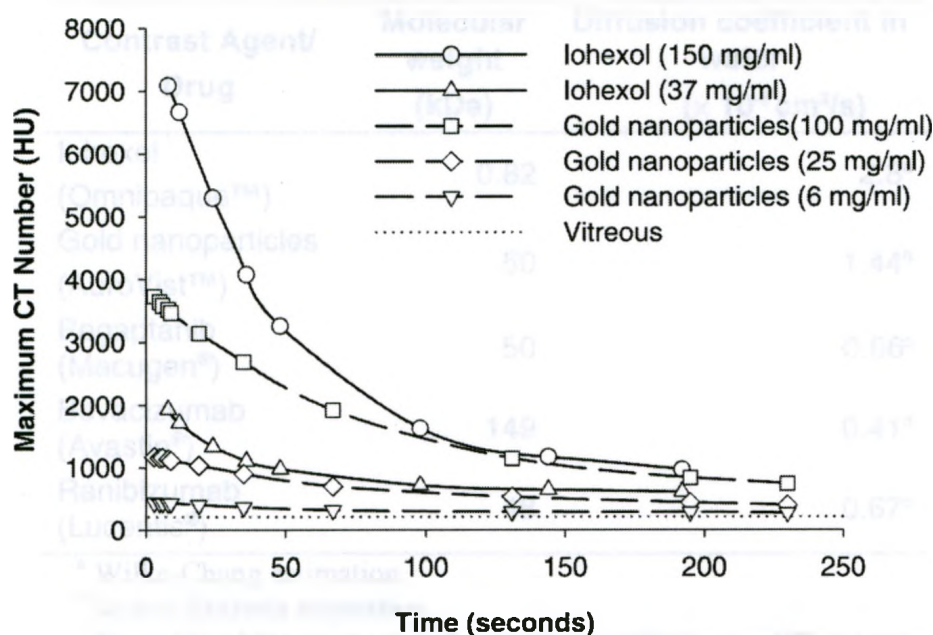


Figure 2.4 Contrast agent dilution from the vitreous graphed over time

Comparison of contrast agent dilution within the vitreous based on the maximum detectable pixel value (HU) at each time point indicates iohexol (Omnipaque™) and gold nanoparticles (AuroVist™) follow different trends.

2.3.3 Molecular Weight

The molecular weight of the contrast agents and common intravitreal drugs were compared alongside calculated diffusion coefficients (Table 2.2). Molecular weight values were taken from product literature and diffusion coefficients were calculated experimentally or taken from literature. Figure 2.5 shows the diffusion coefficients on a logarithmic scale as a function of the molecular weight. The linear regression result is also shown with the equation $\log(D) = -4.99 \times 10^{-3} \text{ 1/kDa} \times MW + 0.27 \text{ cm}^2/\text{s}$ ($r^2 = 0.674$). This shows that there is not a very strong linear relationship for the data points used, but the values do lie within the 95% confidence interval.

Table 2.2 Comparison of molecular weight and diffusion coefficient values

Diffusion coefficient values of Omnipaque™ and AuroVist™ are based on and intravitreal drug values are based on literature and calculations.

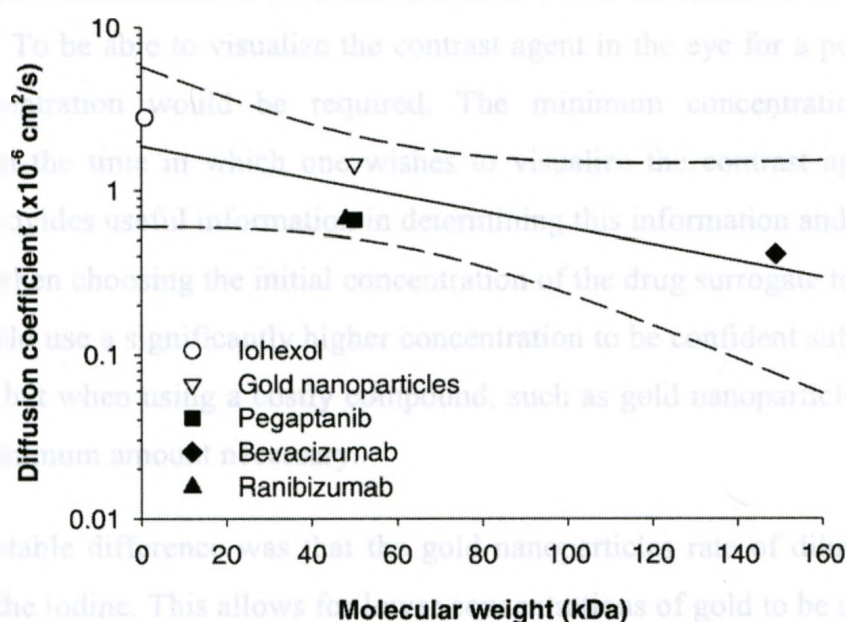
Contrast Agent/ Drug	Molecular weight (kDa)	Diffusion coefficient in water ($\times 10^{-6} \text{ cm}^2/\text{s}$)
Iohexol (Omnipaque™)	0.82	2.8 ^a
Gold nanoparticles (AuroVist™)	50	1.44 ^b
Pegaptanib (Macugen®)	50	0.66 ^c
Bevacizumab (Avastin®)	149	0.41 ^d
Ranibizumab (Lucentis®)	48	0.67 ^d

^a Wilke-Chang estimation

^b Stokes-Einstein estimation

^c From Molokhia *et al.* using free aqueous diffusion coefficient estimation

^d From S.K. Li *et al.* using dynamic light scattering measurements at 25°C

**Figure 2.5 Diffusion coefficient and molecular weight linear regression**

The relationship between diffusion coefficient (cm^2/s) and molecular weight (kDa) using values from Table 2.2, $r^2 = 0.674$. Dashed lines indicate 95% confidence interval.

2.4 Discussion

Both contrast agents provided statistically significant linearity ($p < 0.01$) in signal intensity and concentration analysis, as was expected and shown in previous work.¹⁴ Calibration is an important quality assurance step to the analysis of contrast agents, especially when concentration information will be derived from the scans. It is also vitally important not to rely on the same results for each successive scan (whether on the same day or not). A simple and useful approach to receiving calibration information with each scan is to include samples of diluted contrast agent vials, as was completed in this study, with the specimen of interest and in the scanner's field of view. The vials that were made up for this study will be used in successive experiments looking at drug transport following porcine eye injections.

The iodine and gold nanoparticle solutions can be detected at concentrations of 9 mg/ml and 3 mg/ml and greater, respectively, in the porcine eye. This is calculated using the upper limit of the 95% confidence interval of the background (vitreous) and allows for clear differentiation. Similar results were achieved of significantly higher contrast from gold nanoparticles compared to iodinated solutions when equivalent molar concentrations were used.¹⁵ To be able to visualize the contrast agent in the eye for a period of time, a higher concentration would be required. The minimum concentration required is dependent on the time in which one wishes to visualize the contrast agent. However, Figure 2.4 provides useful information in determining this information and can be used as a reference when choosing the initial concentration of the drug surrogate to inject into the eye. One could use a significantly higher concentration to be confident sufficient contrast is achieved, but when using a costly compound, such as gold nanoparticles, it is desired to use the minimum amount necessary.

The most notable difference was that the gold nanoparticles rate of dilution was lower than that of the iodine. This allows for lower concentrations of gold to be used in order to obtain the same degree of signal intensity higher iodine concentrations would achieve. This appeared to be in part due to the larger molecular weight of the gold nanoparticles (50 kDa for gold nanoparticles vs. 0.82 kDa for iodine), since they do not move through the vitreous as quickly. This observation has been shown before in pharmacokinetic

studies.^{16,17} This is an important characteristic to point out as the molecular weight of gold nanoparticles is the same or very similar to intravitreal drugs. Therefore, gold nanoparticles acting as a drug surrogate provide a more representative example of how an intravitreal drug such as Macugen[®] or Lucentis[®] would be transported in the eye. A comparison of the molecular weight, typical injection volume, concentration and dosage between surrogate contrast agents used in this study and common AMD drugs are described in Table 1.1.

Gold nanoparticles allow for tagging to other agents, such as fluorescein and anti-bodies. This provides greater capabilities in that multiple imaging modalities could be used to investigate the drug flow, such as fluorescence microscopy or molecular imaging.³ Custom contrast agents could be developed where the gold nanoparticles are bound to an ocular drug (ex. anti-VEGF) that would target the site of retinal disease (ex. macula). Gold is available in a variety of sizes and forms, which would influence the visualization and clearing properties. This also provides greater options in choosing a drug surrogate and matching the properties to a specific drug.

A limitation of this work is the assumption that the contrast agents used act in the same way as ocular pharmaceutical drugs used clinically. This was addressed by finding a solution that was comparable in molecular weight to the most commonly used AMD drugs. Molecular weight is only one pharmacokinetic property of a drug that may affect its relationship with the vitreous, others include surface chemistry and drug elimination.¹⁸ Since these findings are being used to investigate drug flow through the vitreous and molecular weight has been shown to be a major influence on the drug's elimination from the vitreous,^{17,19} it can be assumed the contrast agents and ocular drugs would follow similar pharmacokinetics.

2.5 Conclusions

The necessary concentration and signal intensity information has been obtained allowing for a direct comparison of iodine and gold nanoparticle solutions. It has been shown gold nanoparticles have the ability to sustain contrast over an extended period of time, can be used at lower concentrations than iodinated contrast agents, and closely resemble the ophthalmological drug's molecular weight. However, both iodine and gold nanoparticle contrast agents can be successfully used to track a bolus through the vitreous and permit more accurate predictions of the flow and transport mechanisms of intravitreal drug delivery.

2.6 References

1. Campbell, R. J.; Bronskill, S. E.; Bell, C. M.; Paterson, J. M.; Whitehead, M.; Gill, S. S. Rapid expansion of intravitreal drug injection procedures, 2000 to 2008: a population-based analysis. *Arch Ophthalmol* 128(3):359-362; 2010.
2. Graham, K. C.; Detombe, S. A.; MacKenzie, L. T.; Holdsworth, D. W.; MacDonald, I. C.; Chambers, A. F.; Drangova, M. Contrast-enhanced microcomputed tomography using intraperitoneal contrast injection for the assessment of tumor-burden in liver metastasis models. *Invest Radiol* 43(7):488-495; 2008.
3. Hainfeld, J. F.; Slatkin, D. N.; Focella, T. M.; Smilowitz, H. M. Gold nanoparticles: a new X-ray contrast agent. *Br J Radiol* 79(939):248-253; 2006.
4. Rodrigues, E. B.; Rossi, E. E.; Grumann Junior, A.; Meyer, C. H.; Ho, A. C. Treatment of neovascular age-related macular degeneration with antiangiogenic drugs. *Arq Bras Oftalmol*. 69:756-765; 2006.
5. Li, S. K.; Jeong, E. K.; Hastings, M. S. Magnetic resonance imaging study of current and ion delivery into the eye during transscleral and transcorneal iontophoresis. *Invest Ophthalmol Vis Sci* 45(4):1224-1231; 2004.
6. Kim, H.; Robinson, M. R.; Lizak, M. J.; Tansey, G.; Lutz, R. J.; Yuan, P.; Wang, N. S.; Csaky, K. G. Controlled drug release from an ocular implant: an evaluation using dynamic three-dimensional magnetic resonance imaging. *Invest Ophthalmol Vis Sci* 45(8):2722-2731; 2004.
7. Molokhia, S. A.; Jeong, E. K.; Higuchi, W. I.; Li, S. K. Examination of penetration routes and distribution of ionic permeants during and after transscleral iontophoresis with magnetic resonance imaging. *Int J Pharm* 335(1-2):46-53; 2007.
8. Li, S. K.; Lizak, M. J.; Jeong, E. K. MRI in ocular drug delivery. *NMR Biomed* 21(9):941-956; 2008.
9. Wilke, C. R.; Chang, P. Correlation of diffusion coefficients in dilute solutions. *AIChE Journal* 1(2):264-270; 1955.
10. Gordon, M. J.; Chu, K. C.; Margaritis, A.; Martin, A. J.; Ethier, C. R.; Rutt, B. K. Measurement of Gd-DTPA diffusion through PVA hydrogel using a novel magnetic resonance imaging method. *Biotechnol Bioeng* 65(4):459-467; 1999.
11. Xu, J.; Heys, J. J.; Barocas, V. H.; Randolph, T. W. Permeability and diffusion in vitreous humor: implications for drug delivery. *Pharm Res* 17(6):664-669; 2000.
12. Kaufman, P. L.; Alm, A.; Adler, F. H. *Adler's physiology of the eye : clinical application*. St. Louis: Mosby; 2003.

13. Miller, C. C. The Stokes-Einstein Law for Diffusion in Solution. Proceedings of the Royal Society of London. Series A 106(740):724-749; 1924.
14. Du, L. Y.; Umoh, J.; Nikolov, H. N.; Pollmann, S. I.; Lee, T. Y.; Holdsworth, D. W. A quality assurance phantom for the performance evaluation of volumetric micro-CT systems. *Phys Med Biol* 52(23):7087-7108; 2007.
15. Jackson, P. A.; Rahman, W. N.; Wong, C. J.; Ackerly, T.; Geso, M. Potential dependent superiority of gold nanoparticles in comparison to iodinated contrast agents. *Eur J Radiol*; 2009.
16. Bakri, S. J.; Snyder, M. R.; Reid, J. M.; Pulido, J. S.; Singh, R. J. Pharmacokinetics of intravitreal bevacizumab (Avastin). *Ophthalmology* 114(5):855-859; 2007.
17. Bakri, S. J.; Snyder, M. R.; Reid, J. M.; Pulido, J. S.; Ezzat, M. K.; Singh, R. J. Pharmacokinetics of intravitreal ranibizumab (Lucentis). *Ophthalmology* 114(12):2179-2182; 2007.
18. Choonara, Y. E.; Pillay, V.; Danckwerts, M. P.; Carmichael, T. R.; du Toit, L. C. A review of implantable intravitreal drug delivery technologies for the treatment of posterior segment eye diseases. *Journal of Pharmaceutical Sciences* 99(5):2219-2239; 2010.
19. Kamei, M.; Misono, K.; Lewis, H. A study of the ability of tissue plasminogen activator to diffuse into the subretinal space after intravitreal injection in rabbits. *American Journal of Ophthalmology* 128(6):739-746; 1999.

Chapter 3

3 A framework for modeling ocular drug transport and flow through the eye using micro-CT

This chapter describes the experimental design and analysis of micro-CT imaging data for assessment of concentration and transport mechanisms of ocular drug mimics following intravitreal injection. Diffusion coefficients of the injected iodine and gold nanoparticle solutions were estimated using non-linear regression analysis with a diffusion model. There was a predominantly diffusive component in the movement of the contrast to the back of the eye in the horizontal (sagittal & coronal) directions, with ultimate retinal fate observed after 120 minutes. A real-time, accurate, non-invasive method of tracking a bolus and its concentration was achieved using a high spatial resolution and fast scanning speed micro-CT system.

3.1 Introduction

In a clinical environment, ocular drugs are often delivered topically as an aqueous eye drop solution or by direct intravitreal injection. These delivery methods are inherently pulsed with a short period of overdosing followed by a long period of underdosing.¹ As many drugs have a narrow therapeutic window of effectiveness and may be toxic at higher concentrations,² the ability to predict local drug concentrations is necessary for proper loading of the delivery system.³ However, it has proven difficult to track and predict drug flow and fate *in vivo*. Many drug delivery strategies are accepted because of proven efficacy and an acceptable incidence of complications, but not based on a thorough knowledge of the specific pharmacokinetic properties of the eye and so

potentially remain under-optimized. Though there is ample evidence to indicate that the various therapeutic agents administered via intravitreal injection have an effect at the retina,⁴⁻⁷ the details of drug delivery, transport and fate remain elusive. While there are complications associated with intravitreal injections,⁸ it remains the route of choice for administering certain therapeutic agents.^{9,10}

The distribution of injected compounds in the vitreous has been studied both theoretically and experimentally.¹¹⁻¹⁴ The first study to show experimentally measured concentration distribution in the vitreous assessed the concentration of various injected fluorophores in frozen sections of the vitreous.¹¹ This model included examination of the effects of intravitreal injection position and volume.¹⁵ Pharmacokinetic analyses of intravitreal injections using bevacizumab (Avastin®) and ranibizumab (Lucentis®), two common vascular endothelial growth factors (VEGF) inhibitors, have been conducted in rabbit eyes.^{16,17} These studies involved euthanization of rabbits at various time points following drug injection and measurement of drug concentrations in the aqueous fluid, whole vitreous and serum. While such pharmacokinetic studies have yielded important information, they provide little understanding of drug transport mechanisms through the vitreous and retinal drug concentrations. A recent technique to examine molecular tracer distribution in the vitreous involves snap freezing the whole globe to isolate the vitreous after superficial thawing.¹⁸ This approach provides more information regarding vitreal transport kinetics, but remains limited since it requires enucleation and significant eye processing prior to drug transport assessments.

The techniques presented above have several important limitations. Those which involve the use of fluorophores or dyes have the disadvantage of requiring enucleation for analysis to re-enact the movement of the substance *in vivo*. Most importantly, these approaches also prevent real time or serial time point studies, and are unable to provide drug transport gradients from the eyes of individual animals.¹⁹ Magnetic resonance imaging (MRI) has been used to monitor the movement of a contrast agent within the vitreous as a potential means to overcome these limitations. Three dimensional (3D) MRI has shown significant differences between the concentration of gadolinium diethylene triaminopentacetic acid (Gd-DTPA) within the vitreous when released from an episcleral

implant *in vivo* as compared to diffusion in the *ex vivo* eye.¹⁹ Empirical data were then used to calibrate a finite element mathematical model of the rabbit eye for simulation of concentration profiles.²⁰ The study was limited however in that the temporal sampling resolution required 26 minutes of imaging time to acquire a single time point and spatial resolution was limited by a slice thickness of 1.0 mm.

Recent advances in micro-computed tomography (micro-CT) provide unique advantages in pharmacokinetic studies of the eye including excellent temporal and spatial resolution.²¹ These systems have been shown to be particularly useful in providing real time data on drug delivery and distribution in a non-invasive manner.²² This combination of parameters makes micro-CT in particular a more favorable option to study ocular molecular transport over other imaging modalities that require a compromise between scan time, sensitivity and resolution.²³

The purpose of the work presented here was to create a method of measuring the concentration and transport behavior of surrogate ocular drugs following intravitreal injections. This has been accomplished by using *ex vivo* porcine eyes to study the movement of a contrast agent within the vitreous. Porcine eyes were chosen for *ex vivo* work because of their similarity in size and structure to the human eye²⁴⁻²⁷ and the ease of access to large numbers of fresh enucleated eyes. Using the acquired data sets, diffusion modeling was completed to achieve an improved understanding of the factors influencing drug flow through the vitreous.

3.2 Materials and Methods

3.2.1 Micro-CT system

Scanning was performed using a pre-clinical micro-CT imaging system (eXplore Locus Ultra, General Electric Healthcare Bioscience, London, Ontario, Canada). The system possesses the capability of combining the high resolution of micro-CT with the fast scanning speed of clinical CT. A flat-panel detector mounted on a slip-ring CT gantry was used to acquire images with an isotropic spatial resolution of 150 μm . Each 3D

volume was acquired in 8-16 seconds and provided a reconstructed 15 cm field of view with axial extent of 15 cm. X-ray acquisition parameters (80 kVp and 40-80 mA) were kept constant for each experiment.

3.2.2 Injections and Scanning

Enucleated porcine eyes were obtained from a local abattoir and used within 10 hours postmortem. During scanning and for the remainder of the study, they were maintained at 24°C (+/- 2°C). An enclosed plastic case was used for simultaneous scanning of multiple eyes while ensuring the eyes were stabilized, using 50 ml Falcon™ tube covers, and hydrated, using PBS soaked medical gauze (Figure 3.1).

A baseline volume was obtained prior to injection of contrast agent to screen for anatomical irregularity of the eyes. Intravitreal injections of diluted iohexol, a low-osmolar non-ionic iodinated contrast agent (Omnipaque 300, GE Healthcare, Oakville, Ontario, Canada) and gold nanoparticle contrast agent (AuroVist™, Nanoprobe Inc, Yaphank, New York, USA), were used as drug surrogates and tracer sources. To provide quantitative measurements and analysis using the CT number in Hounsfield units (HU) output by the system, standard solutions of known contrast agent concentrations were scanned with the eyes for calibration purposes.

The intravitreal injection technique was taught by ophthalmologists and medical residents, with a focus on mimicking a clinical injection to humans. All intravitreal injections were performed manually using 0.3 ml syringes attached to 29 gauge needles (SS05M2913, Terumo Medical Corporation, Somerset, NJ, USA). Each eye received a single 30 µl injection of a specified concentration. The needle was gently advanced through the sclera approximately 2-3 mm posterior to the superotemporal limbus and inserted to the appropriate depth of 1 cm (marked on the needle) to achieve a clinically relevant mid-vitreous injection in the porcine eye. Contrast agent was injected and the needle carefully withdrawn to minimize reflux along the *in situ* track. Immediately after injections were completed, the case was carefully positioned in the micro-CT scanner.

Experiments were performed with multiple eyes in the plastic case. Each eye received a single injection of a specified concentration. Varying concentrations were used to determine the effect of different dilutions in the transport of the drug surrogate for the duration of the experiment. In the first experiment, a volume of 30 μ l of iodine solution was used in the following concentrations: 150, 75, and 37.5 mg/ml ($n = 12$). For the pilot experiment, CT images were acquired at 12, 22, 32, 52 and 72 minutes (time 0 is at injection of the first eye). 3D scans at varying time points allowed for the measurement of the injected bolus' movement in all directions. Based on the results identified in this pilot experiment, all subsequent injections in the second experiment ($n = 18$) were carried out with a volume of 30 μ l and at iodine concentrations of 150, 37.5, 18.75, 9.38, and 4.59 mg/ml. Images were acquired at 8, 12, 24, 36, 48, 96, 144 and 192 minutes post-injection. Gold nanoparticle solutions were administered in porcine eyes ($n=6$) at concentrations of 100, 25 and 6 mg/ml. Images were acquired at 3, 5, 6, 8, 9, 11, 19, 35, 67, 131, 195, 230 minutes post-injection.

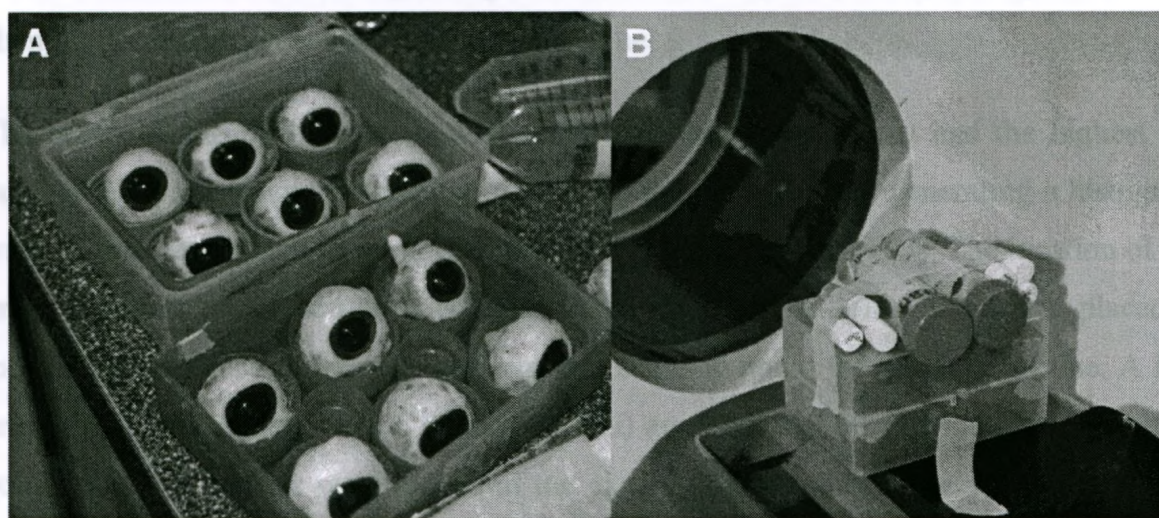


Figure 3.1 Enclosed container for *ex vivo* eyes in micro-CT scanner

An enclosed box was used to stabilize and the eyes in a closed environment for the full duration of the experiment following intravitreal injections of contrast agent. **A)** The box was designed to allow for multiple eyes to be scanned simultaneously and **B)** fit within the scanner's bore and field of view.

3.2.3 Image Analysis

CT data were analyzed with dedicated 3D visualization and analysis software (MicroView 2.1.2, General Electric Healthcare, London ON), which allowed the specimens to be viewed as multi-planar reformats or as cross-sections through the axial, sagittal and coronal planes (see Appendix A). After attainment of calibration curves to correlate CT density to contrast concentration, HU attenuation of intra-ocular voxels was converted to concentration units for further analysis.

Custom 3D regions of interest (ROIs) describing the spatial and temporal distribution of contrast agent were automatically calculated based on CT numbers (HU) using MicroView (see Appendix B). These regions were superimposed onto the image with subsequent ROIs to show varying concentrations at a single time point. Alternatively, ROIs for varying time points, but for a single concentration, were used to qualitatively show the movement of an iso-concentration over time. Lastly, both of these scenarios provide a means of measuring (ImageJ 1.41, NIH, Maryland, USA) the injected bolus' changing concentration and movement over time.

The center of the injected bolus was assumed to be the point that had the highest CT number. This was found by creating a ROI around the bolus and generating a histogram from MicroView that plots number of pixels versus CT number (HU). The location of the greatest intensity was then used as the assumed center of the bolus. A line was placed in the horizontal direction (coronal and sagittal) centered about the maximum value. A line profile plot was created with CT number (HU) against distance. For the remaining time points, the line profiles were placed in the exact same position of the scan to eliminate errors caused by any potential movement of the bolus center (see Appendix C for further information). These observed data were used to calculate the concentration profile of best fit in the diffusion model.

3.2.4 Calculation of Diffusion Coefficients

A model for diffusion from an instantaneous spherical source was chosen from Crank (1975) for the analysis of the intravitreal injection data. This model assumes that the

diffusing substance is moving uniformly through an isotropic infinite medium ($r = 0$ at $t = 0$). The concentration C_r at radial position r at time t is given by²⁸

$$C_r = \frac{1}{2} C_0 \left(\operatorname{erf} \frac{a-r}{2\sqrt{Dt}} + \operatorname{erf} \frac{a+r}{2\sqrt{Dt}} \right) - \frac{C_0}{r} \sqrt{\frac{Dt}{\pi}} \left\{ \exp\left(-\frac{(a-r)^2}{4Dt}\right) - \exp\left(-\frac{(a+r)^2}{4Dt}\right) \right\} \quad (3.1)$$

where C_0 is the initial concentration throughout a spherical bolus with an initial radius a . The analyses were based on the assumption that the injected bolus initially creates a uniformly distributed 30 μl sphere in the vitreous.

Calculation of the diffusion coefficient (D) for each time point in both the sagittal and coronal directions was made by fitting the experimental data with Equation 3.1. Analysis was completed in MATLAB (R2009b, The Mathworks Inc., Natick, MA) where custom code was used for background removal, data range selection, non-linear curve-fitting using least squares method and regression analysis (Appendix D). This approach was used to optimize the coefficient of determination (R^2) of the curve fits and provide the confidence intervals (CI) at a significance level of 95%. Diffusion coefficient values were selected for if an $R^2 \geq 0.90$ was achieved.

3.2.5 Reflective and Absorptive Boundaries

The behavior of the drug surrogate diffusion at a boundary, such as at the retina, was studied using previously derived models. Mitra et al. (1993) presented the following perturbation expansion of the non-Gaussian time dependent diffusion coefficient $D(t)$ for a finite spherical volume with a reflective (Equation 3.2) and absorptive (Equation 3.3) boundary,²⁹

$$\frac{D(t)}{D_0} = 1 - \frac{4S}{9V_p} \left(\frac{D_0 t}{\pi} \right)^{1/2} - \frac{D_0}{2a^2} t + O(t^{3/2}) \quad (3.2)$$

$$\frac{D(t)}{D_0} = 1 - \frac{2S}{9V_p} \left(\frac{D_0 t}{\pi} \right)^{1/2} - \frac{D_0}{a^2} t + O(t^{3/2}) \quad (3.3)$$

where D_0 is the diffusion constant of the bulk fluid, S/V_p is the ratio of surface area to pore volume, t is time and a is the radius.

3.3 Results

Reconstructed 3D images allowed for the visualization of contrast agent in the vitreous following a mid-vitreous injection into *ex vivo* porcine eyes (Figure 3.2). Major features of the porcine eye were also visible such as the cornea, lens and sclera. This allowed for measurements of vitreous and lens dimensions to improve accuracy of future injections. Injection concentrations of at least 6 mg/ml were sufficient to allow for visualization of the injection in the vitreous, from the background, over an extended period of time. The relationship between CT number (HU) and iodine concentration was calculated and showed a very strong linear correlation (Figure 2.2), as expected. It was established that measurable quantities of contrast agent began to reach the back of the eye (retinal surface) after 2 hours (at a concentration of 6 mg/ml).

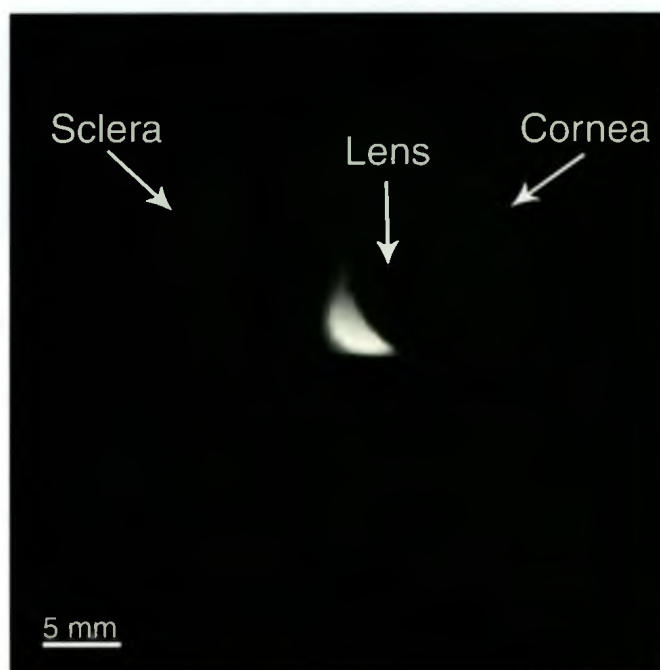


Figure 3.2 Micro-CT image of *ex vivo* porcine eye

Reconstructed 3D micro-CT image of an *ex vivo* porcine eye with intravitreal injected iodinated contrast agent (Omnipaque™) 12 minutes post-injection. Visible anatomical features are labeled (cornea, lens, sclera).

The 3D surfaces of the injected bolus (ROIs) (see Appendix B), that were created to represent the bolus, provided visualization of contrast concentrations at each time point. For each eye specimen, several ROIs were superimposed to qualitatively show varying concentrations at a single time point (Figure 3.3a). This provided an excellent means of

viewing how the concentration of contrast was distributed within the bolus and the effects of time. Alternatively, ROIs for varying time points and for a single concentration were used to qualitatively show the movement of a single concentration over time (Figure 3.3b). Both of these scenarios provided a means of viewing the injected bolus' changing concentration and movement over time.

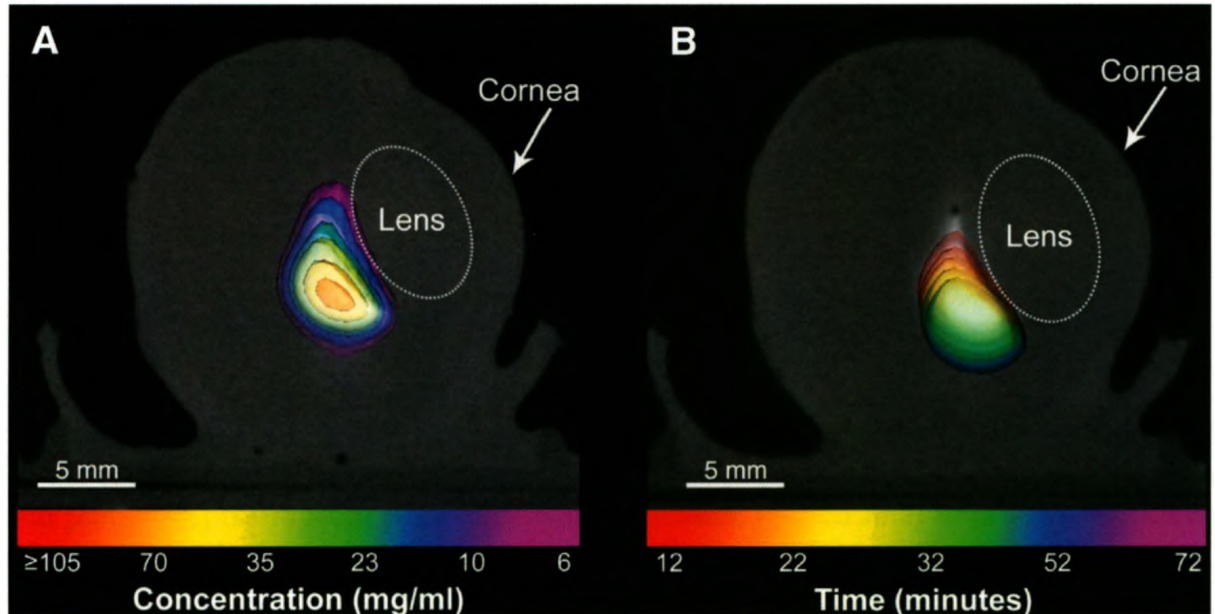


Figure 3.3 Isoshells representing concentrations in sagittal slice of micro-CT scan

A) 2D sagittal micro-CT image of *ex vivo* porcine eye following 30 μ l intravitreal injection of iodinated contrast agent (Omnipaque™) with 3D regions of interest representing specific concentrations from 6 to 105 mg/ml at 12 minutes post-injection. **B)** 2D sagittal micro-CT image of *ex vivo* porcine eye following 30 μ l intravitreal injection of iodinated contrast agent (Omnipaque™) with 3D regions of interest representing concentration shells of 10 mg/ml over a time period of 12-72 minutes.

Direct comparisons of the observed data and the predicted (Equation 3.1) have been made for each specimen at all time points in which it was scanned. Figure 3.4 shows a typical signal profile for the experimental and predicted data after 32 minutes, with the 95% CI around the fit. The R^2 for this case was 0.991 and the confidence intervals are 91.503 HU, which represents less than 0.6% of the maximum CT number (HU). In general, the experimental data followed a Gaussian distribution curve and the time evolution of the mass density functions is consistent with a diffusive transport process.

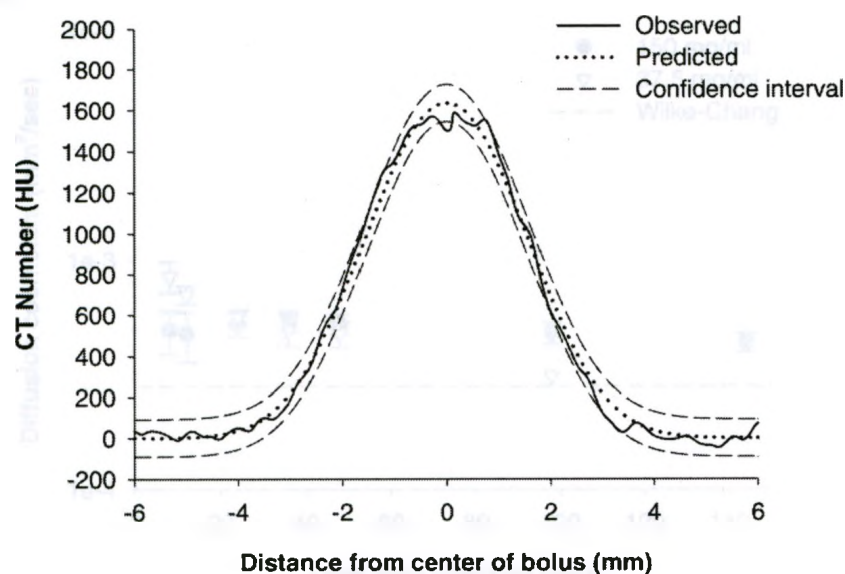


Figure 3.4 Observed and predicted signal profile through bolus

2D signal profile at 32 minute time point displaying observed profile from micro-CT image line profile (solid line) that was obtained through the center of the injected bolus and predicted profile from passive diffusion equation (dotted line) with 95% confidence interval limits shown (dashed lines).

Diffusion coefficients were found from the optimal curve fits of the signal profiles. The combined results for iodinated contrast agent tests are shown in Figure 3.5 for the 150 and 37.5 mg/ml initial iodine concentration, where the diffusion coefficients for the horizontal (Figure 3.5a) and vertical directions (Figure 3.5b) are plotted against time. The diffusion coefficients have a mean of $4.76 \times 10^{-4} \text{ mm}^2/\text{sec}$ and standard deviation of $7.79 \times 10^{-5} \text{ mm}^2/\text{s}$ for 150 mg/ml iodine concentration and $6.10 \times 10^{-4} \pm 1.61 \times 10^{-4} \text{ mm}^2/\text{s}$ for 37.5 mg/ml concentration. The R^2 values have a mean of 0.940 and a mean CI of $\pm 1.69\%$ of the maximum CT number. The diffusion coefficient values lie slightly above the Wilke-Chang estimation ($2.8 \times 10^{-4} \text{ mm}^2/\text{s}$). It should also be noted that they appear to reduce with time and there are fewer values that meet the $R^2 \geq 0.90$ criteria at later time points.

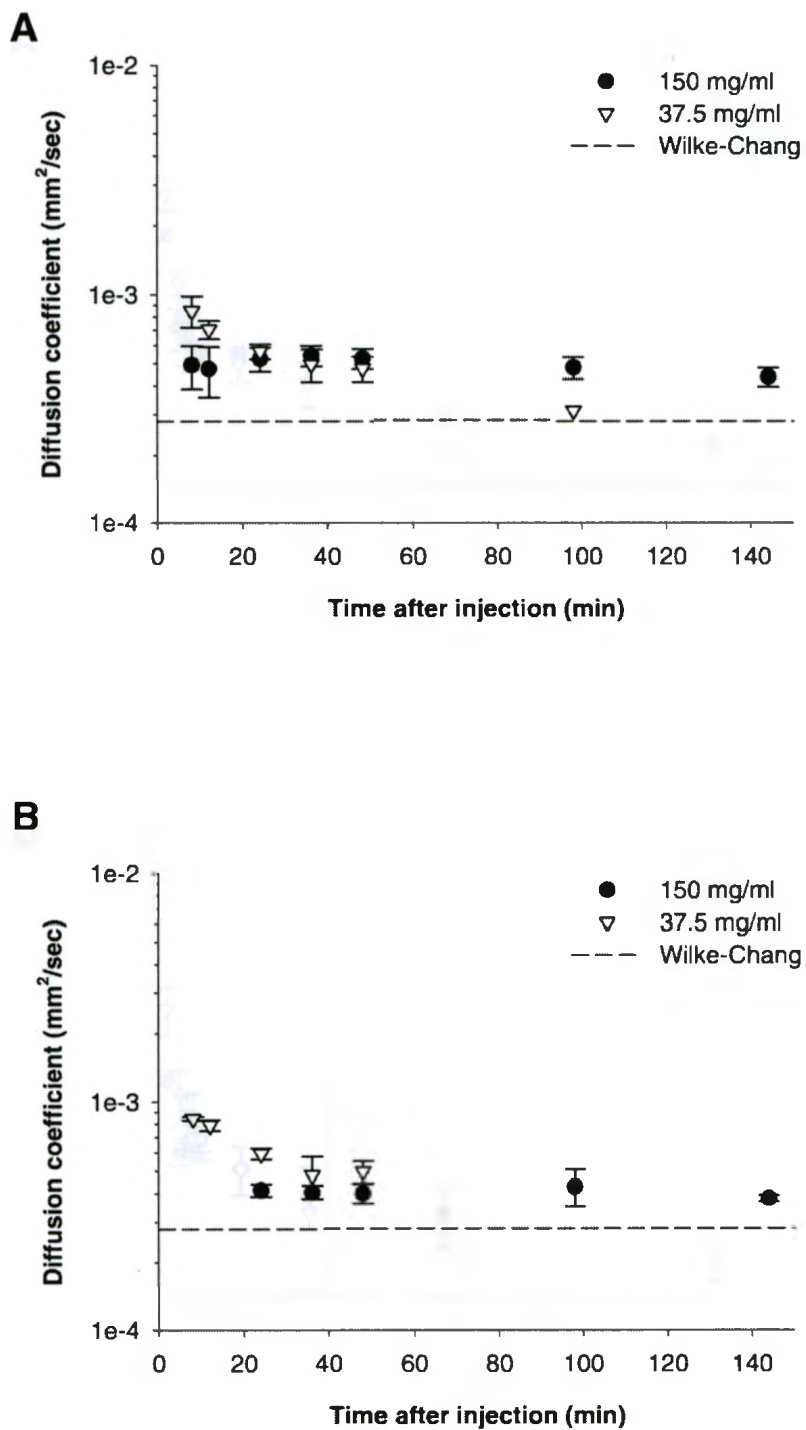


Figure 3.5 Iodine solution diffusion coefficients

Plot of calculated diffusion coefficients in the **A**) horizontal direction and **B**) vertical direction of iodine at 150 (closed circle) and 37.5 mg/ml (open triangle) concentration in vitreous against time in which micro-CT scans were acquired. Values are compared against the Wilke-Chang estimation (dashed line).

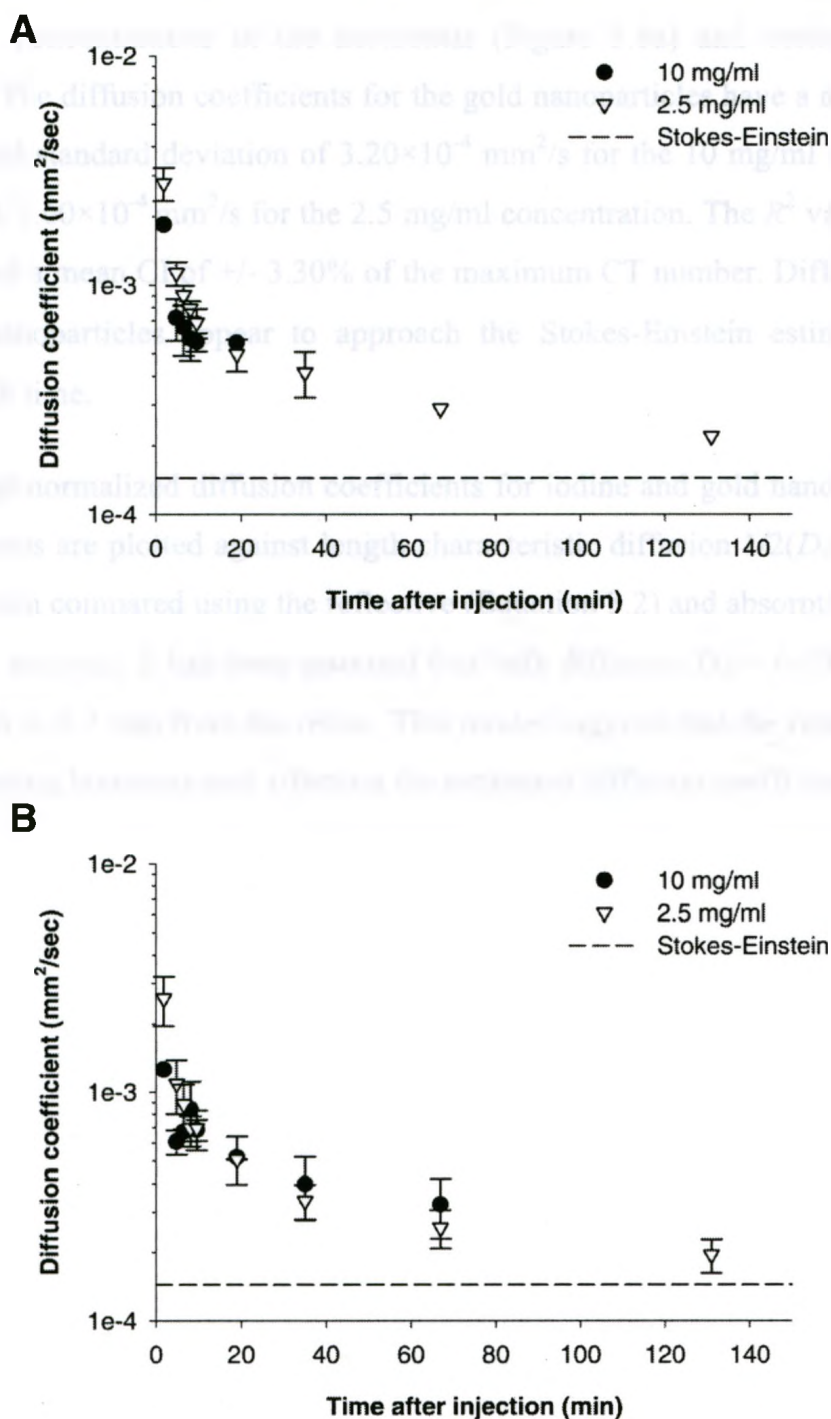


Figure 3.6 Gold nanoparticle diffusion coefficients

Plot of calculated diffusion coefficients in the **A**) horizontal direction and **B**) vertical direction of gold nanoparticles at 10 (closed circle) and 2.5 mg/ml (open triangle) concentration in vitreous against time in which micro-CT scans were acquired. Values are compared against the Stokes-Einstein estimation (dashed line).

Diffusivity values of gold nanoparticles in the vitreous are shown in Figure 3.6 for 10 and 2.5 mg/ml concentrations in the horizontal (Figure 3.6a) and vertical (Figure 3.6b) directions. The diffusion coefficients for the gold nanoparticles have a mean of $6.72 \times 10^{-4} \text{ mm}^2/\text{sec}$ and standard deviation of $3.20 \times 10^{-4} \text{ mm}^2/\text{s}$ for the 10 mg/ml concentration and $9.07 \times 10^{-4} \pm 7.60 \times 10^{-4} \text{ mm}^2/\text{s}$ for the 2.5 mg/ml concentration. The R^2 values have a mean of 0.940 and a mean CI of $\pm 3.30\%$ of the maximum CT number. Diffusion coefficients for gold nanoparticles appear to approach the Stokes-Einstein estimation ($1.44 \times 10^{-4} \text{ mm}^2/\text{s}$) with time.

The average normalized diffusion coefficients for iodine and gold nanoparticles solution in the vitreous are plotted against length characteristic diffusion $1/2(D_0 t)^{1/2}$ in Figure 3.7 and have been compared using the reflective (Equation 3.2) and absorptive (Equation 3.3) boundaries analysis. It has been assumed that bulk diffusion $D_0 = 6 \times 10^{-4} \text{ mm}^2/\text{s}$ and the bolus center is 4-7 mm from the retina. This model suggests that the retinal zone is acting like a reflecting boundary and affecting the estimated diffusion coefficient.



Figure 3.7 Reflective and absorptive diffusion. A scatter plot showing the relationship between normalized diffusion coefficients and the length characteristic diffusion $1/2(D_0 t)^{1/2}$ for gold nanoparticles in the vitreous. The Reflective series (open circles) and Absorptive series (open squares) are plotted. The Reflective series starts at approximately (0.1, 0.9) and ends at (1.1, 0.4). The Absorptive series starts at approximately (0.1, 0.8) and ends at (1.1, 0.3).

3.4 Discussion

The experimental framework in this study has enabled real-time tracking of drug surrogate movement, delivered as a drug surrogate, following intravitreal injection, through the vitreous to the injected retinal site. The framework permits not only visualization of the total distribution of the drug surrogate over an extended period of time, but also quantitative evaluation of the drug surrogate's movement.

3.4.1 Capabilities of Micro-CT in Ocular Drug Transport Study

Previous studies attempted visualization of the distribution of drug surrogate in the vitreous following intravitreal injection in vivo, but failed to provide coupled spatial and temporal information.³⁰ The less spatial resolution was achieved, as presented by

using a pre-clinical micro-CT scanner (Figure 3.3a). With CT, it was possible to visualize the distribution of drug surrogate in the vitreous over a period of time (Figure 3.3b) and to quantify the drug surrogate's movement (Figure 3.3c).

At 120 μ m resolution, the micro-CT system also provides the secondary field of view, which is required to model transport as a diffusion process. The same system can be modified almost continuously with scan speed, field of view, and resolution over a number of hours. The approach allowed for the visualization of drug surrogate distribution (Figure 3.3a) and movement (Figure 3.3b) over a period of time.

Various methods have been used to visualize drug surrogate distribution and movement over time. This is compared to the discontinuous data sets obtained by microscopy in many time points, such as in slit-lamp photography, fundus photography, and retinal imaging. Through the use of overlay or image processing, such as Figure 3.3, it was found that the representation of the drug surrogate distribution and movement closely followed the shape of the lens when the drug surrogate was injected into the vitreous. This study provided the first visualization of drug surrogate distribution and movement in the vitreous.

This is compared to the discontinuous data sets obtained by microscopy in many time points, such as in slit-lamp photography, fundus photography, and retinal imaging. Through the use of overlay or image processing, such as Figure 3.3, it was found that the representation of the drug surrogate distribution and movement closely followed the shape of the lens when the drug surrogate was injected into the vitreous. This study provided the first visualization of drug surrogate distribution and movement in the vitreous.

Figure 3.7 shows the average normalized diffusion coefficients plotted against length characteristic diffusion for experimental values of A) iodine (150 mg/ml) and B) gold nanoparticles (10 mg/ml) in the vitreous in the horizontal direction, sagittal (closed circles) and coronal (open circles), compared against numerical simulations of reflective (solid curve) and absorbing (dashed curve) for a spherical pore.

Figure 3.7 Reflective and absorbing diffusion

Average normalized diffusion coefficients plotted against length characteristic diffusion for experimental values of A) iodine (150 mg/ml) and B) gold nanoparticles (10 mg/ml) in the vitreous in the horizontal direction, sagittal (closed circles) and coronal (open circles), compared against numerical simulations of reflective (solid curve) and absorbing (dashed curve) for a spherical pore.

3.4 Discussion

The framework developed in this study has enabled real-time tracking of a contrast agent bolus, delivered as a drug mimic via intravitreal injection, through the vitreous to the desired retinal fate. The framework permits not only visualization of the bolus in the same specimen over an extended period of time, but also quantitative evaluation of the bolus evolution.

3.4.1 Capabilities of Micro-CT in Ocular Drug Transport Study

Recent studies attempted determination of the distribution of drug surrogates in the eye following intravitreal injection *in vivo*, but failed to provide coupled spatial and temporal information.³⁰ The necessary spatial resolution was achieved in the work presented by using a pre-clinical micro-CT scanner, rather than MRI.^{23,30} With CT, it was possible to estimate concentrations of contrast agents to within ± 0.027 mg/ml over a range of 6 to 300 mg/ml for iodine and 3 to 150 mg/ml for gold nanoparticles with a spatial resolution of 150 μm . The pre-clinical micro-CT scanner also provides the necessary fast scanning speed to achieve the temporal resolution required to model transport and flow within the eye. The same specimen can be monitored almost continuously with scans acquired every 90 seconds over a number of hours. This approach allowed for the visualization of drug surrogate concentration (Figure 3.3a) and movement (Figure 3.3b). Both of these scenarios provided a means of viewing the injected bolus' changing concentration and movement over time. This is compared to the discontinuous data set achieved by sacrificing many specimens at different time points, such as in snap freezing,¹⁸ which lacks consistency and reproducibility. Through the use of overlay in post-imaging processing, such as Figure 3.3, it was found there is preferential flow in the vertical direction and the drug surrogate closely followed the shape of the lens when the injection site was near the lens. This study provides the proof-of-concept data that micro-CT systems available today provide the high resolution, short scan times and near continuous scan time points to accurately track contrast in the vitreous from delivery to target tissue fate.

3.4.2 Modeling Ocular Drug Transport Using Experimental Data

The real-time empirical data acquired from the micro-CT scans of the injected intravitreal bolus have enabled comparison with a 'benchmark' bulk diffusion model to aid the interpretation of the results. Diffusion is thought to be the predominant transport mechanism for ocular drugs through the vitreous humor and we have been able to determine the apparent diffusion coefficients of iodine and gold nanoparticle solutions in the vitreous of the eye. Micro-CT allows for simple measuring of the signal profiles in any direction with a high resolution and sensitivity. These profiles can be used to fit a mathematical model (Figure 3.4) and provide a means of calculating to what degree diffusion is responsible in drug surrogate flow.

Average diffusion coefficients calculated for the iodine and gold nanoparticles did not correlate with the expectation that they would be inversely proportional to the molecular weight. The diffusion coefficient in the vitreous, when compared to an aqueous solution, has been shown differ from the assumption of being inversely proportional to the molecular weight.³¹ Both iodine and gold nanoparticles demonstrated time dependent effects and at later time points approached the diffusion coefficients from Wilke-Chang and Stokes-Einstein estimations, respectively. Density drive gravity flow in the vertical direction could also be a contributing factor with higher concentration solutions. The asymmetry and translation of the signal profiles (see Appendix C) and the reduction in the magnitude of the apparent diffusion coefficients with time (as the overall bolus concentration and specific gravity reduces with diffusion) support this hypothesis.

It can also be suggested that diffusion within a finite volume is affecting the behavior. Diffusion coefficients that reduce with time could be a result of the drug surrogate reaching a reflecting boundary, the retina. A number of researchers have investigated diffusive phenomena in finite volumes, adjacent to absorptive and reflective boundaries.³²⁻³⁴ The comparisons in Figure 3.7 show a reasonable match, thus this appears to be a plausible hypothesis and is further supported by reductions in the R^2 values for the fits with the Gaussian model (Equation 3.1) at later time points.

3.4.3 Limitations

A limitation of the current study is the use of contrast agents as drug mimics for ocular drugs. Omnipaque was chosen as the contrast agent in these experiments due to its common use with micro-CT applications and well-defined properties, reliability and cost effectiveness. Gold nanoparticles have a closer molecular weight to common intravitreal drugs and has been shown to be a suitable source of contrast and a tracer to allow proof-of-principle tests to be realized. Modifying ocular drugs (bevacizumab or ranibizumab) for detection in future micro-CT scanning is essential to provide clinically relevant information on drug transport mechanisms. In particular, stability, density, molecular weight and ionic charge of compounds can have significant effects on the observed behavior. A competing set of criteria for using the micro-CT technique requires radiopaque drug surrogates at suitable concentrations for visualization, but these must also be balanced by clinically relevant volumes and concentrations.

The likely significance for *in vivo* studies has yet to be determined, since both diffusive and advective flow will be occurring.^{9,35} This *ex vivo* study elucidates diffusion effects and can be deconvolved from future *in vivo* work to correctly understand the role of advection. Further work will also involve the development of more sophisticated computational fluid dynamics approaches to provide further understanding of the time dependent coupled diffusion and advection transport behavior in a finite volume.

3.5 Conclusions

Mid-vitreous injection of iodinated and gold nanoparticle contrast agents as a drug mimic using *ex vivo* porcine eyes and micro-CT scanning provides an accurate high resolution, non-invasive method of spatial and temporal tracking of the bolus and concentrations. The ability to extrapolate pharmacokinetic profiles from any region of the vitreous at various time points provides extensive information in understanding ocular drug flow. Our data show the effects of diffusion and boundary reflection on the movement of the solutions in the vitreous body. Knowledge that a drug compound is reaching the retina at a specific concentration and at a particular time after injection is vital information that

has not been visualized to date. The results shown have provided the required *ex vivo* proxy to apply the framework to *in vivo* experiments in rabbits. This work has provided the initial steps towards a better understanding of the mechanisms of drug transport when administered through the vitreous using micro-CT scanning.

3.6 References

1. Liang, F. Q.; Viola, R. S.; del Cerro, M.; Aquavella, J. V. Noncross-linked collagen discs and cross-linked collagen shields in the delivery of gentamicin to rabbits eyes. *Invest Ophthalmol Vis Sci* 33(7):2194-2198; 1992.
2. Pflugfelder, S. C.; Hernandez, E.; Fliesler, S. J.; Alvarez, J.; Pflugfelder, M. E.; Forster, R. K. Intravitreal vancomycin. Retinal toxicity, clearance, and interaction with gentamicin. *Arch Ophthalmol* 105(6):831-837; 1987.
3. Stay, M. S.; Xu, J.; Randolph, T. W.; Barocas, V. H. Computer simulation of convective and diffusive transport of controlled-release drugs in the vitreous humor. *Pharm Res* 20(1):96-102; 2003.
4. Lee, V. H. L.; Pince, K. J.; Frambach, D. A. Drug delivery to the posterior segment. In: Ogden, T. E.; Schachar, A. P., eds. *Retina*. St. Louis: Mosby; 1989:483-498.
5. Peyman, G. A.; Schulman, J. A. Intravitreal drug therapy. *Jpn J Ophthalmol* 33(4):392-404; 1989.
6. Cochereau-Massin, I.; Lehoang, P.; Lautier-Frau, M.; Zazoun, L.; Marcel, P.; Robinet, M.; Matheron, S.; Katlama, C.; Gharakhanian, S.; Rozenbaum, W. and others. Efficacy and tolerance of intravitreal ganciclovir in cytomegalovirus retinitis in acquired immune deficiency syndrome. *Ophthalmology* 98(9):1348-1353; 1991.
7. Regillo, C. D.; Brown, D. M.; Abraham, P.; Yue, H.; Ianchulev, T.; Schneider, S.; Shams, N. Randomized, double-masked, sham-controlled trial of ranibizumab for neovascular age-related macular degeneration: PIER Study year 1. *Am J Ophthalmol* 145(2):239-248; 2008.
8. Ghate, D.; Edelhauser, H. F. Ocular drug delivery. *Expert Opin Drug Deliv* 3(2):275-287; 2006.
9. Kathawate, J.; Acharya, S. Computational modeling of intravitreal drug delivery in the vitreous chamber with different vitreous substitutes. *Int J Heat Mass Tran* 51(23-24):5598-5609; 2008.
10. Li, S. K.; Lizak, M. J.; Jeong, E. K. MRI in ocular drug delivery. *NMR Biomed* 21(9):941-956; 2008.
11. Araie, M.; Maurice, D. M. The loss of fluorescein, fluorescein glucuronide and fluorescein isothiocyanate dextran from the vitreous by the anterior and retinal pathways. *Exp Eye Res* 52(1):27-39; 1991.
12. Ohtori, A.; Tojo, K. In vivo/in vitro correlation of intravitreal delivery of drugs with the help of computer simulation. *Biol Pharm Bull* 17(2):283-290; 1994.

13. Friedrich, S.; Cheng, Y. L.; Saville, B. Finite element modeling of drug distribution in the vitreous humor of the rabbit eye. *Ann Biomed Eng* 25(2):303-314; 1997.
14. Avtar, R.; Tandon, D. A mathematical analysis of intravitreal drug transport. *Trop J Pharm Res* 7(1):867-877; 2008.
15. Friedrich, S.; Cheng, Y. L.; Saville, B. Drug distribution in the vitreous humor of the human eye: the effects of intravitreal injection position and volume. *Curr Eye Res* 16(7):663-669; 1997.
16. Bakri, S. J.; Snyder, M. R.; Reid, J. M.; Pulido, J. S.; Singh, R. J. Pharmacokinetics of intravitreal bevacizumab (Avastin). *Ophthalmology* 114(5):855-859; 2007.
17. Bakri, S. J.; Snyder, M. R.; Reid, J. M.; Pulido, J. S.; Ezzat, M. K.; Singh, R. J. Pharmacokinetics of intravitreal ranibizumab (Lucentis). *Ophthalmology* 114(12):2179-2182; 2007.
18. Berglin, L. C.; Bergman, L.; Berezovsky, D.; Kim, E.; Myles, B.; Anderson, C.; Grossniklaus, H.; Edelhauser, H. Tracing of intravitreally injected labeled drugs and nanoparticles in human vitreous and retina using a liquid nitrogen snap-freeze thaw technique. *Invest Ophthalmol Vis Sci* 50(5):3487; 2009.
19. Kim, H.; Robinson, M. R.; Lizak, M. J.; Tansey, G.; Lutz, R. J.; Yuan, P.; Wang, N. S.; Csaky, K. G. Controlled drug release from an ocular implant: an evaluation using dynamic three-dimensional magnetic resonance imaging. *Invest Ophthalmol Vis Sci* 45(8):2722-2731; 2004.
20. Kim, H.; Lizak, M. J.; Tansey, G.; Csaky, K. G.; Robinson, M. R.; Yuan, P.; Wang, N. S.; Lutz, R. J. Study of ocular transport of drugs released from an intravitreal implant using magnetic resonance imaging. *Ann Biomed Eng* 33(2):150-164; 2005.
21. Du, L. Y.; Umoh, J.; Nikolov, H. N.; Pollmann, S. I.; Lee, T. Y.; Holdsworth, D. W. A quality assurance phantom for the performance evaluation of volumetric micro-CT systems. *Phys Med Biol* 52(23):7087-7108; 2007.
22. Szymanski-Exner, A.; Stowe, N. T.; Salem, K.; Lazebnik, R.; Haaga, J. R.; Wilson, D. L.; Gao, J. Noninvasive monitoring of local drug release using X-ray computed tomography: optimization and in vitro/in vivo validation. *J Pharm Sci* 92(2):289-296; 2003.
23. Li, S. K.; Jeong, E. K.; Hastings, M. S. Magnetic resonance imaging study of current and ion delivery into the eye during transscleral and transcorneal iontophoresis. *Invest Ophthalmol Vis Sci* 45(4):1224-1231; 2004.

24. Lee, B.; Litt, M.; Buchsbaum, G. Rheology of the vitreous body. Part 2: Viscoelasticity of bovine and porcine vitreous. *Biorheology* 31(4):327-338; 1994.
25. Noulas, A. V.; Theocharis, A. D.; Feretis, E.; Papageorgakopoulou, N.; Karamanos, N. K.; Theocharis, D. A. Pig vitreous gel: macromolecular composition with particular reference to hyaluronan-binding proteoglycans. *Biochimie* 84(4):295-302; 2002.
26. Theocharis, Achilleas D.; Papageorgakopoulou, N.; Feretis, E.; Theocharis, Dimitrios A. Occurrence and structural characterization of versican-like proteoglycan in human vitreous. *Biochimie* 84(12):1235-1241; 2002.
27. Ruiz-Ederra, J.; García, M.; Hernández, M.; Urcola, H.; Hernández-Barbáchano, E.; Araiz, J.; Vecino, E. The pig eye as a novel model of glaucoma. *Exp Eye Res* 81(5):561-569; 2005.
28. Crank, J. The mathematics of diffusion, 2d ed. USA: Oxford University Press; 1975.
29. Mitra, P. P.; Sen, P. N.; Schwartz, L. M. Short-time behavior of the diffusion coefficient as a geometrical probe of porous media. *Physical Review B* 47(14):8565; 1993.
30. Molokhia, S. A.; Jeong, E. K.; Higuchi, W. I.; Li, S. K. Transscleral iontophoretic and intravitreal delivery of a macromolecule: study of ocular distribution in vivo and postmortem with MRI. *Exp Eye Res* 88(3):418-425; 2009.
31. Tojo, K. J.; Ohtori, A. Pharmacokinetic model of intravitreal drug injection. *Math Biosci* 123(1):59-75; 1994.
32. Sen, P. N. Time-dependent diffusion coefficient as a probe of geometry. *Concepts in Magnetic Resonance Part A* 23A(1):1-21; 2004.
33. Frøhlich, A. F.; Jespersen, S. N.; Østergaard, L.; Kiselev, V. G. The effect of impermeable boundaries of arbitrary geometry on the apparent diffusion coefficient. *Journal of Magnetic Resonance* 194(1):128-135; 2008.
34. Ghadirian, B.; Stait-Gardner, T.; Castillo, R.; Price, W. S. Modeling diffusion in restricted systems using the heat kernel expansion. *The Journal of Chemical Physics* 132(23):4108-4110; 2010.
35. Xu, J.; Heys, J. J.; Barocas, V. H.; Randolph, T. W. Permeability and diffusion in vitreous humor: implications for drug delivery. *Pharm Res* 17(6):664-669; 2000.

Chapter 4

4 Identification of anomalous features of intravitreal injections using micro-computed tomography

This chapter describes the identified anomalous features that impact drug delivery in the eye as a result of an intravitreal injection. Three-dimensional micro-computed tomography images were used to detect characteristics not normally identified or studied following an intravitreal injection. The presence of air bubbles and inconsistent bolus shapes have indicated that intravitreal injections have high variability. It is only through the realization of these anomalous features that the efficacy of intravitreal drug delivery will be improved through a consistent and accurate injection technique.

4.1 Introduction

Intravitreal injections remain a common technique for administering ocular drugs to the posterior segment of the eye, especially for treatment of age-related macular degeneration. Aspects of intravitreal injections, such as drug reflux, leakage from the needle tract and needle depth, are known to be of importance for the efficacy of intravitreal drug delivery.¹ Although, several types of symptomatic complications have been shown to occur as a result of these injections.²⁻⁴ With improved efficacy through injection technique, it is expected there would be a reduction in the number of complications associated with intravitreal injections.

Some complications that are less studied are the introduction of air or silicone into the eye. Air bubbles have been previously documented and are seen clinically following intravitreal injections,⁵ but there has been little reporting on the size and fate of these air bubbles. Other clinical reports have found intravitreal silicone oil droplets present within the eye following intravitreal drug injections.^{6,7} These are believed to have originated

from the needle as a result of the manufacturing or repackaging processes.⁸ Any factors that may affect the therapeutic efficacy of the drug being administered by intravitreal injection, such as the introduction of bubbles in the vitreous, should be addressed.

Pharmacokinetics in the vitreous is influenced by a number of factors. The more well-known and understood include molecular size of the drug,^{9,10} vitreous liquefaction,¹¹ vitreous volume,¹² intraocular pressure¹³ and intraocular inflammation.¹⁴ Some factors, such as vitreous liquefaction or volume, cannot be changed through treatment options. The differing properties of the vitreous as a result of vitreous heterogeneity^{15,16} can significantly alter how a drug travels through the vitreous in terms of time and route. The distribution of drug in a liquefied vitreous has been shown to be faster than that of a normal vitreous¹⁷ and the effect on drug kinetics is largely influenced by the location of liquefaction.¹⁸

Many pharmacokinetic modeling studies, and therefore drug dosages, are administered based on assumptions of a specific bolus shape^{19,20} and location of injection,²¹ but deviations from these assumptions and predications change the flow and dosage window of the drug. Therefore, the most efficient and effective outcomes for the target tissues may not be realized. The purpose of the work presented in this chapter is to identify and address anomalous features found following intravitreal injections using a porcine and rabbit eye model. With direct spatial and temporal visualization of drug boli from intravitreal injections using micro-computed tomography, we are better able to understand the impact of anomalous features on drug delivery in the eye.

4.2 Methods

4.2.1 Micro-Computed Tomography

Micro-computed tomography (micro-CT) scanning was performed using a pre-clinical system (eXplore Locus Ultra, General Electric Healthcare Bioscience, London, Ontario, Canada). A flat-panel detector mounted on a slip-ring CT gantry was used to acquire images with an isotropic spatial resolution of 150 μm . Each 3D volume was acquired in

8-16 seconds and x-ray acquisition parameters (80 kVp and 40-80 mA) were kept constant for each experiment.

4.2.2 Intravitreal Injections

Freshly harvested enucleated porcine eyes were obtained from a local abattoir and used within 10 hours postmortem. During scanning and for the remainder of the study, they were maintained at 24°C (+/- 2°C). Pre-injection scans confirmed no abnormalities in any eyes. Iodinated (Omnipaque™ 300, GE Healthcare, Oakville, Ontario, Canada) and gold nanoparticle (AuroVist™, Nanoprobe Inc, Yaphank, New York, USA) contrast agents were used as drug mimics at varying concentrations. Clinically relevant intravitreal injections of a 30 µl volume of contrast agent were administered into 24 enucleated eyes. Injections were performed 2-3 mm posterior to the superotemporal limbus at a depth of 1 cm using 29-gauge needles (SS05M2913, Terumo Medical Corporation, Somerset, NJ, USA). Each injection lasted for approximately 2 to 4 seconds.

An additional experiment was performed using *ex vivo* rabbit eyes to investigate the effects of flow rate on intravitreal injections. Three groups of varying flow rates were used and labeled as fast, intermediate and slow injections. Each set utilized three rabbit eyes, one receiving an injection via a syringe pump (Harvard Apparatus PHD 4400 Hpsi, Harvard Apparatus, Massachusetts, USA) and two receiving hand injections designed to mimic a clinical injection. The syringe pump allows for a very accurate volume and flow rate administration and provides the capability to exaggerate flow rates: fast (72 ml/hr), intermediate (0.6 ml/hr) and slow injection (0.144 ml/hr).

4.2.3 Imaging

Scans of the porcine eyes were acquired up to 230 minutes (the anticipated time for the contrast agent to remain at sufficient concentration and/or reach the retina) following the injection to allow for visualization of the contrast agent's progression through the vitreous. Grey scale image intensity variations can be used to differentiate between tissues in the eye and introduced fluids and gases. If used as a drug mimic, the temporal and spatial changes in contrast agent concentration can also be observed as the fluid diffuses through the vitreous.

Experiments performed to investigate the flow rate of intravitreal injections were scanned for up to approximately 20 minutes post-injection. Whole volume scans were acquired as rapidly as possible. To allow for time for scanner start-up and data transmission, scans could be acquired at a maximum rate of every 2-3 minutes.

4.2.4 Image Analysis

The acquired scans were reconstructed and analyzed using dedicated 3D computed tomography visualization and analysis software (MicroView 2.1.2, GE Healthcare, London, Ontario, Canada). Upon examination of the reconstructed scans, anomalous features of air bubbles and irregular bolus shapes were realized.

To better understand the behavior of the air bubbles over time, measures of diameter were taken using signal profiles and 3D regions of interest. The location of each air bubbles was also recorded by its center x , y and z coordinates. All air bubbles resembled perfect spheres and the volume was calculated using the sphere volume equation with the measured diameter. Plots of bubble volume (V) with time (t) were produced and assuming first order kinetics, the slope of these lines were found, providing the decay constant (k), of the following exponential decay equation:

$$V = V_0 \cdot e^{-kt} \quad (4.1)$$

where V_0 is the assumed initial volume of the bubble.

Analysis of the initial bolus shapes was completed by measuring the length, height and width of a reference rectangular prism into which each bolus fit. It should be noted that due to the irregularity of the shapes, these measures only provide an approximation of the shape of the boli. Surface area of the initial bolus was calculated by creating a 30 μ l isosurface around the injected contrast agent. From this the surface area was automatically calculated using an automated feature within the software.

4.3 Results

4.3.1 Air Bubbles

Despite using typical clinical procedures to eliminate air from entering the vitreous during hand injection (e.g. vertical positioning of needle, while tapping the syringe and pushing out air), air bubbles were clearly visible within the vitreous (Figure 4.1) of 21 eyes following the injections and totaled 36 air bubbles.

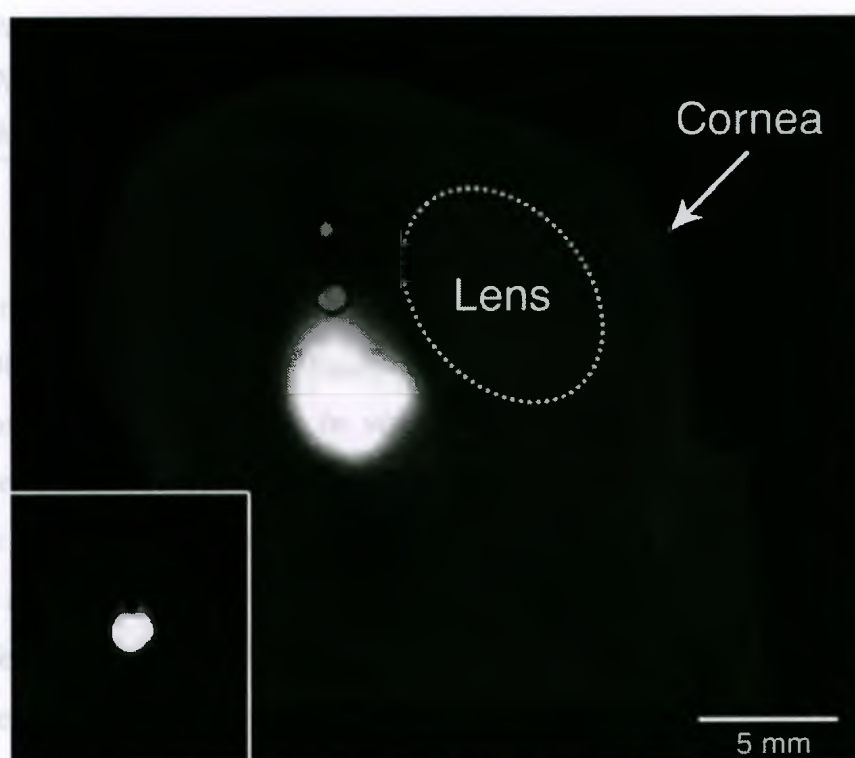


Figure 4.1 Air bubbles seen in micro-CT scan

Micro-computed tomography image showing air bubbles outlined as grey isosurfaces found within the vitreous following intravitreal injection. Inset image is a 2D slice through the injected contrast agent (white region) with the presence of an air bubble (black circle).

The initial volume of the air bubbles ranged from 0.01 μl to 1.50 μl in volume and the mean was 0.03 μl . Some movement (~ 1 mm in any direction) of the bubbles occurred

over the scanning period of 230 minutes. The size of the bubbles was found to decrease over this visualization period (Table 4.1).

Table 4.1 Air bubble changes over time in the vitreous

Air bubble characteristics and the changes over the period of 120 minutes post-injection.

Variable	5 minutes post-injection	135 minutes post-injection
No. per eye (mean)	1.78	1.38
Volume (μl)		
Mean \pm SD	0.06 ± 0.09	0.04 ± 0.07
Minimum	0.010	0.001
Maximum	1.483	1.421

Using the first order kinetics assumption, the decay constants of these bubbles (k) had a mean of $0.0067 \pm 0.0022 \text{ min}^{-1}$. Hence the bubbles had half-lives of 0.09 ± 0.02 days, which is somewhat shorter than *in vivo* observations of free non-expansile gaseous bubbles have found previously.²² This may be due to the size of the air bubbles; previous studies have used large bubbles relative to the eye volume and the relationship between surface area and volume is quite different for smaller bubbles. Further investigation of the relative differences in half-life between different sized bubbles is shown in Figure 4.2, where the decay in bubble volume with time is shown for four typical bubbles with sizes ranging from 0.01 to 0.57 μl are shown. Each decay sequence has been fitted with Equation 4.1 to find the half-life, which is seen to reduce with bubble size.

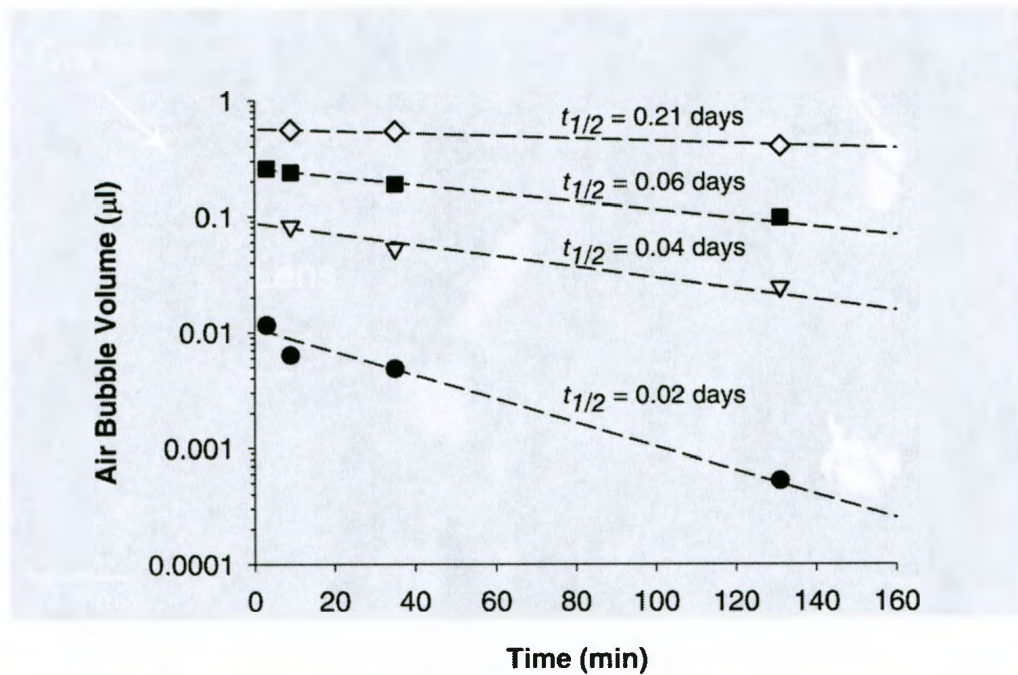


Figure 4.2 Influence of time on air bubble volume

The relationship between air bubble volume (logarithmic scale) and time that was observed in the micro-CT images following intravitreal injections. Lines indicate calculated decay using Equation 4.1.

4.3.2 Bolus Shape

Many of the injected boli were found to have abnormal initial shapes (Figure 4.3). The assumed shape of a sphere was rarely found; rather characteristics such as two conjoining spheres or tear drop shapes often resulted. For an assumed sphere, the diameter would be approximately 3.86 mm (based on 30 μ l volume). However, the extent of the initial boli had a larger range and a higher than expected average (Table 4.2). These asymmetric boli were attributed to movement of the needle tip during the injection and reflux of the drug mimic up the needle path. There was also no true center of the boli (i.e. no single region with a peak contrast concentration) when the initial shape was abnormal.

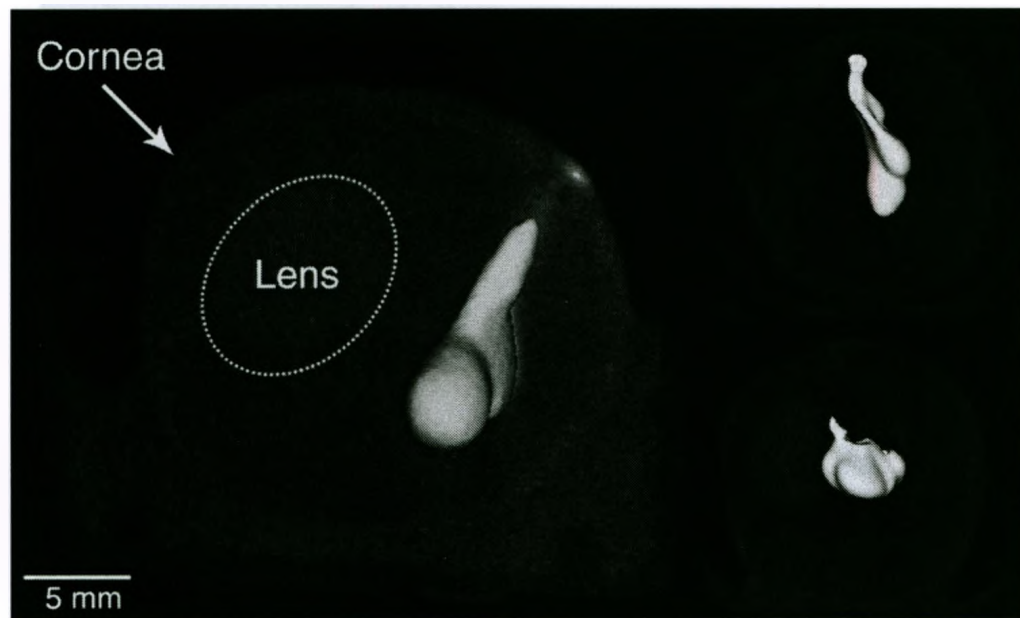


Figure 4.3 Bolus shapes shown in micro-CT images

Micro-computed tomography images showing the abnormal shapes as a result of needle movement during the intravitreal injection with the grey isosurface outlining the injected contrast agent in three different specimens.

Table 4.2 Injected bolus dimensions

30 μ l bolus shape dimensions in first scan after injection (5 minutes)

Variable	Length (mm)	Height (mm)	Width (mm)
Mean \pm SD	4.57 \pm 1.01	5.67 \pm 1.33	4.73 \pm 2.12
Minimum	2.85	3.81	2.98
Maximum	6.39	8.49	4.92

4.3.3 Injection Flow Rate

The slow flow rate injection of 0.144 ml/hr, or for the duration of 12.5 minutes, provided visualization of how the injected solution disperses into the vitreous to form an initial bolus (Figure 4.4). Rather than forming a sphere at the very tip of the needle, the injected solution forms up around the needle and disperses in a pattern to look like it is being pushed away from the needle.

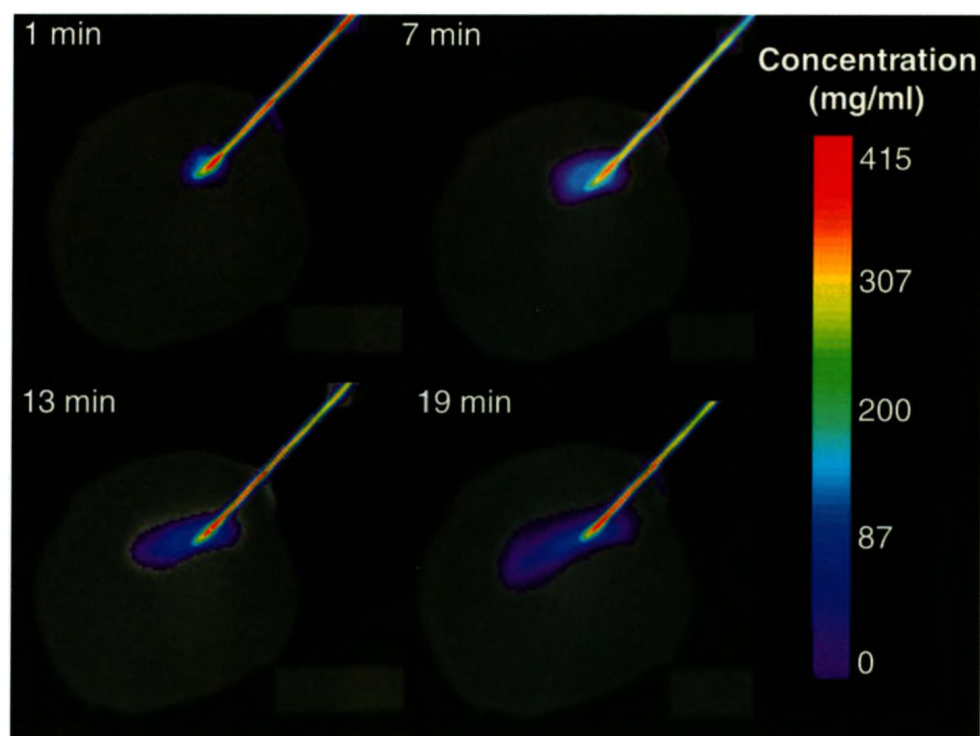


Figure 4.4 Micro-CT images with needle in place during injection

Micro-CT imaging of intravitreal injection and bolus formation in the vitreous with the needle in place during a 12 minute duration injection (0.144 ml/hr) using a syringe pump.

The slow and intermediate flow rates did not provide visualization of how the bolus formed over time due to the temporal resolution limitations of the scanner. A scan was completed in all cases immediately after the injection was completed and the surface area of the 30 μl volume difference is shown in Figure 4.5. A 30 μl sphere would have the surface area of 46.71 mm^2 and is shown in Figure 4.5 as a means of comparison. There does appear to be a trend of a higher surface area for faster injection flow rates. It was observed that a higher injection velocity resulted in the drug being ‘pushed’ further into the vitreous and therefore resulted in an unexpected initial shape and location. This was evident in both the hand injections and syringe pump injection.

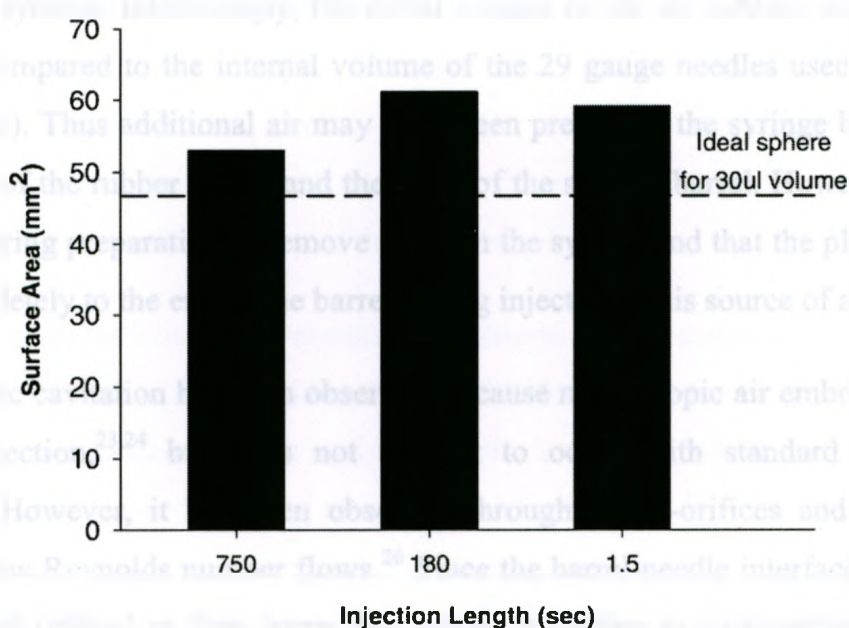


Figure 4.5 Surface area of bolus compared with injection duration

Measured surface area of a 30µl injected bolus of contrast agent following an injection at multiple flow rates (durations): 0.144 ml/hr (750 sec), 0.6 ml/hr (180 sec) and 72 ml/hr (1.5 sec). A comparison was made with that of an ideal sphere with a volume of 30 µl (dashed line).

4.4 Discussion

Although the presence of small air bubbles within the vitreous are not thought to be a significant risk for patients, it is desirable to minimize their size, since they may cause temporary vision impairment. In addition, the transport of the drugs from the injected boli may be hindered due to the increased tortuosity of the diffusion/flow path around the air bubbles. It is important to be aware of the factors influencing pharmacokinetics so that the standard method of drug administration is as effective as possible in disease treatment. Whilst the air bubbles are likely to migrate upwards (due to buoyancy forces), a patient's position during and following the injection, in addition to pressure gradients or flow *in vivo*, are also likely to affect air bubble movement. It was found that of the three specimens used for syringe pump injection, none had evidence of air bubbles following injection. Possible sources for these air bubbles may be inadequate de-airing of the needle barrel system, cavitation or air entrainment during insertion.

The most obvious source of the air bubbles would be transfer from the needle or the barrel of the syringe. Interestingly, the initial volume of the air bubbles was found to be quite large compared to the internal volume of the 29 gauge needles used (up to 5 to 6 times as great). Thus additional air may have been present in the syringe barrel, lying at the interface of the rubber piston and the sides of the syringe barrel. However, given the care taken during preparation to remove air from the system and that the plunger was not pushed completely to the end of the barrel during injections, this source of air is unlikely.

Hydrodynamic cavitation has been observed to cause microscopic air embolisms in other forms of injection,^{23,24} but it is not thought to occur with standard syringes and injections.²⁵ However, it has been observed through micro-orifices and micro-fluidic devices for low Reynolds number flows.²⁶ Since the barrel-needle interface is defined as a 'sharp-edged orifice' in flow terms, the sudden reduction in cross-sectional flow area will induce a static pressure drop at the vena contracta (narrowing of flow) that occurs just beyond the interface. If this drop is sufficiently large and the pressure begins to approach the vapor pressure of the fluid, then cavitation and the growth of micro-bubbles could occur in the flow. Whilst this mechanism is less likely for standard (4-5 second) injection times, this cannot be discounted at this stage for shorter periods of injection. Confirmation of this phenomenon would require further careful study and complex multi-phase computational fluid dynamics approaches.

Another possible source of air could be entrainment during needle penetration of the sclera. A number of examples of physical problems where small objects penetrate liquids and films leading to air entrainment are described in the literature.²⁷ It is therefore conceivable that surface tension forces at the air-liquid-needle interface are sufficient to pull small volumes of air into the vitreous as the bevel and needle penetrate the sclera. Further study of these injections in a sub-aqueous state would confirm this hypothesis.

Some prefilled syringes are available and useful in reducing or eliminating gas bubbles from the syringe. The techniques in which the syringes are filled vary greatly and not all methods are equally effective in removing air from the syringe barrel.²⁸ More advanced vacuum filling provides bubble-free filling and therefore improves dosing accuracy,

product stability, improved sterility and no introduction of air during injection. Recent work has shown foreign materials, such as silicone oil, may still be introduced during intravitreal injections when using prefilled syringes.⁸ If hydrodynamic cavitation is the source of air in the injection, prefilled syringes would not have any effect. Not all prefilled syringes are manufactured and filled in the same way, but they do provide potential for improving the efficacy of drug delivery in the eye.

Based on the observations of the resulting boli shapes after injection, delivery of the drug cannot be based on predictions where the initial bolus is assumed to resemble a sphere. Further experimental observations seems to indicate that the initial bolus shape is also related to the fluid velocity exiting the needle and the stability of the syringe. A higher injection velocity resulted in the injected solution to travel further into the vitreous and further deviated from an expected sphere bolus. The vitreous is a paucicellular hydrogel with primarily unbranched type II collagen fibrils and hyaluronic acid.²⁹ These fibrils form a tensioned semi-random polymer network, where the hyaluronic acid sustains the tension by osmotic (Donnan) swelling. Investigations of the elastic shear moduli using observations of spherical cavity instability of injected fluids into the vitreous cavity have indicated that this tensioned structure is relatively easy to disturb and that the destructure is strain rate (i.e. fluid velocity) dependent.³⁰ In addition, the fulcrum of the needle is the entry point of the sclera, which will effectively magnify any movements of the individual performing the injection. Thus the insertion of the needle, subsequent movement, outflow velocity and instabilities in the vitreal collagen network will all lead to the observed asymmetry of the boli.

For potential changes to be made to the delivery method of ocular drugs it is important to understand and address the factors in drug delivery that can be altered. Drug loss as a result of reflux has been shown to be a highly variable factor in ocular drug delivery. It has been estimated that 10% loss of drug could be substantial enough to alter the pharmacokinetics and therefore effectiveness in treating the disease.¹ Work has been completed recently that found the use of 30G needles and a deep injection helps to minimize reflux of drug during intravitreal injections.¹ The study showed that with minor modifications to injection supplies and technique, significant improvement can be made

to administering the drug in the expected manner, thereby maximizing the therapeutic effect. Our work has broadened and enhanced these observations with direct spatial and temporal visualizations of the drug bolus and associated phenomena following injection.

This is also the first work to date that has imaged an intravitreal injection while maintaining the needle inserted in the eye. Limitations of the work associated with injection flow rate is that it was a preliminary study that had only one specimen per group with use of the syringe pump. To determine statistical differences further work would be required. This experiment provided the necessary understanding of what is required to administer an injection using a syringe pump and better understand what effect flow rate has on intravitreal injections.

4.5 Conclusions

The observation and study of intraocular air bubbles, inconsistent bolus shapes and flow rate variations have demonstrated the importance of a consistent and accurate injection technique to administer the appropriate concentration of drug to the retinal tissue. They also suggest that the design and length of the needle and the injection fluid velocity must be carefully considered while administering intravitreal drugs, as this can alter the concentration and period of drug reaching the target site. Pharmacokinetic modeling assumptions must closely resemble clinical scenarios to provide the most meaningful results and this work has helped to develop a greater understanding of the asymmetrical initial bolus. It is only by making these anomalous features known and studying injection parameters that they can be better addressed to improve the efficacy of intravitreal drug delivery and perhaps influence the design of new drug delivery systems, all of which will improve patient outcomes and safety.

4.6 References

1. Hubschman, J.-P.; Coffee, R. E.; Bourges, J.-L.; Yu, F.; Schwartz, S. D. Experimental model of intravitreal injection techniques. *Retina* 30(1):167-173; 2010.
2. Jager, R. D.; Aiello, L. P.; Patel, S. C.; Cunningham, E. T. J. Risks of intravitreal injection: a comprehensive review. *Retina* 24(5):676-698; 2004.
3. Ozkiris, A.; Erkilic, K. Complications of intravitreal injection of triamcinolone acetonide. *Can J Ophthalmol* 40(1):63-68; 2005.
4. Jonas, J. B.; Spandau, U. H.; Schlichtenbrede, F. Short-term complications of intravitreal injections of triamcinolone and bevacizumab. *Eye* 22(4):590-591; 2008.
5. Somner, J. E. A.; Mansfield, D. Inadvertent injection of intravitreal air during intravitreal Lucentis injection for wet age-related macular degeneration: an undescribed complication. *Eye* 23(8):1744; 2008.
6. Freund, K. B.; Laud, K.; Eandi, C. M.; Spaide, R. F. Silicone oil droplets following intravitreal injection. *Retina* 26(6):701-703; 2006.
7. Bakri, S. J.; Ekdawi, N. S. Intravitreal silicone oil droplets after intravitreal drug injections. *Retina* 28(7):996-1001; 2008.
8. Liu, L.; Ammar, D. A.; Ross, L. A.; Mandava, N.; Kahook, M. Y.; Carpenter, J. F. Silicone oil microdroplets and protein aggregates in repackaged bevacizumab and ranibizumab: effects of long-term storage and product mishandling. *Invest Ophthalmol Vis Sci* 52(2):1023-1034; 2011.
9. Marmor, M. F.; Negi, A.; Maurice, D. M. Kinetics of macromolecules injected into the subretinal space. *Exp Eye Res* 40(5):687-696; 1985.
10. Kamei, M.; Misono, K.; Lewis, H. A study of the ability of tissue plasminogen activator to diffuse into the subretinal space after intravitreal injection in rabbits. *American Journal of Ophthalmology* 128(6):739-746; 1999.
11. Stocchino, A.; Repetto, R.; Cafferata, C. Eye rotation induced dynamics of a Newtonian fluid within the vitreous cavity: the effect of the chamber shape. *Phys Med Biol* 52(7):2021-2034; 2007.
12. Byeon, S. H.; Kang, S. Y. Pharmacokinetics. *Ophthalmology* 116(1):168-169; 2009.
13. Ethier, C. R.; Johnson, M.; Ruberti, J. Ocular biomechanics and biotransport. *Annu Rev Biomed Eng* 6:249-273; 2004.

14. Ghate, D.; Edelhauser, H. F. Ocular drug delivery. *Expert Opin Drug Deliv* 3(2):275-287; 2006.
15. Lee, B.; Litt, M.; Buchsbaum, G. Rheology of the vitreous body. Part 1: Viscoelasticity of human vitreous. *Biorheology* 29(5-6):521-533; 1992.
16. Lee, B.; Litt, M.; Buchsbaum, G. Rheology of the vitreous body. Part 3: Concentration of electrolytes, collagen and hyaluronic acid. *Biorheology* 31(4):339-351; 1994.
17. Tan, L. E.; Orilla, W.; Hughes, P. M.; Tsai, S.; Burke, J. A.; Wilson, C. G. Effects of vitreous liquefaction on the intravitreal distribution of sodium fluorescein, fluorescein dextran, and fluorescent microparticles. *Invest Ophthalmol Vis Sci* 52(2):1111-1118; 2011.
18. Maurice, D. Review: practical issues in intravitreal drug delivery. *J Ocul Pharmacol Ther* 17(4):393-401; 2001.
19. Li, S. K.; Jeong, E. K.; Hastings, M. S. Magnetic resonance imaging study of current and ion delivery into the eye during transscleral and transcorneal iontophoresis. *Invest Ophthalmol Vis Sci* 45(4):1224-1231; 2004.
20. Park, J.; Bungay, P. M.; Lutz, R. J.; Augsburger, J. J.; Millard, R. W.; Sinha Roy, A.; Banerjee, R. K. Evaluation of coupled convective-diffusive transport of drugs administered by intravitreal injection and controlled release implant. *J Control Release* 105(3):279-295; 2005.
21. Friedrich, S.; Cheng, Y. L.; Saville, B. Drug distribution in the vitreous humor of the human eye: the effects of intravitreal injection position and volume. *Curr Eye Res* 16(7):663-669; 1997.
22. Thompson, J. T. Kinetics of intraocular gases: disappearance of air, sulfur hexafluoride, and perfluoropropane after pars plana vitrectomy. *Arch Ophthalmol* 107(5):687-691; 1989.
23. Markus, H.; Israel, D.; Brown, M. M.; Loh, A.; Buckenham, T.; Clifton, A. Microscopic air embolism during cerebral angiography and strategies for its avoidance. *The Lancet* 341(8848):784-787; 1993.
24. Bove, A. A.; Gimenez, J. L. Computer analysis of flow characteristics of injection catheters. *Investigative Radiology* 3(6):427-432; 1968.
25. Meltzer, R. S.; Tickner, E. G.; Sahines, T. P.; Popp, R. L. The source of ultrasound contrast effect. *Journal of Clinical Ultrasound* 8(2):121-127; 1980.
26. Mishra, C.; Peles, Y. Cavitation in flow through a micro-orifice inside a silicon microchannel. *Physics of Fluids* 17(1):013601-013615; 2005.

27. Simpkins, P. G.; Kuck, V. J. On air entrainment in coatings. *J Colloid Interface Sci* 263(2):562-571; 2003.
28. Wagner, A. *Advances in Prefilled Syringe Technology. Innovations in Pharmaceutical Technology*. London, England: Samedan Ltd; 2008.
29. Foster, W. J. Vitreous substitutes. *Expert Rev Ophthalmol* 3(2):211-218; 2008.
30. Zimmerlin, J. A.; Sanabria-DeLong, N.; Tew, G. N.; Crosby, A. J. Cavitation rheology for soft materials. *Soft Matter* 3(6):763-767; 2007.

5.1 Introduction

Conventional drug and drug delivery systems for the past several decades have been based on a solid matrix or liquid solution. A fundamental understanding of drug delivery is required to design and develop novel drug delivery systems that can improve drug delivery and reduce side effects. The development of drug delivery systems is a multidisciplinary field that involves the design and development of drug delivery systems that can improve drug delivery and reduce side effects. The development of drug delivery systems is a multidisciplinary field that involves the design and development of drug delivery systems that can improve drug delivery and reduce side effects. The development of drug delivery systems is a multidisciplinary field that involves the design and development of drug delivery systems that can improve drug delivery and reduce side effects.

The development of drug delivery systems is a multidisciplinary field that involves the design and development of drug delivery systems that can improve drug delivery and reduce side effects. The development of drug delivery systems is a multidisciplinary field that involves the design and development of drug delivery systems that can improve drug delivery and reduce side effects. The development of drug delivery systems is a multidisciplinary field that involves the design and development of drug delivery systems that can improve drug delivery and reduce side effects. The development of drug delivery systems is a multidisciplinary field that involves the design and development of drug delivery systems that can improve drug delivery and reduce side effects.

Chapter 5

5 Modeling drug transport in the vitreous using computational fluid dynamics

This chapter explains the development of a computational fluid dynamics model for drug flow in the vitreous body. Model geometry and transport properties are based on those found in ex vivo experimentation using micro-CT. Validation of the model is completed by using the ex vivo experimental results presented in earlier chapters. The modeling presented is a simplified system of ocular drug flow using diffusion based transport analysis.

5.1 Introduction

Developing new drugs and drug delivery systems for the posterior segment of the eye has become a great interest of vision research. Computational modeling of drug flow is progressively being used in the quest for finding a method that requires fewer injections and provides more targeted delivery. CFD modeling allows for a variety of tests to be performed without using animal or human models. It provides a method of testing and insight into the pharmacokinetics of delivery systems such as controlled release implants,¹ controlled release drugs² and polymeric delivery systems.³ Recent studies have incorporated MRI imaging with model development, but focused on new drug delivery strategies, such as iontophoresis,^{4,5} rather than intravitreal injection.

Initial models of intravitreal drug delivery were developed using the simple geometry of a circle to represent the vitreous with retinal permeability being the only boundary condition.⁶ Several studies were developed upon these results and added fluid models beyond diffusion, such as Navier-Stokes^{7,8} and Darcy's Law.⁹ CFD models have been developed to study drug distribution in the vitreous following intravitreal injections.

Based on the results of the injected fluorophores in frozen sections of vitreous, a finite element model of the rabbit eye was created to study drug distribution after intravitreal injection of fluorescein-based compounds.⁷ Models were developed further by incorporating the lens and interaction with the anterior portion of the eye (aqueous humour and iris).⁷ Friedrich et al. used their model to determine the importance of position and volume of intravitreal injections and found that elimination and distribution of drug was significantly affected by the injection location.¹⁰ Further work was completed and found drugs travelled much faster in aphakic eyes (i.e. the absence of the lens) and retinal permeability is an important parameter to consider in understanding drug distribution in the vitreous.¹¹ All of this work demonstrated the complexity and need for better understanding of ocular drug flow following intravitreal injections, but very little has been validated by experimental evidence.

A major portion of work related to modeling ocular drug delivery has used the rabbit eye as a model.^{1,7,12} Rabbit eyes are very common in ophthalmic research for their similarity in size and properties to that of the human eye. However, rabbit eyes have a very large lens and as a result a much smaller vitreous volume than humans. When studying ocular drug flow in the vitreous, using a rabbit model, reduced vitreous volume is important to consider. Boundary interaction and distances to travel are also key variables to consider when developing a model that has the potential for human applications.

The purpose of this work is to develop a CFD model of a porcine eye using the model geometry and diffusivity values from micro-CT imaging. Validation of the model will be completed using the micro-CT acquired images of intravitreal injected contrast agents into the vitreous. It is anticipated the non-invasive imaging will provide important temporal and spatial background information to develop the fluid dynamics model resulting in a more complete understanding of ocular drug flow in the vitreous.

5.2 Methods

Model geometry, meshing and finite element modeling was performed within a commercially available software package (COMSOL Multiphysics, COMSOL Inc., Burlington MA). A 2-dimensional (2D) model was designed to validate the diffusion model and material properties. This 2D model was designed to be expanded to a 3-dimensional (3D) model that would maintain all of the same parameters.

5.2.1 Initial Conditions

An intravitreal injection was modeled as a hemi-spherical or tear drop bolus with a uniform concentration (Equation 5.1),

$$C_{t=0} = 10 \text{ mol/m}^3 \quad \text{for intravitreal injection} \quad (5.1)$$

The hemi-spherical shape was chosen because it is the initial bolus shape in previous works studying ocular drug flow in the vitreous and is a common clinical assumption. The hemi-spherical bolus was based on a symmetrical sphere of 30 μl volume, resulting in a 3.86 mm diameter. The tear drop shape was designed based on the experimental results found in the micro-CT study which demonstrated the initial bolus resembles a tear drop shape more often than a sphere. The dimensions of the tear drop bolus were 0.74 mm at the top, where the needle tip would be located, and 3.48 mm at its widest point near the bottom. The initial concentration everywhere else in the simulation was set to zero (Equation 5.2),

$$C_{t=0} = 0 \quad \text{everywhere outside the drug source} \quad (5.2)$$

5.2.2 Governing Equations

A purely diffusive model was designed to replicate the transport mechanisms occurring in the *ex vivo* experiment. To expand upon this model a convective component was added to represent what may be found for an *in vivo* animal model. To determine the convection transport of the drug, the Navier-Stokes equation (Equation 5.3) was used to solve the flow components of the vitreous humor. Navier-Stokes equations solve for the fluid motion using pressure, density and viscosity as parameters. The velocity results were then

coupled with the convection-diffusion transport equation to determine the distribution of drug concentration (Equation 5.4).

$$\rho U \cdot \nabla U = -\nabla P + \eta \nabla^2 U \quad (5.3)$$

$$\frac{\partial C}{\partial t} + U \cdot \nabla C = D \nabla^2 C \quad (5.4)$$

where ρ is the mass density, U is the velocity vector, P is the pressure, η is the viscosity, t is time, D is the diffusion coefficient and C is the concentration of the drug. It was assumed there was no drug reaction, degradation or retardation (due to surface effects), so these were not included in Equation 5.4.

5.2.3 Model Geometry

The geometry of the porcine model was based on a simplification of the micro-CT images acquired in the study. The thickness of the retina could not be calculated from the micro-CT imaging, therefore it was taken from literature.^{13,14} Table 5.1 provides details of the dimensions used in the formation of the porcine model and Figure 5.1 shows the final geometry used.

Table 5.1 Dimension for model eye

Geometric dimensions of the porcine eye used in the computational fluid dynamics model.

Tissue	Parameter	Value (mm)
Vitreous body	x-semiaxis	10.00
	y-semiaxis	10.75
Lens	x-semiaxis	3.50
	y-semiaxis	5.00
Retina	thickness	0.15
Anterior chamber	thickness	2.00

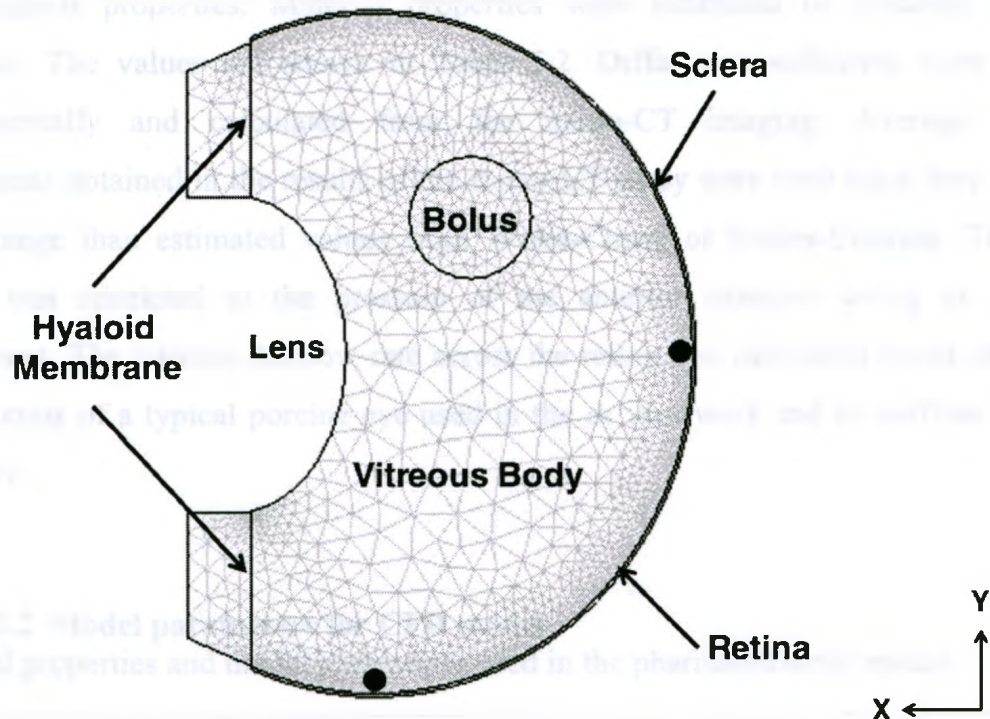


Figure 5.1 Domain of vitreous transport model

Porcine eye model geometry and finite element mesh with labeled anatomical features that were included in the model and the injected bolus shape/position. Dots (•) indicate points where measures were taken to represent concentration levels at the macula and bottom of the eye.

5.2.4 Boundary Conditions and Material Properties

Continuity was assumed for convection-diffusion in all regions except those impermeable to the drug. For the surfaces assumed to be impermeable to the drug, lens and sclera, a zero species gradient was used,

$$\frac{\partial C}{\partial n} = 0 \quad \text{at lens and sclera} \quad (5.5)$$

The hyaloid membrane and a small region of the anterior chamber were included to determine the concentration of drug that entered the anterior segment of the eye. Anatomically the hyaloid membrane is the boundary between the vitreous and anterior chamber. It is composed of highly porous tissue, therefore no resistance was included in

the transport properties. Material properties were estimated or obtained from the literature. The values are shown in Table 5.2. Diffusion coefficients were obtained experimentally and calculated from the micro-CT imaging. Average diffusion coefficients obtained in the results of the micro-CT study were used since they provide a wider range than estimated values from Wilke-Chang or Stokes-Einstein. The inflow source was restricted to the pressure of the anterior chamber acting as a normal component. The vitreous outflow rate across the retina was calculated based on the area of the retina of a typical porcine eye used in the *ex vivo* work and an outflow rate from literature.

Table 5.2 Model parameters for CFD model

Material properties and model parameters used in the pharmacokinetic model.

Constant	Value	Reference
Diffusion coefficient of iodine	$4.76 \times 10^{-6} \text{ cm}^2/\text{s}$	Calculated in this study
Diffusion coefficient of gold nanoparticles	$9.07 \times 10^{-6} \text{ cm}^2/\text{s}$	Calculated in this study
Density of vitreous	1 g/cm^3	Kaufman <i>et al.</i> ¹⁵
Density of iodine	1.406 g/cm^3	Nath <i>et al.</i> ¹⁶
Density of gold nanoparticles	1 g/cm^3	Estimated
Dynamic viscosity of vitreous	$0.00629 \text{ Pa}\cdot\text{s}$	Stocchino <i>et al.</i> ¹⁷
Dynamic viscosity of iodine	$0.002 \text{ Pa}\cdot\text{s}$	GE Healthcare ¹⁸
Dynamic viscosity of gold nanoparticles	$0.000911 \text{ Pa}\cdot\text{s}$	Nanoprobe ¹⁹
Intraocular pressure	2000 Pa	Stay <i>et al.</i> ²
Vitreous outflow through retina	$4.67 \times 10^{-3} \text{ cm/hr}$	Araie and Maurice ⁶

5.2.5 Solution Method

The model geometry was automatically meshed using the built-in software function to create triangular elements throughout the domains. Finite element method was used to solve the model, where discrete elements are solved using differential equations. To solve the computational model, Equation 5.3 was first solved to determine the velocity

distribution in the vitreous using Navier-Stokes equation. The solution was assumed to be time-independent and therefore unaffected by the action of the diffusing drug mimic. The resulting velocity field was exported and used in the time-dependent diffusion-convection equation (Equation 5.4) to solve for the concentration distribution of the drug mimic in the vitreous. All simulations were run on a 2 GHz Core 2 Duo CPU running Windows.

5.3 Results

5.3.1 Validation of Model with Experimental Results

The maximum drug concentration is assumed to be at the center of the bolus. Time dependent measurements were taken from both experimental and modeling cases and are shown in Figure 5.2. For the purpose of this validation, the initial concentration of the bolus in the simulation was set to 150 mg/ml to correlate with the iodine solution concentration used in the *ex vivo* experiment. A strong correlation was found between the two and the model was well within the margins of error from the experimental results.

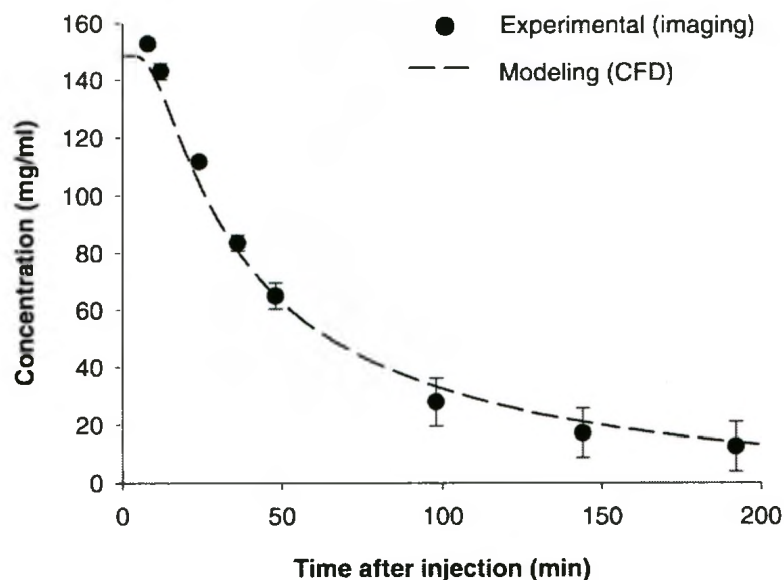


Figure 5.2 Concentration at the center of the injected bolus

Numerical model validation with *ex vivo* experiment data of concentration values at center of bolus up to 200 minutes post-injection, using measured values from experimental contrast agent in micro-CT imaging (dots) and CFD modeling (dashed line).

5.3.2 Effect of Diffusion Coefficients

Diffusion coefficients used in the model were chosen as the two extremes for the contrast agents under study. In Figure 5.3, the model predicted concentration profiles are shown for the time point of 3 hours, the end point of experimental work completed using micro-CT. The profiles indicate due to the small differences in the diffusion coefficient, the maximum concentration of iodine within the eye remains at 1.7 times greater than for gold nanoparticles. The area of greatest importance is the back of the eye, or the macula. Figure 5.4 provides greater information into concentration at specific points by depicting the model-predicted concentration gradients for (A) iodine solutions and (B) gold nanoparticles at specific points in the eye of the macula and bottom retina. Iodine had the lower diffusion coefficient and resulted in longer period for the model to reach uniform concentration throughout the entire vitreous. The model was run for a simulation of 24 hours and iodine had still not reached uniform concentration within the model eye. Gold nanoparticles had a higher diffusion coefficient and reached uniform concentration more rapidly after approximately 15 hours. However, the iodine remained at a slightly higher concentration at the macular for a longer period of time than the gold nanoparticles.

Figure 5.3 Concentration profiles from a 3D model. Model parameters: concentration of contrast agent at the injection site is 10^{-4} mol/L, diffusion coefficient of iodine is 1.5×10^{-6} cm²/s, and diffusion coefficient of gold nanoparticles is 2.5×10^{-6} cm²/s. The concentration of contrast agent is shown in the color scale on the right.

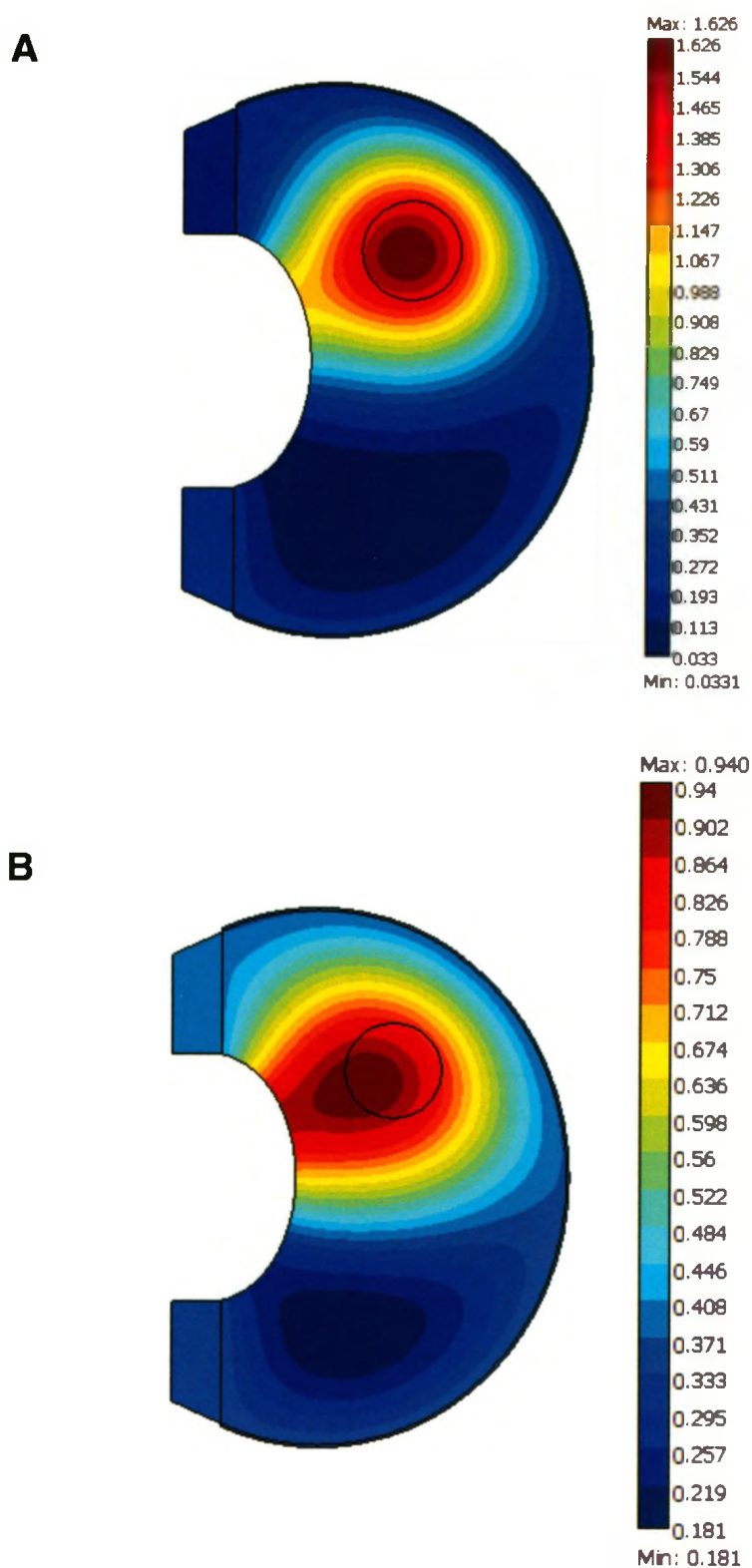


Figure 5.3 Concentration profiles from CFD model

Model predicted concentration profiles for **A)** iodine solution ($4.76 \times 10^{-4} \text{ mm}^2/\text{s}$) and **B)** gold nanoparticles ($9.07 \times 10^{-4} \text{ mm}^2/\text{s}$) at 3 hours post-injection. Units for the concentration profiles are mol/m^3 .

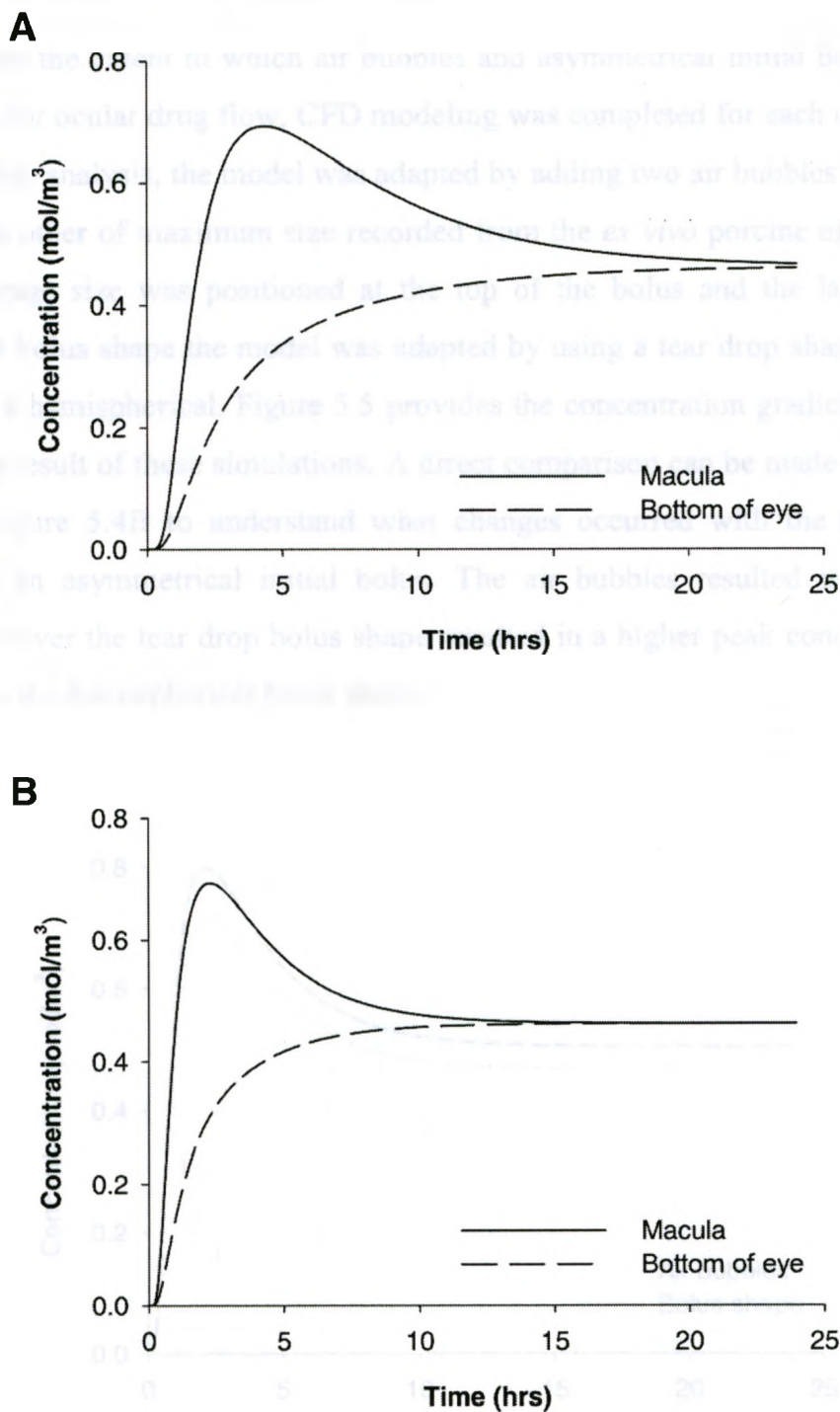


Figure 5.4 Concentration gradient at boundary points for contrast agents

Differing diffusion coefficients were used in the model between **A**) iodine solution ($4.76 \times 10^{-4} \text{ mm}^2/\text{s}$) and **B**) gold nanoparticles ($9.07 \times 10^{-4} \text{ mm}^2/\text{s}$). Boundary points are located at the macula (back of the eye) and bottom of the retina/eye.

5.3.3 Air Bubbles and Bolus Shape

To determine the extent to which air bubbles and asymmetrical initial bolus shape were responsible for ocular drug flow, CFD modeling was completed for each of the scenarios. For air bubble analysis, the model was adapted by adding two air bubbles, one of average size and the other of maximum size recorded from the *ex vivo* porcine experiments. The one of average size was positioned at the top of the bolus and the larger one at the bottom. For bolus shape the model was adapted by using a tear drop shaped initial bolus rather than a hemispherical. Figure 5.5 provides the concentration gradients found at the macula as a result of these simulations. A direct comparison can be made with the graphs found in Figure 5.4B to understand what changes occurred with the presence of air bubbles or an asymmetrical initial bolus. The air bubbles resulted in no significant change, however the tear drop bolus shape resulted in a higher peak concentration at the macula than the hemispherical bolus shape.

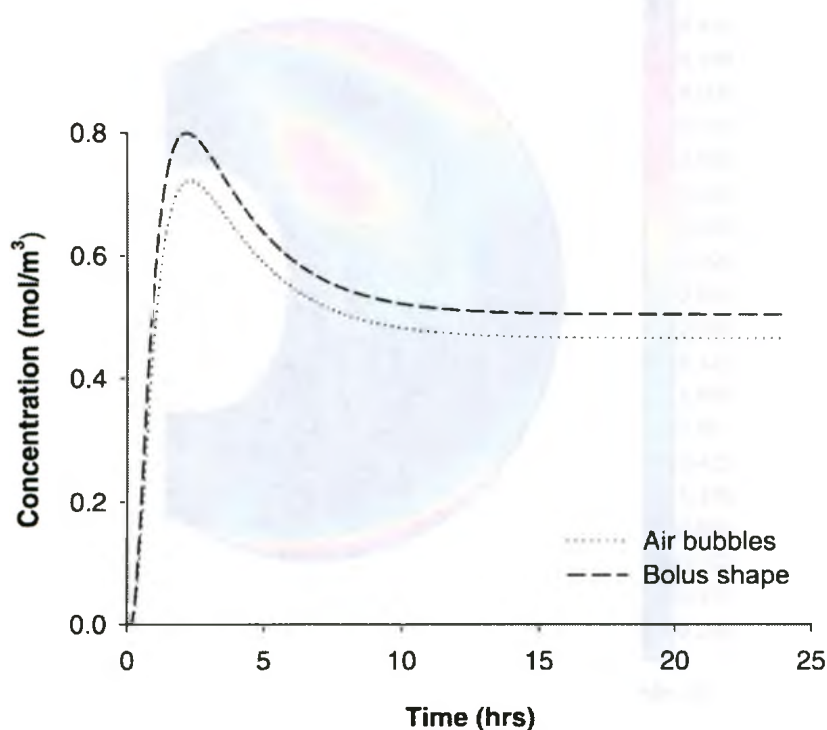


Figure 5.5 Concentration gradient at the macula for anomalous features

Model simulations were performed with the presence of air bubbles around the initial bolus (dotted) and with the initial bolus in the shape of a tear drop (dashed). Diffusion coefficients used in the simulation were for gold nanoparticles ($9.07 \times 10^{-4} \text{ mm}^2/\text{s}$).

5.3.4 Convection

The results of the convection-diffusion model simulations showed that the distribution of the injected solution reached uniform concentration more rapidly with the presence of convection, but concentration profiles remained very similar to those shown in Figure 5.3. Most interestingly, the concentration of the injected drug at the macula remained at a higher concentration for a longer period. Understanding the affect an injected drug has on the normal convective flow of the eye is also important. The convective flux is shown in Figure 5.6 and demonstrates how the distribution of an injected solution, in this case gold nanoparticles, is influenced by active flow. A non-uniform flow pattern is also influenced as a result of the differences in viscosity and density of the introduced drug.

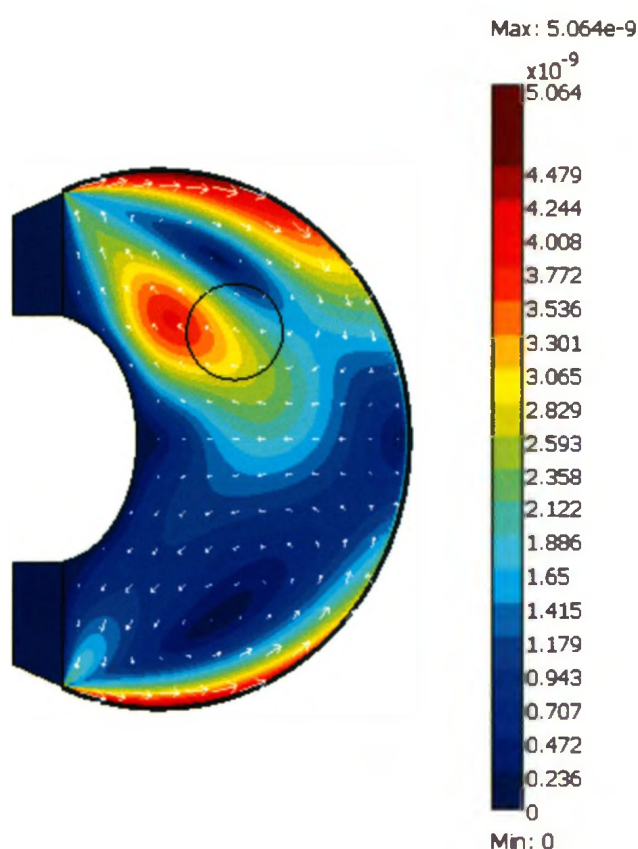


Figure 5.6 Convective flux and velocity fields in CFD model

Convective flux of the vitreous body is shown in the contour plot and velocity field is depicted by the arrows with their respective magnitude. Units of the convective flux profiles are $\text{mol/m}^2\cdot\text{s}$.

5.4 Discussion

A model was developed for simulation of intravitreal drug delivery in the vitreous body. This model is unique from previous ones in that it is based on diffusion coefficients that were obtained from extensive experimental data and studies anomalous features of intravitreal injections. Developing a computational fluid dynamics model is a favourable method in studying fluid transport, as parameters can be easily manipulated and parametric studies performed. This model has been developed so that it can be used to study other drugs and include additional parameters such as boundary permeability, metabolism of drug and altered injection sites. A well-developed model can also be used to minimize the number of animals used for *in vivo* experimentation³ by doing some of the analysis using a CFD model rather than animal model. However, it is very important to ensure the model has been developed and validated with high quality experimental results.

The strong correlation between the CFD model and the *ex vivo* data as shown in Figure 5.2 is an indication that the model developed is representative of what is occurring experimentally in porcine eyes when injected with contrast agent. A primary objective of this work was to develop a simulation from a computational model that strongly resembled the results found experimentally. Correlation of maximum concentration values in part demonstrates the correct domain parameters have been set, such as diffusion coefficient, density and viscosity. The model solutions also demonstrated strong convergence with reciprocal of step size values ranging from 10^{-3} and 10^{-4} .

Detailed concentration contour profiles were obtained from the CFD model as shown in Figure 5.3. These images provide the spatial information of how a drug is distributed throughout the vitreous. Figure 5.4 provides specific point information within the vitreous and comparison of the concentration at the target site, the macula, and a peripheral region at the bottom of the eye. From these profiles we can see that the drug reaches the macula quite quickly and peaks at approximately 5 hours. However, it is 7% of the concentration that was initially injected. That carries huge implications for drug delivery and the potential to overdose healthy areas of the eye in order to reach sufficient levels at the target site.

Modeling based on the presence of air bubbles and altered bolus shapes revealed minor deviations from the concentration gradients that did not have these features. Air bubbles resulted in slightly higher peak values of drug concentration at the macula with 0.3% more of the initial concentration than the normal. The teardrop bolus shape had more of an effect and resulted in 1.1% more of the initial concentration at the macula than in the case of a hemispherical bolus. The full extent of the asymmetrical bolus may not be realized because the model is constrained to 2D and could result in larger differences in a 3D model.

Convection has been shown to be an important parameter to include in ocular drug delivery studies, particularly for humans models.² When a convective component was implemented in this study's model, the concentration profiles did not have much of an effect when coupled with diffusion. This could be attributed to the fact that the molecular weight of the drug mimic used in this study were much higher than those used in other studies that cited convection as a significant transport mechanism.^{2,8} However, by creating this diffusion based model an important step has been made in learning more about ocular drug delivery. It has been shown by Missel *et al.* that it is vital to separate experiments to deduce diffusion from other transport mechanisms due to the nonlinear way that they interact.²⁰

A limitation of this model is that it lacks the 3D information that was provided in micro-CT imaging. However, the 2D model is simpler to design and implement in terms of requiring less computational power and time. There are some limitations to the quantitative data provided since homogenous properties of the vitreous and no lateral diffusion/dispersion must be assumed. The third dimension that is missing from this model would be side-to-side if you were looking into the eye from the front or back. This direction is expected to have the same transport properties as the other horizontal direction from front to back while boundary interaction would only be an issue at later time points. The effect of gravity, particularly for high molecular weight drugs, could also be introduced as a potential transport mechanism in the vertical direction as some characteristics of it were displayed in micro-CT imaging.

5.4.1 Translation to Human Model

CFD modeling allows for developed models to be easily translated to other applications or systems. It allows for an intermediary step to be established between animal models and human testing, by developing a CFD human model. Model geometry can be altered to replicate that of the human eye and known material properties and boundary conditions revised. The realized properties such as diffusion coefficient and density driven flow would be maintained and applied to the human model. The results of such a simulation would more closely resemble what may actually occur in a human eye. While the results would be based on some assumptions, the efficiency and lack of requirements for human subjects makes the research particularly appealing for drug delivery studies.

5.5 Conclusions

A computational fluid dynamics model has been developed based on parameters obtained from experimental data. Results from the model correlated extremely well with those found in the experimental results performed using porcine eyes. The model is able to study the quantitative effects of diffusion or convection and the introduction of anomalous features on drug concentration within the vitreous following an injection. The model is an excellent resource to create a correlation between *ex vivo* and computational experimentation and allows for model enhancements or adaptations to be made for future work.

5.6 References

1. Park, J.; Bungay, P. M.; Lutz, R. J.; Augsburger, J. J.; Millard, R. W.; Sinha Roy, A.; Banerjee, R. K. Evaluation of coupled convective-diffusive transport of drugs administered by intravitreal injection and controlled release implant. *J Control Release* 105(3):279-295; 2005.
2. Stay, M. S.; Xu, J.; Randolph, T. W.; Barocas, V. H. Computer simulation of convective and diffusive transport of controlled-release drugs in the vitreous humor. *Pharm Res* 20(1):96-102; 2003.
3. Tojo, K.; Isowaki, A. Pharmacokinetic model for in vivo/in vitro correlation of intravitreal drug delivery. *Adv Drug Deliv Rev* 52(1):17-24; 2001.
4. Li, S. K.; Jeong, E. K.; Hastings, M. S. Magnetic resonance imaging study of current and ion delivery into the eye during transscleral and transcorneal iontophoresis. *Invest Ophthalmol Vis Sci* 45(4):1224-1231; 2004.
5. Molokhia, S. A.; Jeong, E. K.; Higuchi, W. I.; Li, S. K. Transscleral iontophoretic and intravitreal delivery of a macromolecule: study of ocular distribution in vivo and postmortem with MRI. *Exp Eye Res* 88(3):418-425; 2009.
6. Araie, M.; Maurice, D. M. The loss of fluorescein, fluorescein glucuronide and fluorescein isothiocyanate dextran from the vitreous by the anterior and retinal pathways. *Exp Eye Res* 52(1):27-39; 1991.
7. Friedrich, S.; Cheng, Y. L.; Saville, B. Finite element modeling of drug distribution in the vitreous humor of the rabbit eye. *Ann Biomed Eng* 25(2):303-314; 1997.
8. Kim, H.; Lizak, M. J.; Tansey, G.; Csaky, K. G.; Robinson, M. R.; Yuan, P.; Wang, N. S.; Lutz, R. J. Study of ocular transport of drugs released from an intravitreal implant using magnetic resonance imaging. *Ann Biomed Eng* 33(2):150-164; 2005.
9. Xu, J.; Heys, J. J.; Barocas, V. H.; Randolph, T. W. Permeability and diffusion in vitreous humor: implications for drug delivery. *Pharm Res* 17(6):664-669; 2000.
10. Friedrich, S.; Cheng, Y. L.; Saville, B. Drug distribution in the vitreous humor of the human eye: the effects of intravitreal injection position and volume. *Curr Eye Res* 16(7):663-669; 1997.
11. Friedrich, S.; Saville, B.; Cheng, Y. L. Drug distribution in the vitreous humor of the human eye: the effects of aphakia and changes in retinal permeability and vitreous diffusivity. *J Ocul Pharmacol Ther* 13(5):445-459; 1997.
12. Tojo, K. J.; Ohtori, A. Pharmacokinetic model of intravitreal drug injection. *Math Biosci* 123(1):59-75; 1994.

13. Buttery, R. G.; Hinrichsen, C. F. L.; Weller, W. L.; Haight, J. R. How thick should a retina be? A comparative study of mammalian species with and without intraretinal vasculature. *Vision Research* 31(2):169-187; 1991.
14. Ruiz-Ederra, J.; García, M.; Hernández, M.; Urcola, H.; Hernández-Barbáchano, E.; Araiz, J.; Vecino, E. The pig eye as a novel model of glaucoma. *Exp Eye Res* 81(5):561-569; 2005.
15. Kaufman, P. L.; Alm, A.; Adler, F. H. *Adler's physiology of the eye : clinical application*. St. Louis: Mosby; 2003.
16. Nath, R.; Yue, N.; Weinberger, J. Dose perturbations by high atomic number materials in intravascular brachytherapy. *Cardiovascular Radiation Medicine* 1(2):144-153; 1999.
17. Stocchino, A.; Repetto, R.; Cafferata, C. Eye rotation induced dynamics of a Newtonian fluid within the vitreous cavity: the effect of the chamber shape. *Phys Med Biol* 52(7):2021-2034; 2007.
18. Product monograph: Omnipaque (iohexol injection). GE Healthcare Canada; 2006.
19. Product information and instructions: AuroVist™ gold nanoparticle x-ray contrast agent. Nanoprobe Inc.; 2009.
20. Missel, P. J.; Chastain, J.; Yaacobi, Y.; Mitra, A. K.; Kompella, U.; Kansara, V.; Duvvuri, S.; Amrite, A.; Cheruvu, N. Delivery of anecortave acetate from an ocular implant: a finite element physiologic based pharmacokinetic ocular model including regional partitioning and choroidal elimination. *AAPS Annual Meeting*; 2005.

Chapter 6

6 General Discussion and Conclusions

This chapter will provide a brief summary of how each previously presented objective was addressed in the research. Limitations of ex vivo experimentation and the use of drug mimics will be discussed and means of addressing each will be suggested. Potential directions that this work can be carried out in the future are explored and the overall significance of the work completed is highlighted with potential clinical and research contributions.

6.1 Summary

The ability to provide a greater understanding of drug distribution and fate of ocular drug administration is vital information that can have major clinical implications. Intravitreal injections are commonly used to administer drugs to the posterior segment of the eye, but little is known as to how the drug flows through the vitreous once it has been injected. Use of intravitreal injections for the treatment of AMD and other diseases continues to increase as new drugs are developed and drug costs decrease or are covered by health insurance.^{1,2} Toxicological impact and concentration levels of intravitreal injections is important because the drug administered directly into the eye.³ Through the integration of non-invasive imaging and computational modeling, new knowledge can be obtained to aide in developing changes or alternatives to the current method of drug administration.

To visualize the progression of drug flow through the vitreous in micro-CT imaging, two contrast agents were compared as possible drug mimics. Iodine solutions have a very low molecular weight and have been well studied in biological systems.^{4,5} Gold nanoparticles have a molecular weight that is similar to that of some anti-VEGF drugs used in AMD therapy, but is a relatively new contrast agent for x-ray imaging.^{6,6} A variety of testing

was performed on each of the contrast agents including concentration calibration, dilution from the vitreous over time and diffusivity, to determine if gold nanoparticles were a viable alternative as a drug mimic for intravitreal injections. It was found that gold nanoparticles can be used at lower concentrations for an extended period of time to maintain sufficient contrast over iodinated solutions and possess a closer molecular weight to intravitreal drugs.

Micro-CT imaging of drug mimic flow through the vitreous allows for spatial and temporal concentration profiles to be obtained. This important information allowed for accurate diffusivity estimates to be made using Crank's passive diffusion equation and CFD. In addition, time dependent differences in diffusion coefficients led to the examination of how the drug interacts with the domain boundaries. The use of an animal model allows for insight into the mechanisms of ocular drug transport and the use of specialized equipment and experimental configurations that would not be possible in human subjects. Furthermore, *ex vivo* testing allows for evaluation and optimization of the experimental methods without the use of live animals.

Complications or abnormalities that develop as a result of intravitreal injections are important aspects to be considered when studying ocular drug flow. It was shown in the *ex vivo* experiments that typical intravitreal injections are likely to result in anomalous features. These can include air bubbles, the initial bolus taking on the form of irregular shapes and differing flow rate of the injection, all of which may impact drug delivery. This is the first work that has addressed any of these unexpected characteristics, in part due to the unique set up of non-invasive imaging. As a result this could help develop more accurate pharmacokinetic computational models.

Using the knowledge gained from the *ex vivo* specimens imaged using micro-CT and analyzed for passive diffusion, a porcine eye model was designed for use in CFD modeling. Model dimensions were values measured from the micro-CT images and assumptions used in previous models, such as bolus shape, were revised to account for what was found from the imaging. Diffusion coefficient values that were calculated in earlier work were used within the model and resulted in a strong correlation with the

experimental concentration results. Spatial and temporal dependent drug concentration was the outcome of interest. The necessity to separate transport mechanisms⁷ was successfully accomplished using *ex vivo* data and allowed for a strong understanding of the diffusive nature of ocular drug flow in the vitreous. The developed model provides a strong foundation for expansion into a more complex 3D and constitutive CFD models of ocular drug flow in the vitreous.

6.2 Limitations

All experimental work presented here utilized *ex vivo* porcine and rabbit eyes. This is an obvious limitation as it does not allow for a full understanding of ocular drug transport within the vitreous because of the absence of any active flow. A pilot *in vivo* experiment was performed with an anesthetized rabbit and syringe pump. Significant problems occurred with needle positioning and stability in addition to the challenge of the small bore size of the micro-CT. These experiments would be possible if a custom designed micro-CT bed was designed to hold the rabbit and position the syringe. Preliminary drawings have been designed for this set up and may be employed in future work. Despite the inability to acquire *in vivo* data, it is now fully understood what is required in future work if an *in vivo* setup is desirable.

Radiopaque contrast agents were required for the injected solution to be detectable in the micro-CT scans for an extended period of time at a measurable concentration. The two contrast agents utilized, iodine and gold nanoparticle solutions, were classified as drug mimics for this work. They were used because pharmaceutical drugs used in intravitreal injections would not be detected in the micro-CT imaging as they do not possess the radiopaque properties required to be viewed from the background or vitreous grey scale intensity. Therefore, it cannot be assumed that clinical drugs would act in exactly the same manner as the contrast agents when flowing through the vitreous. An important aspect of this work was understanding the properties of the contrast agents and commonly used intravitreal drugs. From this it was inferred that gold nanoparticles would act in much the same way as the most common intravitreal drugs.

6.3 Future Work

Important steps of this work have been completed and have provided a strong foundation for further work to be completed. Minimum concentrations levels of the contrast agents studied have been established for future work to balance sufficient signal intensity with cost. Gold nanoparticles provide a variety of options with the ability to tag drugs and/or dyes to the nanoparticles. This would provide the option to study the drug's presence by multiple imaging modalities and provide insight into how the drug interacts with the retinal tissue once it reaches the posterior boundary of the eye.

Micro-CT imaging an *in vivo* rabbit model would provide the additional active flow and clearing behaviour absent in the presented experimental data. Diffusion has been shown to be a major contributing factor, if not the principal factor, in drug transport in the vitreous. With the knowledge gained from the *ex vivo* data analysis, the method to deconvolve diffusive flow is now known and would play an important role in understanding the degree to which active and passive flow play a role.

Advanced CFD modeling could be employed by creating a fully developed 3D model of the animal model eye, porcine or rabbit. This model could be used to better understand the full effect the drug properties have on ocular drug flow. Specifically, to investigate the effect of density, viscosity and molecular weight on drug flow and develop recommended prescribing information for a drug with a particular set of properties to ensure the required concentration reaches the target site for a sufficient amount of time, while not reaching levels of toxicity. Development of new administration methods of drugs to the vitreous is gaining popularity and this model could be adapted to understand where the ideal location for drug administration.

6.4 Significance

The ability to accurately model drug transport following an intravitreal injection provides vital information to better understand the concentration and time frame for the drug to reach the target site. By addressing anomalous features not otherwise studied, the work provides insight into potential variation that exists between clinically administered intravitreal injections and those modeled in pharmacokinetic studies. The approach of creating a link between experimental pharmacokinetic data found from non-invasive imaging with CFD modeling makes this work unique and novel. The findings permit the development of more accurate predictive tools or models to better understand and optimize ocular drug delivery. These tools can be used to provide the medical community and industry with the ability to design and test new drugs and drug delivery systems for clinical application.

6.5 References

1. Campbell, R. J.; Bronskill, S. E.; Bell, C. M.; Paterson, J. M.; Whitehead, M.; Gill, S. S. Rapid expansion of intravitreal drug injection procedures, 2000 to 2008: a population-based analysis. *Arch Ophthalmol* 128(3):359-362; 2010.
2. Brechner, R. J.; Rosenfeld, P. J.; Babish, J. D.; Caplan, S. Pharmacotherapy for Neovascular Age-related macular degeneration: an analysis of the 100% 2008 Medicare fee-for-service part B claims file. *American Journal of Ophthalmology* 151(5):887-895.e881; 2011.
3. Penha, F. M.; Rodrigues, E. B.; Furlani, B. A.; Dib, E.; Melo, G. B.; Farah, M. E. Toxicological considerations for intravitreal drugs. *Expert Opinion on Drug Metabolism & Toxicology* 7(8):1-14; 2011.
4. Szymanski-Exner, A.; Stowe, N. T.; Salem, K.; Lazebnik, R.; Haaga, J. R.; Wilson, D. L.; Gao, J. Noninvasive monitoring of local drug release using X-ray computed tomography: optimization and in vitro/in vivo validation. *J Pharm Sci* 92(2):289-296; 2003.
5. Nath, R.; Yue, N.; Weinberger, J. Dose perturbations by high atomic number materials in intravascular brachytherapy. *Cardiovascular Radiation Medicine* 1(2):144-153; 1999.
6. Hainfeld, J. F.; Slatkin, D. N.; Focella, T. M.; Smilowitz, H. M. Gold nanoparticles: a new X-ray contrast agent. *Br J Radiol* 79(939):248-253; 2006.
7. Missel, P. J.; Chastain, J.; Yaacobi, Y.; Mitra, A. K.; Kompella, U.; Kansara, V.; Duvvuri, S.; Amrite, A.; Cheruvu, N. Delivery of anecortave acetate from an ocular implant: a finite element physiologic based pharmacokinetic ocular model including regional partitioning and choroidal elimination. *AAPS Annual Meeting*; 2005.

Appendix A – Eye Planes/Orientation

To help understand the orientation and use of planes for the eye in this study, Appendix A provides a slice and label for each plane. The lens is labeled in each image it is visible and the cornea is depicted with an arrow. The axial plane refers to a top down view where all sides can be seen. The coronal plane refers to the plane from one side to the other or what one would see looking into the eye or from the back. The sagittal plane refers to a side on view of the eye where you can see from the front of the cornea to the back of the retina.

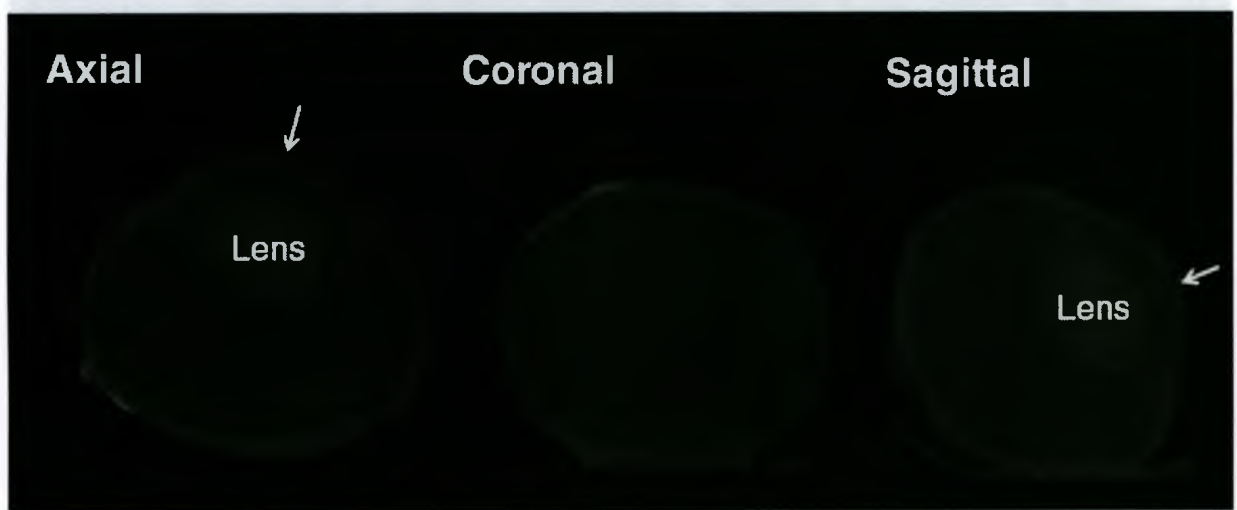


Figure A.1 Planes used for orientation of the eye in analysis of micro-CT images
The arrow indicates the cornea and the lens is labeled.

Figure B.1: Isosurfaces representing the diffusing bodies over time

The top surface represents the cornea (anterior) and the bottom surface represents the retina (posterior).

Appendix B – Contrast Agent ROIs

An example of the 3D regions of interest (ROIs) based on concentration levels of the contrast agent/drug mimic in the vitreous are shown in Figure A.2. The ROIs are representative of grey scale intensities and are from time points of 8, 48 and 192 minutes post-injection, from smallest to biggest.

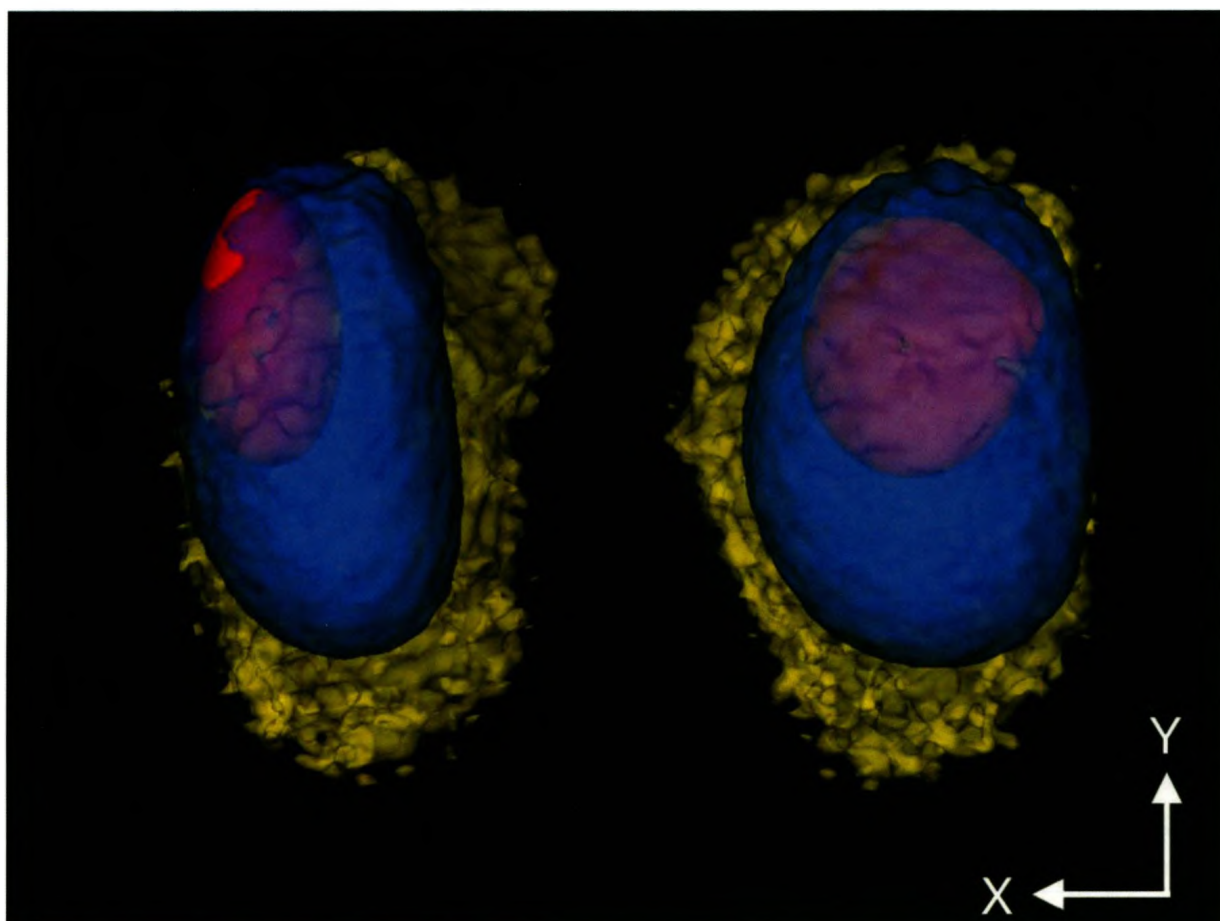


Figure B.1 Isosurfaces representing the diffusing bolus over time

The red surface represents 8 minutes post-injection, the blue 48 minutes and the yellow 192 minutes.

Appendix C – Contrast Agent Bolus Signal Profiles

Examples of signal profiles obtained from the micro-CT images are shown below for two specimens used in calculating the diffusion coefficients.

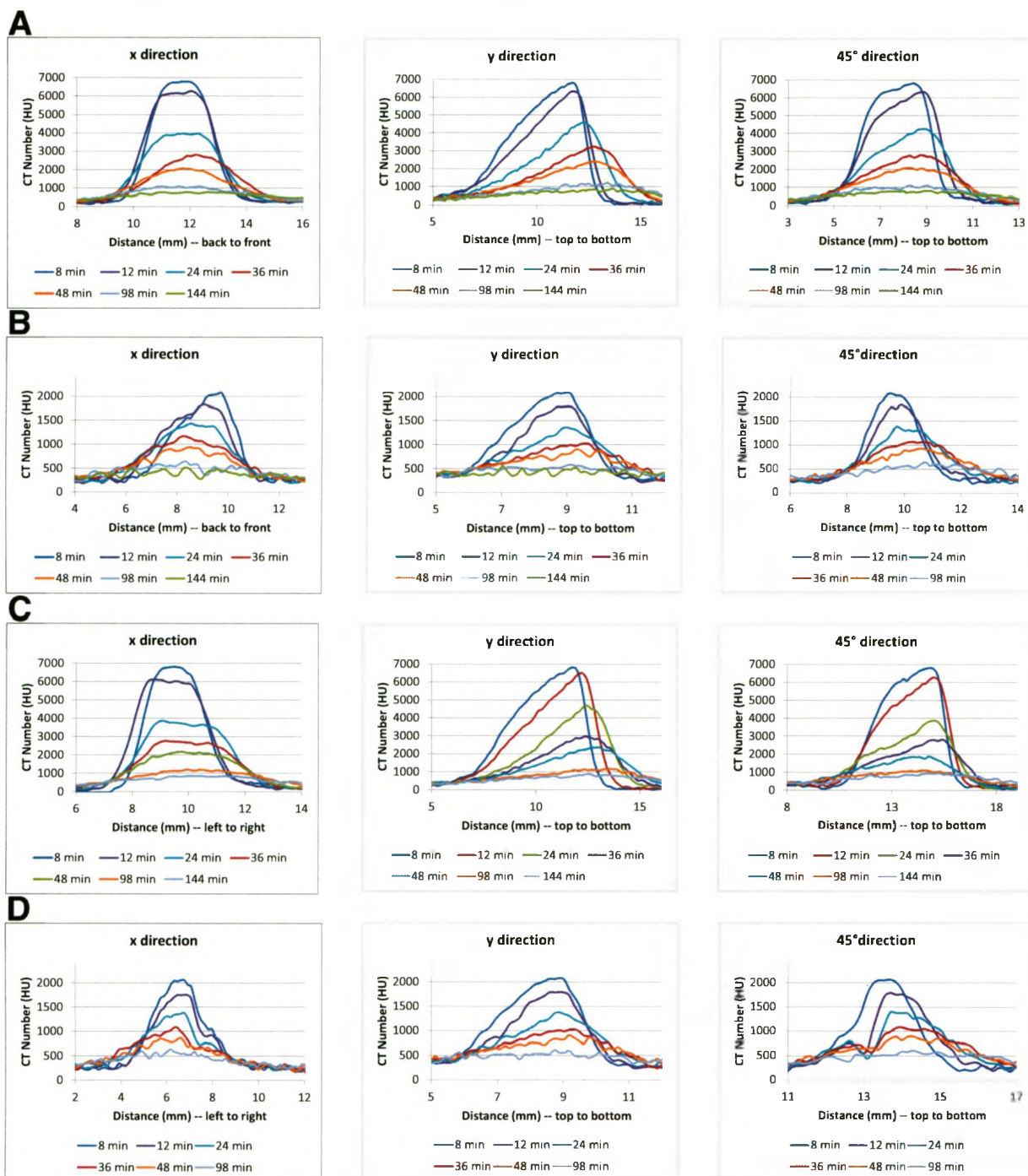


Figure C.1 Line signal profiles through the bolus

Signal intensity vs. distance taken at each time point in the x (horizontal), y (vertical) and 45° directions for A) 150 mg/ml iodine in sagittal plane B) 150 mg/ml iodine in coronal plane C) 37 mg/ml iodine in sagittal plane D) 37 mg/ml iodine in coronal plane.

Appendix D – MATLAB Implementation Code

Custom made MATLAB optimization code for calculating curve of best fit with diffusion coefficient variable.

```
%Calculates the predicted concentration values using the passive
diffusion
%equation (Crank) based on the distance input.
%
%Where:
%I = intensity line plot; Co = initial concentration; V =
injection volume;
%D = diffusion coefficient; t = time since injection
%
%Created by CAS on 04-Dec-09.

clear all
close all

%global r;
%global Co;
global t;
%global a;

%Load txt file
filename = input('Enter file name: ','s');
I = load(filename);

%Required user input values
%Co = input('Enter value of Co: ');
t = input('Enter value of t (sec): ');

%Defined values
I0 = I;
d = I(:,1);
Co = 4148;
%t = 2880;
V = 30;
a = ((V*3)/(4*pi))^(1/3);
D0 = 4E-4;
xmax = 0;

%Calculate FWHM & SD
width = fwhm(I(:,1),I(:,2));
SD = width/(2*sqrt(2*(log(2))));
SD1 = (0.5*width)+SD;
SD2 = (0.5*width)+(2*SD);
SD3 = (0.5*width)+(3*SD);
```

```

%Center distance values about zero
[M,N] = max(I0);
dmax = I0(N(1,2),1);
r = I(:,1) - (dmax+1E-10); %cannot have r = 0 b/c NaN will be
returned and optimization terminated

%Calculate window
plot(r,I(:,2)); hold on;
plot(xmax+SD1,0:2000,'r:',xmax-SD1,0:2000,'r:');
plot(xmax+SD2,0:2000,'b:',xmax-SD2,0:2000,'b:');
plot(xmax+SD3,0:2000,'g:',xmax-SD3,0:2000,'g:');
hold off;
%d = I(:,1);
disp('Select a left point and right point to define the
window. ');
I = I(:,2);
[W1,W2]=ginput(2);
low=find(r>W1(1),1,'first');
high=find(r<W1(2),1,'last');

r = r(low:high);
I = I(low:high);
plot(r,I)
%plot(r(low:high),I(low:high))

%Calculate background
plot(I0);
disp('Select points to calculate a background average. Press
ENTER key when done. ');
[px,qy] = ginput;
back = mean(qy);

%Signal intensity is defined by removing user-defined background
signal
I = I - back;

%D = lsqcurvefit('Crank',D0,r,I);
[D,resnorm,residual,exitflag,output,lambda,J] =
lsqcurvefit('Crank',D0,r,I);
C = Crank(D,r);
D

%Calculate coefficient of determination
MeanY = mean(I);
R2 = 1-(sum((I-C).^2)/sum((I-MeanY).^2))

```



```

%Plot observed and predicted results on the same graph
plot(r,I,'k-',r,C,'k:')
legend('Observed','Predicted')
xlabel('Distance from center (mm)')
ylabel('Concentration (AU)')

% Use NLPREDCI to find confidence intervals on the model's
response
[ypred,delta]=nlpredci('Crank',r,D,residual,'jacobian',J);
CI = max(delta);

% Plot the confidence intervals with the original data -- ypred &
C are the SAME!
figure
plot(r,ypred)
hold on
plot(r,I,'+r')
plot(r,ypred + CI,'--g')
plot(r,ypred - CI,'--g')

%Output matrix
OUTPUT = [t, V, back, min(r), max(r), D, R2, CI]
clipboard('copy', OUTPUT);

```

Function for passive diffusion equation from Crank (1975) used in Optimization code

```

function F = Crank(D,r)

global t

%Defined values
Co = 4148;
V = 30;
a = ((V*3)/(4*pi))^(1/3);
D0 = 4E-4;

F = ((1/2).*(Co).*(erf((a-
r)./(2.*(sqrt(D.*t))))+(erf((a+r)./(2.*(sqrt(D.*t))))))-
((Co./r).*(sqrt((D.*t)./pi)).*((exp((-((a-r).^2))./(4.*D.*t)))-
(exp((-((a+r).^2))./(4.*D.*t)))));

```